Development of a 3D radial MR Imaging sequence to be used for (self) navigation during the scanning of the fetal brain in utero

by

Leah Morgan

Thesis presented for the degree of
Master of Science
June 2016

Department of Human Biology

University of Cape Town

Research Supervisors:

Professor Ernesta Meintjes

University of Cape Town, ernesta.meintjes@uct.ac.za

Professor Andre Van der Kouwe

A.A. Martinos Center for Biomedical Imaging, andre@nmr.mgh.harvard.edu

University of Cape Town
Department of Human Biology

Plagiarism Declaration

1. I know that plagiarism is wrong. Plagiarism is to use another's work and pretend that it is one's own.
2. I have used the IEEE convention for citation and referencing. Each significant contribution to, and quotation in, this project from the work(s) of other people has been attributed, and has been cited and referenced.
3. This project is my own work.
4. I have not allowed, and will not allow anyone to copy my work with the intention of passing it off as his or her own work.

Signed: Signed by candidate

Date: 15/06/2016

Abstract

Imaging the fetal brain *in utero* is challenging due to the unpredictable motion of the fetus. Although ultra-fast MRI sequences are able to image a 2D slice in under a second, thus limiting the time in which fetal motion can corrupt images, Cartesian sampling makes these sequences sensitive to signal misregistration and motion-corruption. Corruption of a single 2D slice renders it impossible to reconstruct 3D volumes from these slices without complex slice-to-volume registration. There is a need for motion-robust sequences that can produce high-resolution 3D volumes of the fetal brain.

The Siemens Cardiovascular sequence was edited to produce a new radial readout that sampled a 3D spherical volume of k-space with successive diametric spokes. The diameter end points map a spiral trajectory on the surface of a sphere. The trajectory was modified so that multiple sub-volumes of data are sampled during a single acquisition where *M* is the number of sub-spirals and *N* is the number of diametric spokes per sub-spiral. This allows reconstruction of individual sub-volumes of data to produce a series of low-resolution navigator images that can be co-registered to provide information on motion during the acquisition. In this way, a segmented sequence suited to self-navigation was developed.

Imaging parameters for the 3D radial sequence were optimised based on theoretical calculations and scans performed in adult brains and abdomens. Optimum values for *M* and *N* needed to be determined. Increasing *M* for a constant total number of projections improves the temporal accuracy of motion tracking at the expense of decreased signal to noise ratio in the navigator images. The effects of breathing and rigid body motion on image quality were also compared between 3D radial and equivalent 3D Cartesian acquisitions.

Custom reconstruction code was written to separate the incoming scan data according to the sub-spiral trajectories described within the sequence such that individual navigator images could be reconstructed. Successive sub-spiral images were co-registered to the first navigator image to quantify motion during the acquisition. The resulting transformation matrices were then applied to each sub-spiral image after reconstruction and co-registered sub-spiral images combined in image space to generate the final 3D volume. To improve the quality of navigator images, a method is presented to perform navigator image reconstruction at a lower base resolution, thus reducing streaking artifacts and improving the accuracy of image co-registrations.

Finally, the methods developed were applied to two fetal scans.

The radial sequence was shown to be more motion-robust than an equivalent Cartesian sequence. The minimum number of diametric spokes that provided navigator images that could be accurately co-registered when scanning an adult brain was *N=256*, which could be acquired in 1.25 s. For abdominal scans, the minimum number of spokes was *N=1024*, which could be acquired in about 6 s when water excitation is applied. However, the latter could potentially be reduced by reconstructing navigator images at a lower base resolution. Although fetal scans demonstrated poor image contrast, navigator images were able to track motion during the acquisition demonstrating the potential use of this method for self-navigation. In conclusion, a motion-robust radial sequence is presented with potential applications for prospective navigation during fetal MRI.

Acknowledgements

Prof. Ernesta Meintjes from the University of Cape Town and Dr. Andre J.W. van der Kouwe from the Athinoula A. Martinos Center for Biomedical Imaging (Boston, USA) supervised this work. They provided the necessary context, advice, support and expertise required for the implementation of this work.

Additional acknowledgement must be given to Dr. van der Kouwe, for providing the resources and support required for sequence development and image reconstruction. Dr. Himanshu Bhat generously provided the source code for the Siemens Cardiovascular sequence used for editing in this work. In addition, Dr. Bhat provided expert advice and numerous resources from his own research for editing the sequence with a new trajectory. Patrick McDaniel assisted with the registration section of this work and provided useful resources for extracting information from the registration of navigator images.

The following organisations have provided the resources required for this work: The University of Cape Town, Cape Universities Body Imaging Centre, the Groote Schuur Hospital (GSH, Cape Town, South Africa), the Athinoula A. Martinos Center for Biomedical Imaging (Boston, USA), Massachusetts General Hospital (MGH, Boston, USA) and the Boston Children's Hospital (BCH, Boston, USA).

Acquiring fetal scans would not have been possible without the support of Prof P. Ellen Grant from the Fetal-Neonatal Neuroimaging & Developmental Science Center at BCH and Dr. Sally Candy from the Groote Schuur Hospital. Scans for the results presented in this work were supervised by Borjan Gagoski (MR Physicist at BCH) and radiologists Ingrid Op't Hof and Petronella Samuels from GSH. We would like to express our thanks to all the subjects and pregnant mothers who volunteered to be scanned.

Research funding was provided by the South African Research Chairs Initiative, the National Research Foundation of South Africa, the University of Cape Town and NIH grants R21AA017410 and R01HD071664. Research scans were supported by the Fetal BRP grant for the Fetal-Neonatal Neuroimaging & Developmental Science Center, Boston Children's Hospital (NIH- 1R01EB017337-01).

Table of Contents

List of Figures

List of Tables

1. Introduction

Since Magnetic Resonance Imaging (MRI) provides excellent soft tissue contrast, MRI of the fetus *in utero* has the potential to provide unprecedented insight into fetal development throughout gestation. In particular, it enables observation of neurodevelopment as well as the mechanisms and consequences of abnormal development. Since MRI is a non-invasive imaging modality and does not contain any ionizing radiation, it is considered safe for fetal imaging after the first trimester of pregnancy [1], [2], [3].

In contrast to ultrasound, MRI is not limited by the position of the fetus or maternal obesity and the fetal anatomy can be imaged with clearer diagnostic accuracy [4]. This enables better management of high-risk pregnancies. Therefore, although MRI is currently only used as an adjunct to ultrasound when clinically indicated, it is arguably a more effective technique for monitoring fetal development and should be pursued as a primary imaging method.

However, fetal MR imaging is uniquely challenged by the continuous and unpredictable motion of the fetus. Motion during MRI signal acquisition results in incorrectly registered data and disruptive image artifacts [5]. Although methods are continuously being developed to reduce the effects of motion, very few of these are applicable to fetal imaging. This is because fetal motion is often non-rigid and can occur in multiple planes simultaneously, making it difficult to simulate or predict. When imaging a small field of view to acquire only the fetal brain, it is sometimes the case that by the time the acquisition is complete the fetal head will have shifted out of the image field of view entirely.

The sequences currently used for fetal MRI are fundamentally limited in their ability to address the challenges of fetal motion due to the Cartesian sampling techniques that they implement. Typically the sequences sample consecutive two-dimensional (2D) slices of data and use a Cartesian sampling technique to fill each slice in k-space line-by-line [6]. This strategy makes the sequences vulnerable to the effects of fetal motion in two ways. Firstly, the fetus can move during the acquisition of k-space lines within a slice, resulting in incorrectly registered data particularly in the phase-encode direction and ghosting artifacts that degrade the image quality [7]. These sequences are also affected by inter-slice motion that occurs in the time between acquisitions of 2D slices and disrupts the positions of corresponding voxels between slices [6]. This complicates the process of slice-to-volume registration, required to reconstruct 3D volumes from successive 2D acquisitions [8].

To address these issues, “ultrafast” sequences that implement single-shot techniques for rapid data acquisition have been developed. These increase the speed of slice acquisition to less than 1 second which reduces, but does not eliminate, the risk of motion within a slice [6], [9]. If motion does occur during slice sampling, image artifacts are inevitable due to the inherent motion-sensitivity of the Cartesian sampling technique. Additionally, images will be severely affected if motion occurs particularly during the acquisition of the central few lines of k-space, since these are the only lines that contain low spatial frequency information, which provides image contrast. Therefore, in a clinical setting and for practical reasons, if the fetus moves it is more likely that the data will be discarded and the acquisition repeated, resulting in long scan times for the mother.

To prevent redundant scanning in other applications of MRI where motion frequently occurs, navigation techniques are implemented to track a region of interest as it moves and update sequence parameters in real-time, thereby correcting for motion during an acquisition. Recently, a navigator for tracking the diaphragm was implemented during a fetal scan with promising results [10]. However,

the acquisition time increased from the usual sub-30 seconds to 7 minutes with severe fetal motion, and the navigator was not always successful in continuously tracking fetal motion. Therefore to date, no practical methods are available for navigation during fetal scans and motion in fetal MRI remains an unresolved issue. Scans are conducted "blindly", subjecting radiographers to a trial-and-error approach where acquisitions are repeated in an attempt to gather useful images for diagnosis.

There is a need to develop a sequence capable of producing high-resolution 3D volumes of the fetal brain. To do this, an alternative sampling technique must be employed that is motion-robust compared to Cartesian sampling. Additionally to avoid redundant scanning, the sequence should ideally be capable of self-navigation, which means that when motion does occur the sequence should detect this and allow affected data to be co-registered so that it can still be used in the generation of the final image. Radial sampling trajectories have been shown to be inherently motion-insensitive due to the fact that each spoke contains a balanced sampling of both high and low spatial frequencies. Radial sampling effectively causes the effects of motion to be distributed in all directions [11]. Further, the fact that every diametric spoke passes through the centre of k-space means that the central region of k-space is significantly over-sampled. This makes radial sequences particularly suited to navigation applications as very few spokes can provide sufficient signal to generate a useful navigator image [12].

This project aimed to reduce the effects of fetal motion in fetal MRI by addressing two major limitations of the sequences currently used. These limitations are the motion-sensitive Cartesian sampling techniques that are implemented and the absence of techniques to track fetal motion during an acquisition. Therefore, the first aim was to develop a 3D radial sequence capable of performing rapid MRI scans of the fetal brain. Secondly, the sequence needed to be suited to self-navigation by producing consecutive low resolution images at regular intervals that could be used to track the position of the fetal brain throughout an acquisition.

Outline

In chapter 2, the physical principles behind MRI are described with particular emphasis on techniques for spatial encoding, leading into a discussion on the mechanisms of how motion, particularly fetal motion, induces image artifacts. The various sequences that are currently used in fetal MRI are critically evaluated to reveal fundamental issues with the Cartesian sampling technique. Other considerations when imaging the fetus are then discussed, such as the unique anatomical environment of the uterus as well as ethical and safety concerns related to fetal MRI. Some techniques for motion compensation are then presented such as post-processing and prospective navigation. An example of a recent attempt to apply a navigation technique to fetal MRI is briefly assessed. The Siemens reconstruction algorithm for radially sampled data is then described to provide an understanding of the reconstruction code which was modified in this project.

The following three chapters each comprise five sections – sequence development, protocol optimization, a comparison of Cartesian and radial sequences, image reconstruction, and *in vivo* fetal scans. Chapter 3 outlines the methods used for each aspect of the development. The mechanism of radial spatial encoding is explained before looking at the particular sampling trajectory developed in this work. A segmented scan using multiple sub-volumes of data is presented as a method for a self-navigating sequence. An optimized protocol is then developed for scanning the adult brain and abdomen. The minimum number of diameter readouts required to reconstruct a navigator image is determined for each type of scan. The 3D radial sequence developed here is then compared to an equivalent 3D Cartesian sequence to evaluate the effects of breathing motion and rigid body motion between the two. The method of designing custom reconstruction code is described for suitable

reconstruction of navigator images produced by this sequence. A novel method is presented for improving the quality of navigator images produced from radially sampled data. Navigator images are co-registered to demonstrate applications for self-navigation with the radial sequence developed here. Finally, *in vivo* fetal scans are performed where the developed protocol is implemented and evaluated.

In chapter 4, the results from each of the five sections are presented. In chapter 5, the results are critically evaluated and discussed with particular reference to applications in fetal MRI where relevant. Finally, in chapter 6, conclusions are drawn from the preceding results and recommendations are made for future work.

2. Background and Literature Review

2.1. The Basics of Magnetic Resonance Imaging

Nuclei that have an imbalance between the number of neutrons and protons have a net angular momentum and can be imaged using MRI. The hydrogen (^{1}H) nucleus, consisting of a single positively charged proton, is abundant in tissues throughout the human body and is therefore very frequently imaged in MR. A hydrogen nucleus, which is positively charged, spinning about its own axis produces a net magnetic field resembling that of a tiny bar magnet, called a magnetic dipole moment (μ). When the body is subjected to an externally applied magnetic field (B_0, measured in Tesla) every dipole moment experiences a torque that causes it to precess around the direction of the net magnetic field at a characteristic frequency, called the Larmor frequency, that is proportional to the magnetic field strength and is given by

$$\omega_L = \gamma B_0, \tag{2.1}$$

where γ is the gyromagnetic ratio of the proton being imaged. For hydrogen, $\gamma = 42.6$ MHz/Tesla. Therefore at 3 Tesla, which is the magnetic field strength of the scanners used in this project, the precessional frequency of hydrogen is

$$\omega_L = (42.6)(3) = 127.8\ MHz.$$

Since the transverse components of the dipole moments cancel and more protons align parallel to the direction of B_0 than anti-parallel, to attain a lower energy state, a net longitudinal magnetization (M_0) is produced parallel to B_0.

Another important component of MRI is the radio frequency (RF) pulse, an electromagnetic wave transmitted at the Larmor frequency (ω_L) such that it will alter the precession of the hydrogen protons about B_0. During MR imaging, the person or object to be scanned, is placed on a retractable table that moves into the scanner bore. An RF coil is placed around the body part to be imaged and can resemble either a helmet-like device (for head imaging) or a padded blanket (for abdominal imaging). These coils are typically transmit and/or receive coils meaning they can transmit a radio frequency pulse and/or receive the MR signal produced.

To generate the MR signal, an RF pulse is applied such that it produces a tiny alternating magnetic field, B_1, perpendicular to the main magnetic field. If the RF pulse is applied at the Larmor frequency, resonance occurs and the net magnetization will begin to precess around B_1. This causes the magnetization vector to spiral towards the transverse plane perpendicular to B_0. Typically, the direction of the main external magnetic field is denoted the z-direction and is called the longitudinal direction, while the plane perpendicular to that, i.e. the x-y plane, is called the transverse plane. The duration of the RF pulse determines the flip angle (α). For a 90 degree flip angle the magnetization is flipped entirely to the transverse plane ($M_{xy} = M_0$) and there is no remaining longitudinal

magnetization (M_z = 0). For smaller flip angles, the magnetization will have both transverse and longitudinal components.

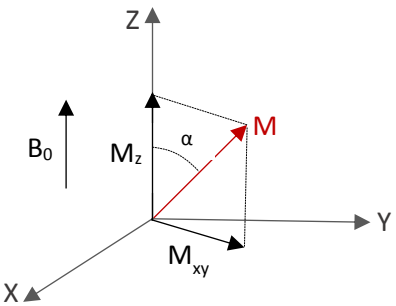

Figure 2.1. Transverse (Mxy) and longitudinal (Mz) magnetization vectors generated by a partial flip angle.

As soon as the RF pulse terminates, the magnetization vector starts precessing around B_0 only again and returns via a spiraling motion back to its original alignment and lowest energy state parallel to B_0. The energy that was transmitted to the spins during excitation is given back to the lattice in a process known as spin-lattice relaxation. The rate at which the energy is returned to the lattice determines the spin-lattice relaxation rate, T1, which is defined as the time it takes the z-component of the magnetization (M_z) to regrow to 63% of its maximum value (M_0) according to equation 2.2:

$$M_z(t) = M_0\left(1 - e^{-\frac{t}{T1}}\right). \quad (2.2)$$

Independently, the transverse component M_{xy} decays once the RF pulse is switched off due to the fact that the local chemical environment around individual spins differ causing each spin to precess at a slightly different frequency. This rate of decay, characterized by the time constant T2, is known as spin-spin relaxation. T2 decay is 5 to 10 times more rapid than the T1 relaxation and is given by

$$M_{xy}(t) = M_0\left(e^{-\frac{t}{T2}}\right). \quad (2.3)$$

In reality, other sources of inhomogeneity contribute to the decay of the transverse magnetization, so that it occurs faster than it would otherwise. The time constant T2* defines the rate of decay of the transverse magnetization due to spin-spin interactions as well as other external inhomogeneities. The oscillating transverse magnetization vector induces a current in a receiver coil according to Faraday's law. This induced signal constitutes the MR signal.

Factors Affecting Image Contrast

Image contrast is affected by a great number of factors. The parameters described below are not an exhaustive list of all factors that can affect the image contrast, but only those most relevant to this project.

RF pulse timing (TR, TE) to control T1 and T2 weighting

T1 and T2 are inherent properties of the tissues being imaged and cannot be manipulated. However, specific sequence parameters can be manipulated to alter the source of the contrast in the image.

Two such parameters are the time between successive RF pulses, known as the repetition time, TR, and the time between the RF pulse and signal readout, known as the echo time, TE. TR and TE can be manipulated to acquire specific image contrasts.

- A T1-weighted contrast is achieved with a short TR and short TE. When TR is short (i.e. of the order of the T1 of the tissues relaxing fastest), the T1 recovery of the tissues relaxing slowly will have only just begun and therefore the difference in M_z values between fast and slowly relaxing tissues will be maximal, increasing the contrast in the image. Since TE is short, effects from differences in rates of transverse decay will be negligible.
- A T2 weighted contrast is achieved with a long TR and long TE. When TR is long enough, the longitudinal magnetization will have recovered almost fully for all tissue types, so that no contrast arises from differences in T1. For a longer TE, signal from tissues decaying faster will be minimal compared to tissues decaying more slowly, thus increasing the contrast due to differences in T2.
- A proton-density weighted contrast is achieved with a long TR and very short TE. This is because contrast due to differences in T1 and T2 have both been minimized. This can be explained by observing the signal equation for a spoiled gradient echo (GRE) sequence (as used in this project):

$$S = \frac{\rho\left(\sin\alpha\left(1-e^{-\frac{TR}{T_1}}\right)e^{-\frac{TE}{T_2^*}}\right)}{1-\cos\alpha.e^{-\frac{TR}{T_1}}}. \qquad (2.4)$$

For a small TE, the T2* term approaches unity and for a long TR, the T1 term is minimized. By minimising the T1 and T2 factors, the signal contrast is largely due to differences in proton-density, ρ, between different tissue types.

RF Pulse Amplitude (Flip Angle)

The flip angle is another parameter that can be manipulated to alter the image contrast. Since RF energy deposition is proportional to the square of the flip angle (α^2), it is important to understand the effect that lowering the flip angle will have on the achieved image contrast since, for fetal imaging, it is desirable to minimize the RF energy deposited during the scan and it may be required to do this by reducing the scanning flip angle.

For typical GRE FLASH (Fast Low Angle Shot) sequences, such as the one that was used as the base sequence for further development in this work, scanning with a higher flip angle ($45^0 < \alpha < 90^0$) typically increases the contrast due to differences in T1 between tissues. A larger flip angle ensures that the remaining M_z component after the RF pulse, is small so that its value before the next RF pulse is impacted significantly by longitudinal relaxation. As a result, for a short TR, the M_z component prior to the next RF pulse will differ significantly between tissues with short and long T1's, increasing the T1-weighting in the image [13].

In contrast, smaller flip angles ($\alpha < 20^0$) reduce the T1 weighting in the image as significant M_z remains after the RF pulse and differences in longitudinal recovery rates of different tissues do not alter this

residual M_z significantly. For very short TR and TE times (< 10 ms) the proton-density weighting is maximized [13].

For extremely short repetition times (TR < 5ms, TR << T1) and very low flip angles such as those implemented in ultrafast imaging, the longitudinal magnetization M_z cannot fully recover in the time before the next RF pulse excitation and therefore a lower steady-state signal (M_{ss}, $M_{ss} < M_0$) is achieved after the first few pulses. For ultrafast spoiled GRE sequences, this means that images contain proton-density weighted contrast instead of T1 contrast and notoriously low signal [14]. Therefore, when acquisition speed is paramount, the desired image contrast is not always achievable.

Spatial Encoding of k-Space

The signal received by the receiver coil contains no spatial information. Magnetic field gradients are introduced to spatially encode the signal. Altering the strength of the magnetic field across the scanner bore in the X, Y and Z directions causes the precessional frequency, and as a result the frequency of the MR signal, to vary with position.

In conventional two-dimensional (2D) MR sequences, the Gz gradient is applied at the same time as the RF pulse. Only spins in a narrow slice will meet the resonance condition and only these spins will be excited, thus achieving slice selection. Successive slices are selected by applying subsequent RF pulses at the appropriate frequencies to select adjacent slices.

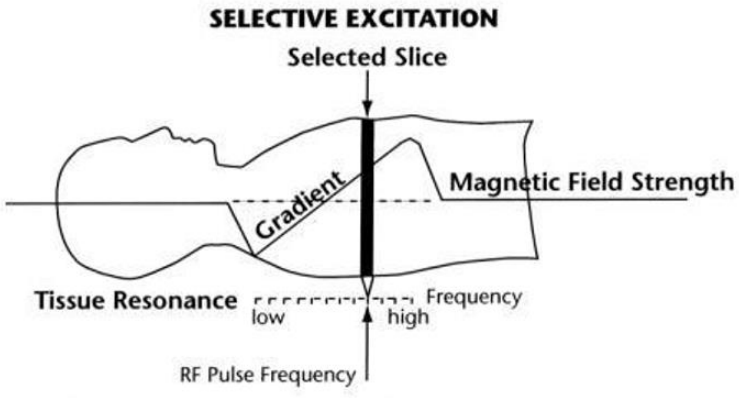

Figure 2.2. A single imaging slice is selected by applying an RF pulse at the resonant frequency for the protons contained in that slice. Adapted from [15].

After the RF pulse and Gz have been switched off, there is a delay (TE) before the signal echo can be measured. The echo contains signal from the entire slice. To create an image of a slice, it is necessary to know how much signal is coming from each pixel. To determine this, two orthogonal gradients are applied in the Gy and Gx directions before and during signal readout, respectively, to encode each row of pixels with a unique phase (Gy) and each column of pixels with a unique frequency (Gx). The combined effect is that each pixel has its own corresponding phase shift and frequency and therefore the echo signal now contains information on the original location of each signal component. To obtain enough information to reconstruct the image of a slice, signal readout is repeated for different phase encoding gradients. The matrix size of the final image determines the number of phase encoding steps required.

Figure 2.3 is a very simple pulse sequence diagram to illustrate the various gradient parameters and timings present in a typical MRI sequence.

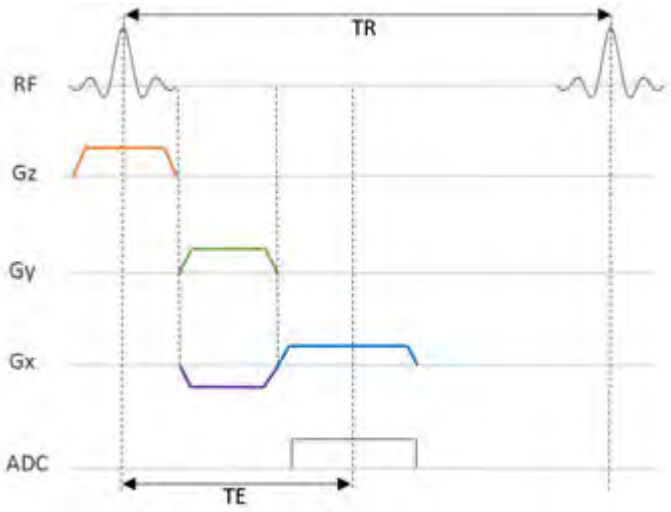

Figure 2.3. Example of a basic Pulse Sequence Diagram for a standard Cartesian encoding scheme. Note the gradient timings for the slice-select gradient (Gz), the phase encode gradient (Gy) and the frequency encode gradient (Gx).

The analog signal received after each excitation is digitized during readout. These data points fill a single line in a matrix of digitized data space, called k-space. The axes of k-space, Kx and Ky, correspond to the frequency and phase encoding directions respectively.

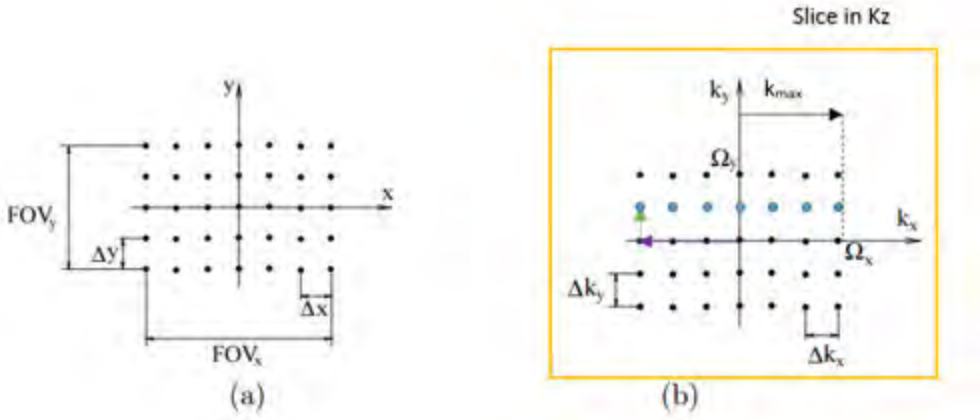

Figure 2.4. To illustrate the relevant dimensions for spatial encoding in image space (a) and k-space (b). Adapted from [16]

Different rows in k-space are filled by varying the phase encode (Gy) gradient strength. By selecting the field of view (FOV) and matrix size, the user can control the dimensions of k-space to be filled. A typical matrix size is 256 x 256 pixels. An important property of k-space is the spatial frequency distribution. The central region of k-space contains high amplitude signals with low spatial frequencies and provides all the tissue contrast information for the final image [13]. The periphery, i.e. high spatial

frequencies, contains low amplitude signals and provides the fine detail information [13]. Two conclusions are worth noting here. Firstly, the peripheral regions are important to include in image reconstruction to prevent blurry output images [11]. Secondly, when k-space is filled line-by-line, it is crucial that no motion occurs during acquisition of the central rows since these contribute to almost all of the contrast signal in the final image [11]. The line-by-line manner described here is a Cartesian sampling scheme and is one of the most common sampling strategies used.

2.2. Evaluating the Current Methods for Fetal MRI

The steady development of MRI hardware and software has recently enabled successful MR imaging of the fetus *in utero*, 30 years after it was first proposed [6]. Many years of development were required to establish scanning methods that are capable of addressing the technical challenges associated with fetal MRI. The principal challenge is fetal motion [7], which remains the driving force behind the continuous development of fetal scanning techniques. Since the risk associated with using sedentary drugs is no longer acceptable [17], fetal scanning always runs the risk of being corrupted by motion artifacts as a result of the regular and unpredictable motion of the fetus during the scan [7].

How Fetal Motion Affects MR Images

The shifting of the fetus during an MRI scan causes signal interruptions and data errors, resulting in motion artifacts that corrupt the final image [7]. This is because the process of converting k-space voxels to image pixels assumes correctly registered phase and frequency information [5]. The irregular motion of the fetus prohibits lengthy k-space acquisitions such as those required for 3D sequences and so typically, Cartesian scanning techniques are used which sample 2D slices in a line-by-line manner [6]. This technique is illustrated in Figure 2.5.

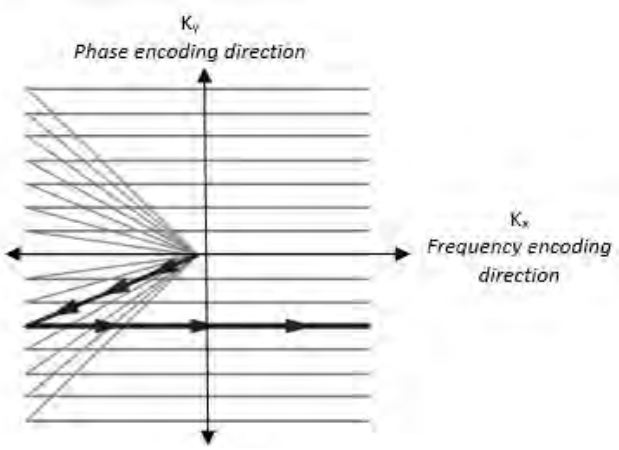

Figure 2.5. A single line in k-space filled using a Cartesian sampling scheme. Adapted from [11].

Shifting-motion artifacts often appear as ghosting artifacts in the phase encoding (Ky) direction [5], which is the repetition of the object image that often overlaps the object itself. This artifact appears in the phase encode direction specifically because a much larger time gap exists between the acquisitions of adjacent lines in k-space than adjacent frequency encoded points and so there is more risk for motion to occur between the acquisitions of k-space lines, resulting in signal variations between these lines [11]. Severe ghosting can also appear as vertically-oriented diffuse image noise or blurring in the final image [18], [5].

Along with the shifting motion of the fetus, other motion-induced effects must also be considered. In particular, maternal breathing also causes blurring and ghosting artifacts [5], and motion of the amniotic fluid as a result of the fetus shifting, leads to signal intensity artifacts [6].

Ultrafast Sequences

Today, the most commonly used techniques for fetal imaging are Single-Shot T2-Weighted (SST2W) sequences [6]. Although the fundamental technique is the same, these sequences go by different developer names e.g.: HAlf-fourier Single-shot Turbo spin Echo (HASTE – Siemens), Single-Shot Fast Spin Echo (SSFSE – General Electric Medical systems) and Single-Shot half-Fourier Turbo Spin Echo (SShTSE – Philips) [6]. The Single-Shot feature common to all these sequences minimizes fetal motion artifacts. First, a single slice-selective RF pulse is applied, followed by multiple refocusing pulses that create a series of spin echoes (Fig. 2.6, [19]). During each echo, lasting approximately 2-3 ms [6], frequency encode gradients are applied to sample a horizontal line in k-space. On either side of each readout, opposite phase encode gradients are applied with the strength varying between successive pairs so that the 2D slice in k-space is filled line-by-line in the typical Cartesian manner [19].

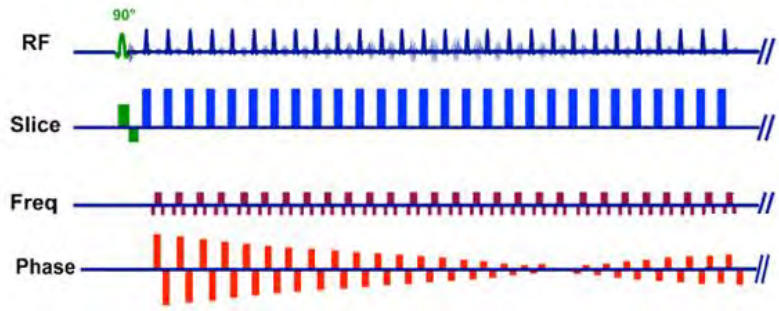

Figure 2.6. Pulse sequence diagram for a typical single-shot turbo spin echo sequence used for rapid T2-weighted 2D slice imaging [19].

What sets these sequences apart is that an entire k-space slice is sampled following a single RF pulse [20]. In sequences that implement the half-Fourier technique, just more than half of the total k-space lines are actually sampled while the rest are generated using the mirroring properties of k-space i.e. conjugate symmetry [6]. In this way an entire 2D slice can be acquired in less than a second. These sequences have therefore appropriately been named “ultrafast” sequences [9], [21].

To generate a 3D volume of data, a series of 2D slices are acquired to form a “stack”. Multiple slices need to be sampled in the shortest time possible since there is always the risk that the fetus may shift between slice acquisitions [6]. With these types of sequences, slice “cramming” is necessary to be able to cover the largest volume possible in less than 20-30 seconds, since longer scans are likely to be corrupted by fetal motion [6]. In fact, it is generally expected that scans longer than 25 s will be degraded by fetal motion artifacts. However, the delay between slices cannot be too short otherwise the remaining T1 signal from amniotic fluid will interfere with the signal in the next slice [6].

Therefore, although these sequences are generally presumed fast enough to be exempt from intra-slice fetal motion [22], they are still vulnerable to inter-slice motion [6]. Should motion occur between the acquisitions of slices, the scan is reduced to a series of isolated 2D snapshot images unless computationally expensive slice-to-volume registration methods are implemented post scan [8], [11]. Another disadvantage of SST2W sequences is that even at 1.5T, they generate high values for energy

absorption compared to other types of sequences [23] [24], which imposes a risk to both the mother and the fetus [25]. Today, fetal MRI is frequently conducted at 3T and so the specific absorption rate (SAR) values for these sequences will be even higher. Since SAR limitations will also limit the minimum allowable TR time [26], these sequences often cannot perform at their optimal speeds anyway making them susceptible to fetal motion artifacts.

Single-shot sequences require very long echo times and so they are predominantly T2 weighted [6], which is generally preferred by clinicians for diagnosing the health of amniotic-fluid-filled air passages [27] but cannot provide information, for example, on the health status of the thyroid, pituitary gland, liver and adipose content in the way that T1-weighted sequences can [28], [29], [30].

Another sequence that has been successfully employed in fetal MRI is the spoiled gradient echo (SPGR) [6]. In these sequences, an RF pulse is applied along with a slice-select gradient, followed by a gradient echo readout [13]. These sequences then apply "spoiler" gradients after readout to eliminate any remaining transverse magnetization component before the application of the next RF excitation pulse [31]. This type of sequence is more versatile in terms of achievable contrast than the SST2W sequences. They can be appropriated for detecting damage caused by hemorrhages in the fetal brain by setting longer TE times to achieve the necessary T2* weighting [6]. However, as a result of longer TE times, the number of slices that can be acquired within the generally appointed time limit of 25 s is limited to only about 4 [6]. SPGR sequence parameters can also be adjusted to acquire T1-weighted images by increasing the flip angle and reducing the TE time to a minimum which has unique diagnostic applications as mentioned earlier.

Some more recent developments in fast 3D SPGR sequences implement techniques such as asymmetric partial k-space sampling as well as very short TR/TE times to achieve T1-weighted images in under 30 seconds [6]. Examples of these include VIBE (volumetric interpolated breath hold - Siemens) and LAVA (liver acquisition with volume acquisition – GE). However, since these sequences sample the entire 3D volume over the duration of the scan, even with reduced scan times, they are still more sensitive to motion than the slice-by-slice methods discussed earlier. This method is preferably used with maternal breath-hold and when the fetus is assumed to be still [6].

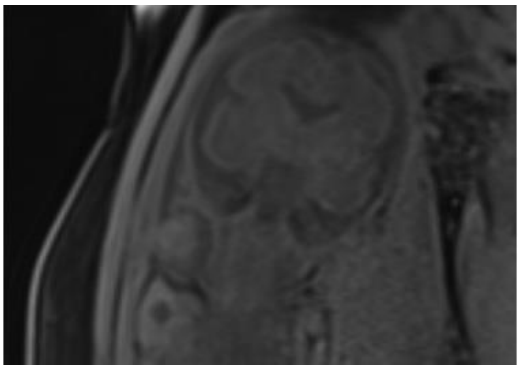

Figure 2.7. Image of the fetal brain using a T1-weighted, 3D spoiled gradient echo sequence (Siemens VIBE) at 3T [6].

Unspoiled gradient echo sequences have also been successfully implemented in fetal imaging in the instances of FIESTA (fast imaging employing steady-state acquisition) and b-SSFP (balanced Steady State Free Precession) [6]. In these instances, instead of applying a "spoiler" gradient to eliminate

transverse magnetization, the free induction decay signals between successive RF pulses are allowed to accumulate and refocus such that a constant signal of varying amplitude is present throughout the acquisition [6]. Major advantages of these sequences is the increase in overall signal-to-noise (SNR) ratio in the acquired images and the capacity for rapid imaging of the fetus since RF pulses can be applied in quick succession [32]. However, the type of tissue contrast is limited to T2/T1, which limits applications in the context of monitoring fetal anatomy [6].

In summary, fetal MRI has been conducted successfully with various Cartesian sequences, including SST2W, b-SSFP and 3D SPGR methods [6], despite the challenges presented by fetal motion, particularly in early stages of gestation [33], [34]. None of these sequences are, however, exempt from fetal motion effects since all of them implement a Cartesian spatial encoding technique that is inherently vulnerable to motion. Any motion that does occur will result in a signal modulation in k-space which translates directly into motion artifact in image space once a Fourier transform is applied [11], [35]. The ghosting artifacts produced often overlap the imaged object and may interfere with diagnosis. This is a generally recognised problem amongst clinicians regarding Cartesian sequences [18].

Other Considerations for Fetal MRI

Anatomy

The anatomical development of the fetal brain also presents some of its own challenges in MRI. The immature fetal brain contains a high percentage of water and is mostly unmyelinated, meaning that little fatty tissue exists at this stage of development [7]. This results in poor tissue contrast and subsequently low-quality images. Challenges associated with poor tissue contrast must be overcome in order to prevent inaccurate diagnoses of fetal brain abnormalities. The fetal brain also represents a small region of interest in comparison to the rest of the maternal abdomen. Typically a large FOV (> 30 cm) is specified for imaging a pregnant woman even though the fetal brain would occupy only a small area within the FOV. Alternatively, when specifying a small FOV to include only the fetal brain, it is difficult to prevent wrap-around artifacts in the phase encode direction [6]. There is also a large distance between the fetal brain and the receiver coils which lie on the mothers' abdomen, resulting in inefficient sampling of the signal coming from the fetal brain.

Safety Concerns

The ethics surrounding fetal MR imaging remain a concern and contribute towards the assumption that fetal MRI is an unsafe practice. This assumption exists predominantly in countries where fetal MRI is still a very new concept. Today, opinions are evolving since it is more commonly recognized that MRI contains no ionizing radiation and does not threaten to interfere with the development of the fetus [3]. MRI is often negatively associated with other imaging modalities such as X-ray and Computer Aided Tomography scans [36], which do make use of ionizing radiation and are known to impose a risk of cancerous cell development [37].

The more recent evolution of most MRI procedures from 1.5T to 3T due to the achievable improvements in image quality [38], has encouraged the upgrade of fetal MRI to 3T [2]. As a result, original concerns surrounding safety have re-surfaced in the context of 3T and so it is important to address these concerns since this is ultimately the end-goal of the research conducted in this project.

It is important firstly to note that subjecting the fetus to the stronger static magnetic field of 3 Tesla has not been shown to cause any long-term or short-term negative effects [39], [40]. The most recent USA FDA guideline for fetal MRI now reads "At this stage, the predominance of research studies have failed to discover any reproducible harmful effects of exposure of the mother or developing fetus to

the 3T or weaker magnetic fields used in the clinical MR imaging process." [1]. It is therefore a commonly held belief amongst researchers familiar with fetal MRI that there is no increase in risk to the pregnant mother or fetus when by exposing the fetus to static magnetic field strengths of 3T as opposed to 1.5T [2].

However, another valid concern surrounding fetal MRI at 3T is the increase in RF frequencies which corresponds to higher power in the RF pulses and the potential effects of this are declared less certain by the FDA [1]. They advise that a "thorough and thoughtful evaluation of the potential and at times unknown risks of the MR examination versus the potential benefits to the patient" must be considered before proceeding with the examination at 3T [1]. The reason for concern is that alternating magnetic gradients during a particular volume excitation, give rise to electric fields which generate ionic currents with the ions from salt within the body [2]. Electrical conduction within body tissues in turn generates heat. To prevent the uncontrolled dissipation of heat throughout the body, MRI scanners implement strict RF energy limits. These limits are a ratio of the RF power in Watts (W) deposited per kilogram (Kg) of tissue, known as the specific absorption rate (SAR) [41]. Studies have found that the safety of the fetus is preserved at 3T as long as SAR limits are adhered to and many studies have been conducted to ensure that the unique anatomical environment of the pregnant abdomen does not alter heat dissipation mechanisms such that local SAR values unexpectedly rise above the safety limits [42], [43], [44], [45]. The sequence developed in this work is to be run on a Siemens scanner and so the SAR limit of 2 W/kg will apply as determined by the International Electrotechnical Commission (IEC) [46]. In practice, if the MRI system anticipates that SAR limits will be exceeded during an acquisition, the exam will be automatically stopped before the sequence is run and the user will be notified which scan parameters must be adjusted in order to reduce the SAR value [2]. Therefore, we feel confident that the research conducted in this project will obey all SAR limits and pose no greater risk than other routinely implemented fetal MRI scans.

There is also a concern that imaging at 3T poses an increased risk of peripheral nerve stimulation (PNS). However, PNS is not linked to the static magnetic field and so the risk is equal to imaging at 1.5T on Siemens scanners since the gradient designs are equivalent [47]. A high rate-of-change of readout gradients is what actually results in PNS [2]. However, this does not need to be a concern as in practice the scanner will assess the gradient rate-of-change in advance and warn the radiographer if any stimulation will be experienced by the patient, who can then decide to increase the TR time and thereby reduce the risk [2]. Additionally, the fetus is often positioned at the isocenter where gradient field variation is at a minimum and so the concern for PNS is further reduced [2].

Finally, the acoustic noise generated by the rapidly alternating electromagnetic currents as readout gradients are generated, is thought to pose a risk to the fetus' hearing. During a typical MRI scan, the patient will wear ear plugs to prevent discomfort and possible damage to hearing. Although the fetus has no option in this regard, it is believed that acoustic noise is dampened by the soft tissues and amniotic fluid surrounding the fetal head within the abdomen, as well as the fluid which fills the ear [2]. This theory is supported by the numerous follow-up studies of children who were imaged *in utero* that have reported no hearing impairment [48], [49], [50], [40], [51]. It is pertinent however to supply additional acoustic protection at both 1.5T and 3T such as the use of acoustic padding underneath the patient [2].

To further reduce potential risk to the fetus, it is an accepted practice to refrain from performing fetal MRI before 18 weeks gestation [27], [6]. This practice is supported by the fact that scans are most successful in the third trimester anyway, when fetal motion is inhibited due to restricted space in the uterus [27]. All scans conducted in this research were performed on fetuses after 30 weeks gestation.

Predominance of Ultrasound

Ultrasound (US) remains the predominant modality for monitoring fetal abnormalities during pregnancy. The expense and complexity of MRI have limited this method as an adjunct to ultrasound [6]. However, this becomes extremely useful when diagnostic questions remain even after ultrasound has been performed. MRI has many advantages over US as it is not severely limited by fetal position or maternal obesity and the anatomy of the brain can be seen even in the presence of an ossified skull towards the end of gestation [27]. Moreover, MRI provides far superior soft tissue contrast resolution to US, allowing for better distinguishability between fetal anatomical structures [4]. However, MRI is limited in its diagnostic ability during the early stages of gestation due to the smaller anatomical features of the young fetus and the exacerbated issues with motion [1], [52]. Additionally, as mentioned before, it is not ethical to perform MRI earlier than 18 weeks gestation [6], therefore ultrasound remains the only available imaging modality during the early stages of pregnancy.

2.3. Radial Sequences as an Alternative

In Cartesian sequences, orthogonal phase and frequency encode gradients are alternated to acquire k-space data in a line-by-line manner. Whereas, in radial imaging, orthogonal gradients are applied simultaneously to generate a radial spoke-by-spoke sampling pattern over a certain FOV in k-space [11]. Encoding gradients are applied such that each readout represents a diameter of a circle (2D) or a sphere (3D) in k-space. These two sampling patterns are illustrated in Figure 2.8.

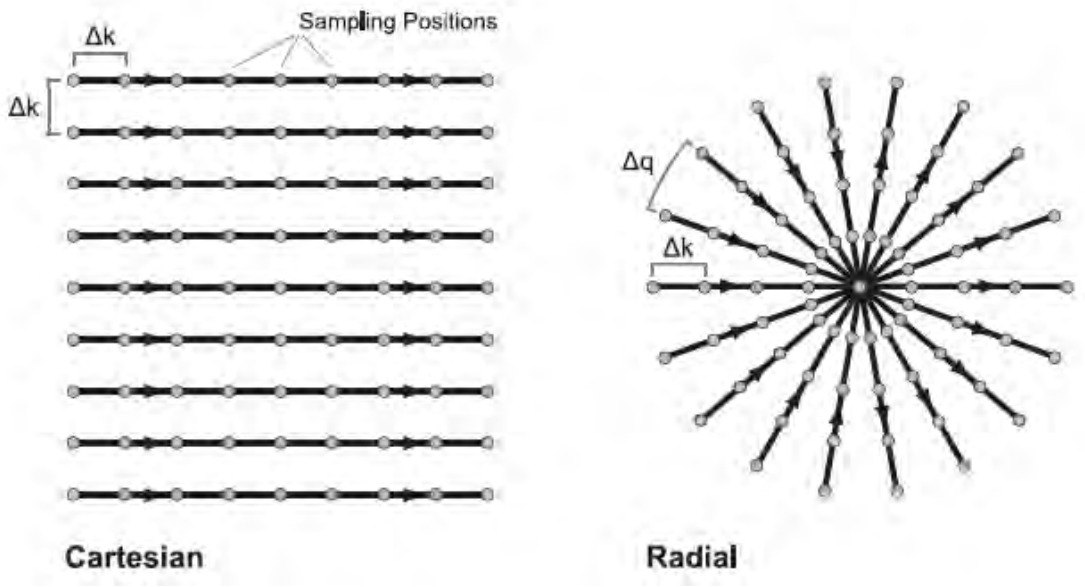

Figure 2.8. 2D k-space sampling patterns for the Cartesian and radial case [11].

In this work, 3D radial imaging is of particular interest and so many of the formulae related to radial imaging are presented for the 3D case, although 2D radial imaging is currently very popular. To achieve a 3D radial spoke at readout, the vector component gradient strengths depend on G, the overall gradient strength, and θ and $\emptyset$, the spherical coordinate angles used to describe the orientation of a vector in 3D. Therefore, the gradients at readout are represented by [53]:

$$G_x = Gsin\theta cos\emptyset, \quad G_y = Gsin\theta sin\emptyset, \text{ and } G_z = Gcos\theta. \tag{2.5}$$

The unique sampling pattern of a radial sequence has a number of benefits that may make it more suitable than traditional Cartesian sampling for fetal MRI. For example, each radial projection passes through the centre of k-space which results in a final sampling pattern where the central region of k-space is more densely sampled than the outer regions [11]. In a Cartesian sequence all spatial frequencies are equally sampled since there is a uniform distribution of encoding lines in k-space [13]. This central region represents the lower spatial frequencies for the sampled object. This may make it possible to construct low resolution images from very few radial spokes if sufficient low spatial frequency information is sampled to still produce images with enough contrast information [11]. This feature was of particular interest to this project where we wanted to explore the possibility of using radial sequences to rapidly produce low resolution navigator images for motion detection and correction throughout the scan. Another benefit of radial imaging is that a single spoke acquires a balanced sampling of both high and low spatial frequencies, which ensures that navigator images contain uniformly updated image information [12].

In contrast, Cartesian sequences have all their low spatial frequency information contained within the central few rows of k-space which makes these lines particularly important to sample accurately [11]. Should motion occur while these lines are sampled, the final image will suffer more severe artifacts than if the motion occurred, for example, when sampling the very top rows of k-space [11]. This suggests that radial sampling is more robust that Cartesian sampling in terms of when motion occurs during the sequence, since a balanced sampling with each radial spoke ensures that motion will have the same effect, no matter when it occurs during the scan. Radial sequences carry equal “risk” for the effect of motion throughout the duration of the scan whereas Cartesian sequences will suffer most severely if motion occurs during the acquisition of the central few rows in k-space, typically half-way through the scan [11].

Not only is a radial sequence less sensitive to *when* motion occurs during a scan, but it is also less sensitive to *how* subject motion affects the final image. As mentioned earlier, incorrectly registered phase information in Cartesian sequences presents as ghosting artifact in the final image [18]. In 3D radial sampling, an artifact such as ghosting is not possible, since three orthogonal readout gradients are applied simultaneously and signal discrepancies, as a result of motion, are distributed between all three encoding dimensions [11]. This diminishes the appearance of artifacts in the final image. With radial sampling, motion artifacts appear as blurring or curvilinear intensities which radiate away from the scanned object and are easily distinguishable from the anatomy (Fig. 2.9) [19]. The artifacts are considered less interfering by radiographers [54] since more diagnostic information is preserved [55].

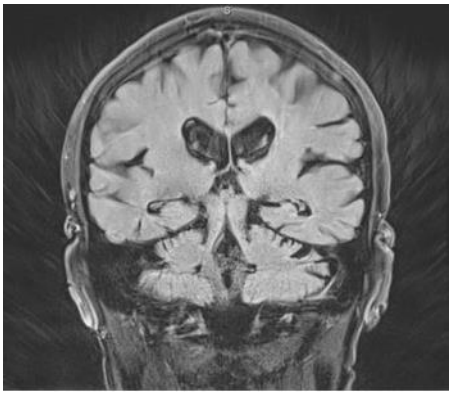

Figure 2.9. Typical motion artifacts displayed in images produced with a radial sampling technique [19].

Additionally, since radial spokes overlap one another at the k-space origin, the centre is over-sampled which has an averaging effect on signal discrepancies between spokes, further reducing the impact of motion on the final image [11]. Thus, radial sequences are described as inherently motion-robust, especially when compared to Cartesian sequences, making them a good choice in applications where motion is inevitable such as when imaging the moving fetus [56], [57].

2.4. Challenges of Radial MRI

Meeting the Nyquist Criterion

In order to accurately measure a signal and prevent aliasing artifacts, the digital sampling rate must be at least twice that of the frequency of the signal [13]. This translates into a sampling requirement called the Nyquist condition which states that the distance between neighbouring samples must be less than or equal to the inverse of the field of view (FOV) [13] . A radial sampling scheme requires unique definitions for the sampling requirements to meet the Nyquist criterion, since the distance between adjacent sampled points is more complicated to visualize for a 3D spherical field of view than for a uniform 3D cube.

A spherical volume is most efficiently sampled when an isotropic resolution is achieved. This is achieved when $\Delta k_r = \Delta k_\theta = \Delta k_\varphi$ [58].

The following derivation is an extension of one that can be found in [59] and [58]. Assume that the end point of each radial projection is associated with an area (ΔS) on the surface of a sphere.

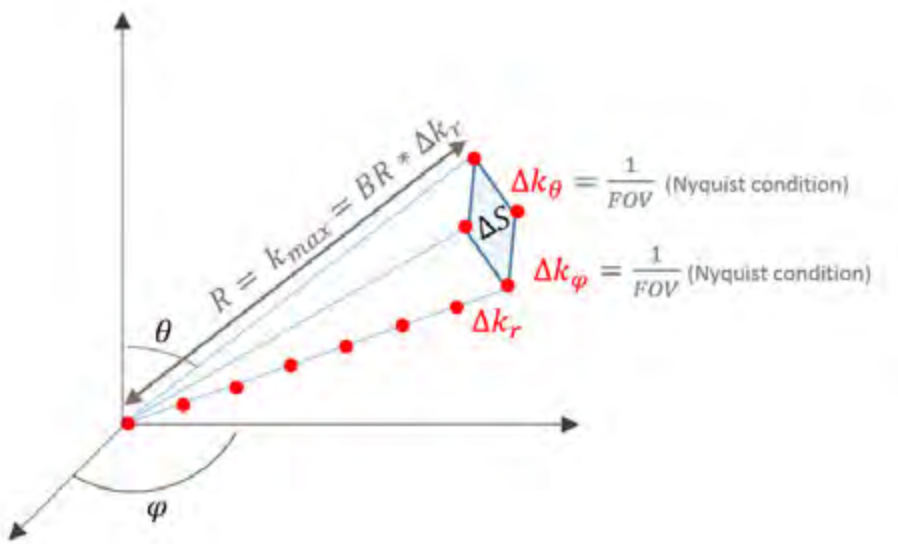

Figure 2.10. Illustration to show the relevant dimensions associated with a radial projection in 3D k-space

Therefore this area can be represented as:

$$\Delta S = \Delta k_\theta * \Delta k_\varphi = (\Delta k_\theta)^2, \text{ to achieve isotropic resolution} \quad (2.6)$$

and,

$$\therefore \Delta S = \left(\frac{1}{FOV}\right)^2, \text{ to obey the Nyquist condition.} \quad (2.7)$$

To cover the entire surface area of a sphere, we require:

$$S = N_{radii} * \Delta S, \quad (2.8)$$

where N_{radii} is the number of radial projections. This can be rearranged to determine the number of radial projections required to achieve isotropic resolution:

$$N_{radii} = \frac{S}{\Delta S}$$

$$N_{radii} = \frac{4\pi R^2}{\Delta S}$$

$$N_{radii} = \frac{4\pi {k_{max}}^2}{\left(\frac{1}{FOV}\right)^2}$$

$$N_{radii} = \frac{4\pi(BR * \Delta k)^2}{(\Delta k)^2}$$

$$N_{radii} = 4\pi(BR)^2. \quad (2.9)$$

For diameter readouts, such as those implemented in this work, this number can be halved to determine the number of diameter projections required:

$$N_{diam} = 2\pi(BR)^2, \quad (2.10)$$

where *BR* is the number of sampled points along a projection i.e. the base resolution. Therefore, for a particular base resolution, equation 2.10 gives the required number of projections to be sampled such that the Nyquist condition is satisfied. However, it is often impractical to acquire sufficient spokes to achieve isotropic coverage of k-space with radial sampling. For example, for a standard base resolution of 128:

$$N_{diam} = 2\pi(BR)^2 = 2\pi(128)^2 \approx 10\ 2944\ \ projections.$$

For a typical sequence with TR = 10ms, the total scan time would be ≈ 17 minutes. Therefore, in reality 3D radial sequences are necessarily under-sampled to achieve more practical scan times [11], [58]. The ability to still produce an image of reasonable quality is owed to the characteristic over-sampling of the central region in k-space [11]. However, the fewer radial projections that are reconstructed into an image, the larger the distance between the outermost samples grows. This results in Nyquist artifacts which are characteristically described as streaking patterns. (Fig 2.11) [11].

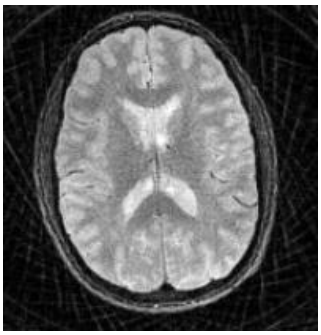

Figure 2.11. Example of streaking artifacts due to a reduced number of radial spokes [60].

In practice it is sometimes acceptable to sample with so few radial spokes that streaking artifacts are inevitable, because often they appear outside the region of interest for the scanned object and therefore do not interfere with the diagnosis [11]. However, when even fewer radial spokes are acquired, the radius at which streaking artifacts begin to occur will eventually overlap the scanned object [11]. This presents a challenge in navigation applications where the aim is to use as few spokes as possible to construct sufficiently rapid navigator images since streaking artifacts may interfere with the image quality. Still, contrary to an equivalent Cartesian scan, for heavily under-sampled radial scans, much of the object information is retained [11], [55] providing further support for the viability of radial sampling for 3D real-time navigation during fetal MRI.

2.5. Motion Detection and Correction Strategies for Fetal MRI

As mentioned earlier, even with the rapid imaging techniques such as those applied in 2D SST2W scans, fetal motion can still occur between the acquisitions of slices confusing the orientation of different slices in the final stack [6]. For research purposes where structural analysis is performed, it is required that 2D sequences are combined into a single 3D volume [61] but this relies on the continuous correspondence of voxel positions between slices [6]. Therefore motion-correction strategies have necessarily been developed for recovery of motion-corrupted fetal MRI data.

These strategies can include prospective motion-correction, where the sequence can be updated in real-time such that the scanner gradients are adjusted to "follow" the anatomy of interest as it moves throughout the scan [6]. These can come in the form of sequence navigators, self-navigating sequences or motion-correction devices [10]. Alternatively, motion can be retrospectively corrected through post-processing techniques but these have the disadvantage of being subjected to "spin-history" effects where shifting tissues that have experienced different RF pulse amplitudes during the scan, reflect in the final corrected volume with variations in their signal intensities [6]. Additionally, if the fetus shifts from the field of view, the target scan information cannot be recovered. Therefore, prospective navigation techniques should be the ultimate end-goal for fetal MRI. The post-processing used in fetal applications to date are computationally expensive and require further development to become more appropriate for clinical use [10].

Current methods of navigation for abdominal imaging involve tracking the motion of the diaphragm [62]. This method has been translated to fetal MRI applications with promising results however, in such applications, the scan time of the single-shot T2 weighted sequence into which the navigator was inserted, increased from the usual sub-30 seconds to about 7 minutes and it was not always able to track the motion when the fetus was particularly restless [63], [10]. A pilot scan was also required to position the navigator on the fetal brain and this process sometimes had to be repeated which further increased the scan time [63]. There are currently no practical options for navigation during fetal scans and artifact-corruption in many different forms by fetal and maternal motion remains a largely unresolved issue.

2.6. Reconstruction of Radially Sampled Data

Changing the k-space sampling scheme from parallel lines to radial spokes complicates the image reconstruction process. The MR images are reconstructed from k-space data using the Fourier Transform (FT) mechanism [13]. The relationship between the image intensity values, $m(\vec{r})$, and the measured MR signal, $M(\vec{k})$, is given by

$$M(\vec{k}) = \int m(\vec{r}) e^{-i2\pi\vec{k}\vec{r}} d\vec{r}, \tag{2.11}$$

where the integral is evaluated over the field of view (FOV),

$$\vec{k}(t) = \gamma \int_0^t \vec{G}(\tau) d\tau \tag{2.12}$$

and,

$$\vec{G}(t) = \left(G_x(t)\ ,\ G_y(t)\ ,\ G_z(t)\right). \tag{2.13}$$

The image intensity values at discrete positions are therefore given by the inverse Fourier Transform (IFT) of the k-space data, $M(\vec{k})$, evaluated over the volume sampled in k-space, according to the equation

$$m(\vec{r}) = \int M(\vec{k}) e^{i2\pi\vec{k}\vec{r}} d\vec{k}. \tag{2.14}$$

The above formula requires uniformly sampled points in k-space at every location $\vec{k}_j$. However, with radial imaging, the sampled points do not fit neatly onto a regular Cartesian grid, nor are they equidistant, and so applying the IFT directly becomes laborious and impractical for clinical scanning even with extremely powerful computers. Additionally, the centre of k-space where all the radial spokes intersect is more densely sampled than the periphery, resulting in blurred images with poor edge detail. Various reconstruction algorithms exist for non-Cartesian sampled data, each with characteristic image artifacts resulting from imperfect estimations.

Siemens Reconstruction Algorithm for Radially Sampled Data

The Siemens Image Reconstruction Environment (ICE) interpolates the radial k-space data onto a regular Cartesian grid prior to Fourier Transform using an algorithm developed and described in a paper by Sonia Nielles-Vallespin (2004, [58]). This paper forms the basis of this description of the method below.

Interpolation in k-space

In this work, re-gridding interpolation is performed prior to performing the IFT. In radial imaging, the sampled points along a diametric spoke lie somewhere between the vertices of a regular Cartesian grid and so each sampled point must be reassigned as accurately as possible to the nearest Cartesian grid points. This process extends beyond a simple nearest-neighbour interpolation since, for radial samples that lie exactly between two Cartesian points, the interpolation error would be unacceptably large.

Interpolation of radial spoke data is performed by convolving the data with a window function (convolution kernel) $C(k_x, k_y, k_z)$ which, in this instance, is a Kaiser-Bessel function with good interpolation accuracy and reasonable computational expense.

The window function is of the form:

$$C(k) = \begin{cases} \frac{1}{W} I_0\left[\beta\sqrt{1-\left(\frac{2k}{W}\right)^2}\right] for\ |k| \le \left(\frac{W}{2}\right), \\ 0\ otherwise \end{cases}, \tag{2.15}$$

where:

- *W* is the kernel width with an optimized value of 3.0 [64].
- $I_0(k)$ is the modified Bessel function of the first kind (order zero)
- β is a shape parameter optimized to be 4.2054 [64].

During re-gridding of a radially sampled point $M(\overrightarrow{k_j})$, the window function $C(\Delta\vec{k})$ is evaluated with respect to $\overrightarrow{k_j}$ for each Cartesian grid point $\overrightarrow{p_i}$ that lies a distance $\Delta k \le \frac{W}{2}$ from $\overrightarrow{k_j}$. The radial sample is

then multiplied by the convolution kernel at each $\overrightarrow{p_i}$ and thereby interpolated to the relevant Cartesian grid point, forming a matrix of gridded data $m(\vec{p})$. The value of the convolution kernel for each Cartesian grid point is added into a density matrix $D(\vec{p})$, to be used at a later stage. This process is repeated for every radially sampled point.

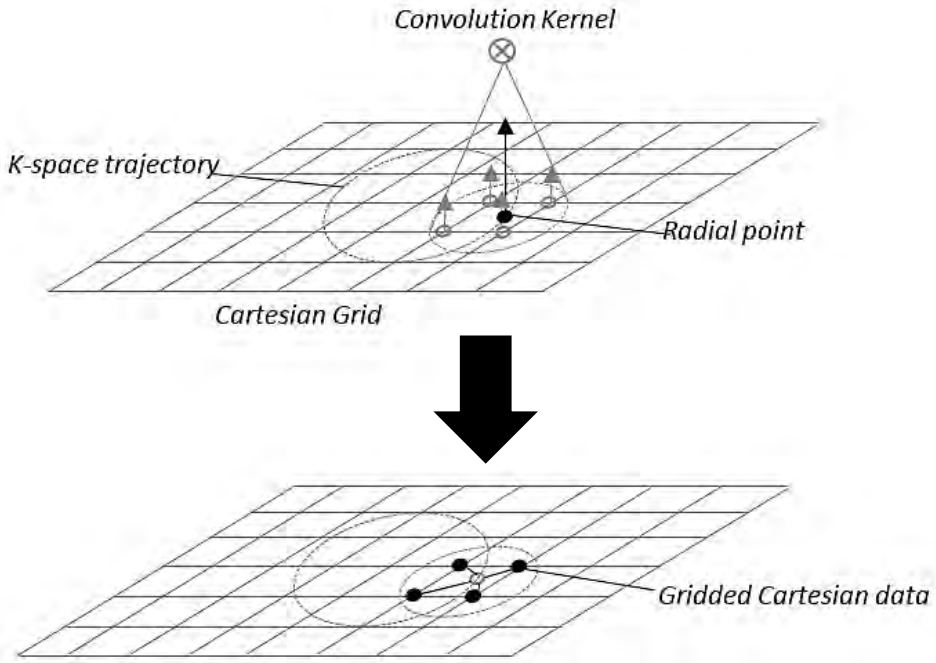

Figure 2.12. To show the process of calculating the convolution kernel for the relevant Cartesian grid points, before distributing the radial data between these points.

Density Compensation

With radial sampling, k-space is sampled along a set of diametric spokes that pass through the centre of k-space each time. If re-gridding was applied directly to a radial data set, many points sampled near the centre of k-space would be assigned to the same Cartesian grid points, whereas some Cartesian points on the periphery of the sampled volume may not be assigned to a radial sample at all. Recall that only Cartesian points $\overrightarrow{p_i}$ a distance $\Delta k \leq \frac{W}{2}$ from a radial sample will be assigned a portion of the signal whilst the remaining grid points will have a value of zero.

The result is an over estimation of the influence of Cartesian points in the centre of k-space (low spatial frequencies) and an under estimation of the influence of Cartesian points towards the edges (high spatial frequencies). As high spatial frequencies contain edge information about the scanned object, the output images appear blurry since they lack a balanced contribution from these frequencies. To avoid this, density compensation must be included in the reconstruction process.

Pre-compensation

When the sampled data is interpolated onto a Cartesian grid, the original position of each sampled point is lost. Therefore, a density compensation step must be performed prior to re-gridding. This is achieved by multiplying each radially sampled point $M(\overrightarrow{k_j})$ by an appropriate weighting function $\omega(\vec{k}_j)$ that is proportional to the inverse of the sample density:

$$\omega(k_x, k_y, k_z) = \frac{1}{\rho(k_x, k_y, k_z)}, \tag{2.16}$$

The weighting function used here is a rho filter originally developed for 2D radial reconstruction and defined for use in a 3D radial application by the expression:

$$\omega_n = \frac{1}{6N}\pi[(k_{n+1})^3 - (k_n)^3], \tag{2.17}$$

where *N* is the total number of radially sampled points, k_n is the distance of the sampled point from the centre of k-space, and k_{n+1} is the radius of the next most distant point along the spoke from the centre of k-space. These variables are illustrated in Figure 2.13.

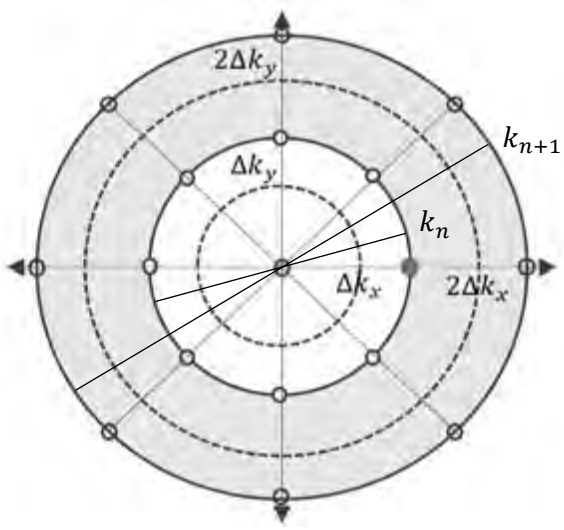

Figure 2.13. Figure to illustrate the parameters in the equation for the rho filter. Each radial sample is multiplied by the volume of the surrounding cell. Adapted from [58].

To demonstrate, assume a radially sampled point that is one of eight points on the surface of a sphere with diameter k_n. To weight this sample using the rho filter, it is multiplied by one eighth of the difference between the volume of the sphere on which the next point sampled along the radial spoke lies, given by $(\frac{4\pi}{3}(k_{n+1})^3)$, and the volume of the sphere on which the point itself lies, given by $(\frac{4\pi}{3}(k_n)^3)$. The weighting factor is also divided by the total number of radially sampled points *N.* Therefore, sampled points with high spatial frequencies that are more sparsely distributed, are multiplied by a larger weighting factor, and the points closest to the centre of k-space are multiplied by a smaller weighting factor. In this way, the sample density is balanced across the data set before the re-gridding kernel is applied.

Post-compensation

As described previously, the value of the window function $C(\Delta\vec{k})$ is evaluated for every Cartesian grid point $\overrightarrow{p_i}$ during re-gridding. Each grid point is assigned portions of signal from nearby radial samples,

which are successively added to originally empty voxels within the Cartesian array $m(\vec{p})$. Since a single Cartesian voxel may be assigned multiple radial signal contributions, particularly for grid points near the centre of k-space, there will be grid points with a stronger influence than others. For each Cartesian voxel, the values of the window function from all the radial signals that contribute to that voxel are summed and entered into the corresponding position in another originally empty matrix with the same dimensions as the Cartesian array. This matrix, which contains information about the density distribution used to construct the 3D Cartesian matrix, $m(\vec{p})$, is referred to as the density matrix $D(\vec{p})$. Finally, the Cartesian array is divided by the density array to generate a normalised Cartesian array $m_D(\vec{p})$.

3D Inverse Fourier Transform

Re-gridding and density compensation yield a uniformly sampled Cartesian array of k-space data in which the grid points contain interpolated MRI signal information from the radially sampled object. The image is reconstructed by applying an Inverse Fourier Transform over the k-space field of view using the following equation

$$m(x,y,z) = \int m_D(k_x,k_y,k_z)e^{i2\pi(k_x x+k_y y+k_z z)}dk_x dk_y dk_z. \quad (2.18)$$

De-apodisation

One disadvantage of convolution with the rapidly-decaying Kaiser-Bessel window is signal drop-off towards the edges of the image, known as apodisation [58]. To compensate for this, after an IFT has been applied to the Cartesian array, the inverse Fourier Transform of the window function (convolution kernel) is calculated and each Cartesian data point is then divided by this result. The FT of the Kaiser-Bessel function is given by:

$$c(x) = sin\sqrt{\pi^2W^2x^2-\beta^2}/\sqrt{\pi^2W^2x^2-\beta^2}\,, \quad (2.19)$$

where the optimal values for *W* and β are as specified previously, namely 3.0 and 4.2054, respectively.

Implementation of Reconstruction Algorithm

The flow diagram in Figure 2.14 shows how these steps are implemented in the Siemens gridding algorithm.

Step 1: PRE-COMPENSATION

A radial sample with MRI signal value $M(\overrightarrow{k_j})$ is multiplied by the weighting function: $\omega_n = \frac{1}{6N}\pi[(k_{n+1})^3 - (k_n)^3]$	Density-compensated radial sample: $M_\omega(\overrightarrow{k_j})$

Step 2: RE-GRIDDING

The Kaiser-Bessel window function $C(\Delta\vec{k})$ is evaluated for each Cartesian grid point $\overrightarrow{p_i}$ within a distance of $\Delta k \leq \frac{W}{2}$ with respect to $\overrightarrow{k_j}$	The value of the window function for each Cartesian grid point is added to the relevant voxel in a separate density matrix $D(\vec{p})$

Step 3: RE-GRIDDING

The weighted radial sample $M_\omega(\overrightarrow{k_j})$ is multiplied by the convolution kernel $C(\Delta\vec{k})$ at each of the relevant grid points $\overrightarrow{p_i}$.	This process is repeated for each radial sample point. The interpolated data generates a Cartesian array $m(\vec{p})$

Step 4: POST-COMPENSATION

The Cartesian array $m(\vec{p})$ is divided by the density array $D(\vec{p})$ resulting in a Cartesian array with uniform sampling density $m_D(\vec{p})$

Step 5: 3D FAST FOURIER TRANSFORM (FFT)

A 3D FFT is applied to the Cartesian data set $m_D(\vec{p})$ to generate an image: $m(\vec{x})$

Step 6: DEAPODISATION

The Fourier Transform of the Kaiser-Bessel window function $C(\Delta\vec{k})$ is calculated; $c(\vec{x})$	Each cartesian data point in $m(\vec{x})$ is divided by the transformed convolution kernel $c(\vec{x})$

Figure 2.14. A schematic illustrating the steps within the Siemens radial-to-Cartesian gridding algorithm.

3. Methods

3.1. Sequence Development

The MRI sequence modified in this project was the Siemens Cardiovascular (CV) pulse sequence, developed to perform MR imaging of the beating heart. It can be run in TRUFI (true fast imaging with steady state free precession) or GRE (gradient echo) mode and has both two-dimensional (2D) and three-dimensional (3D), as well as Cartesian and radial settings.

Optimizing the Gradient Echo Setting

T1-weighted images of the fetal brain allow for the detection of haemorrhages, calcification and fat deposition, and in later stages of gestation they provide useful information on bone density and development [27]. Since the gradient echo sequence can provide T1-weighted images, it was considered more appropriate than the TRUFI sequence to be developed further in this project.

Additionally, a gradient echo sequence is able to accommodate rapidly varying readout gradients, which allow for more freedom in designing a new radial trajectory. In contrast, TRUFI sequences are particularly sensitive to eddy current artifacts unless consecutive readout gradients are minimally varied, which would limit the possible k-space encoding strategies [65]. For these reasons, the GRE mode of the CV sequence was chosen to serve as the foundation sequence for editing in this project.

A standard gradient echo sequence can implement very short repetition times (TR) useful for fast MR imaging. However with such short TR's, there may be a transverse component of magnetization remaining before the application of the next radio frequency (RF) pulse, even if smaller flip angles are used. Residual transverse magnetization is an important consideration in gradient echo sequences. If left alone, the residual transverse magnetization will accumulate and contribute to the readout signal making it difficult to control the image contrast. To address this issue, spoiler gradients were added to the GRE sequence to destroy any remaining transverse magnetization by dephasing spins prior to each RF pulse, so that only the desired longitudinal magnetization contributes to the signal.

The pulse sequence diagram in Figure 3.1 illustrates the modified 2D radial gradient echo sequence with the addition of spoiler gradients after analogue-to-digital conversion (ADC). Readout occurs over the acquisition time (T_{acq}) and the echo time (TE) is the time between RF pulse application and mid-way through readout. The repetition time (TR) is the time between successive RF pulses. The way in which k-space is filled, is illustrated graphically next to the pulse sequence diagram for the pair of phase and readout gradients indicated with the solid line. Varying the phase encode gradient through all possible values for the indicated maximal readout, and vice versa, will generate a series of spokes passing through the centre of k-space. After readout, spoiler gradients (d) are applied. Note that these gradients are a constant magnitude regardless of the magnitudes of the preceding readout and phase encode gradients.

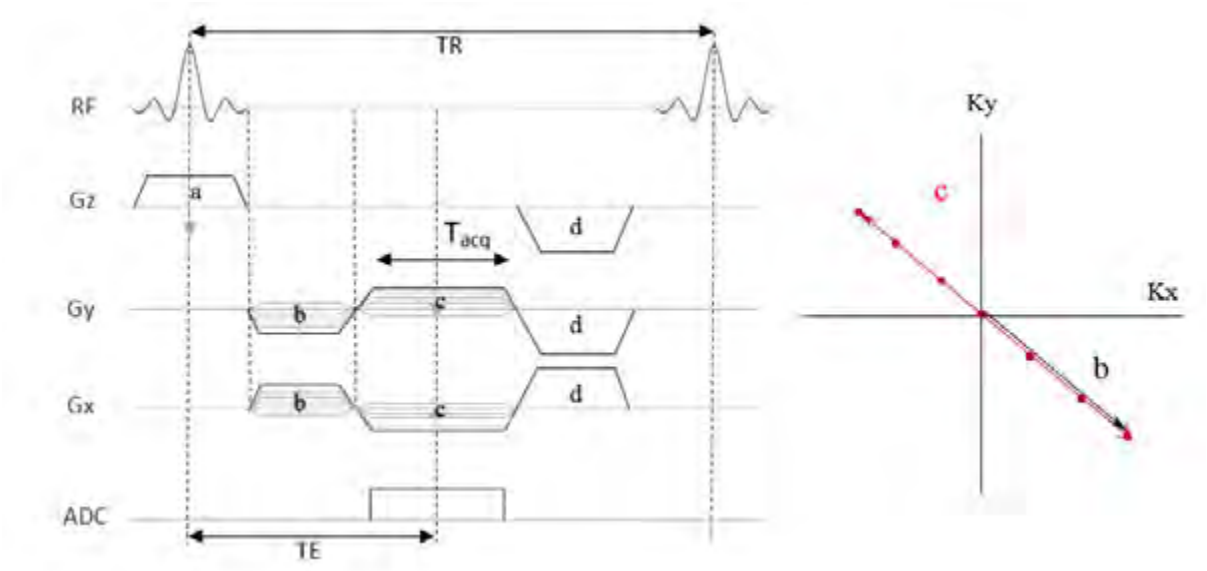

Figure 3.1. Pulse Sequence Diagram for the modified 2D radial gradient echo sequence where 'a' is a slice-selective gradient in the Gz encoding direction, 'b' is a pre-phasing gradient for Gx and Gy in the frequency (Kx) and phase (Ky) encoding directions, respectively, 'c' is the readout gradient for Gx and Gy. These gradients are applied simultaneously to generate a 2D spoke. Finally, 'd' represents the spoiler gradients for Gz, Gy and Gx added into the sequence to destroy residual transverse magnetization before each RF pulse excitation.

The modified GRE pulse sequence therefore resembles a FLASH (Fast Low Angle Shot) sequence that achieves T1 contrast with large flip angles and proton-density weighting with small flip angles.

The steady state signals for a FLASH sequence is given by:

$$S = \frac{\rho\left(\left(1 - e^{-TR/T_1}\right)e^{-TE/T_2^*}\sin\alpha\right)}{1 - \cos\alpha \,.\, e^{-TR/T_1}}, \tag{3.1}$$

where α is the flip angle, ρ is the proton-density factor, and T_1 and T_2* are longitudinal and observed transverse relaxation times of the imaged tissue, respectively.

The maximum signal is achieved at the Ernst Angle (α_E) for a given TR and T_1 and is given by:

$$\alpha_E = \arccos\left(e^{-TR/T_1}\right). \tag{3.2}$$

These equations are useful for determining the optimum flip angle in the scanning protocol which will be discussed in section 3.2.

Method for Sampling a 3D Spherical Volume in k-Space

In 3D radial imaging, all three gradients G_Z, G_Y and G_X are applied simultaneously, to sample a diametric spoke in k-space, passing through the origin, $\overrightarrow{k_0} = (0,0,0)$, with end points that lie on the surface of a sphere.

The net gradient vector, $\overrightarrow{G}$, determines the direction of a readout diameter and is oriented in k-space by the polar angle θ and azimuth angle $\emptyset$, measured from the positive Kz and Kx axes, respectively. Figure 3.2 illustrates an arbitrarily oriented gradient vector and the relevant vector components.

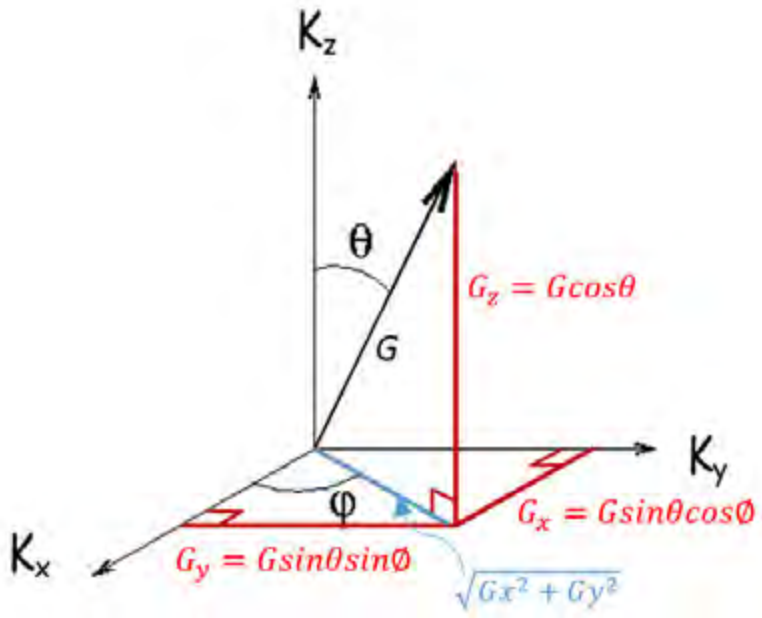

Figure 3.2. Figure to show the component vectors of gradient G in three-dimensional k-space.

The magnitude of vector $\vec{G}$ and spherical angles θ and $\emptyset$ are given in terms of their component gradients G_Z, G_Y and G_X:

$$G = \sqrt{G_x^2 + G_y^2 + G_z^2} \tag{3.3}$$

$$\emptyset = \arctan\left(\frac{G_y}{G_x}\right), \quad 0 < \emptyset < 2\pi \tag{3.4}$$

$$\theta = \arccos\left(\frac{G_z}{\sqrt{G_x^2 + G_y^2 + G_z^2}}\right), \quad 0 < \theta < \pi. \tag{3.5}$$

The individual components of vector $\vec{G}$ in spherical coordinates are:

$$G_x = Gsin\theta cos\emptyset, \quad G_y = Gsin\theta sin\emptyset, \text{ and } G_z = Gcos\theta. \tag{3.6}$$

By extension, since $\vec{k}$ is related to $\overrightarrow{G}$ by $\overrightarrow{k(t)} = \gamma \int_0^t \vec{G}(t)\, dt$, where γ is the gyromagnetic ratio,

$$k = \sqrt{k_x^2 + k_y^2 + k_z^2} \tag{3.7}$$

and,

$$k_x = ksin\theta cos\emptyset, \quad k_y = ksin\theta sin\emptyset, \text{and } k_z = kcos\theta. \tag{3.8}$$

In order to sample a 3D spherical volume in k-space, many diametric spokes must be sampled by varying the spherical angles in successive readouts. Before each readout, pre-phasing gradients first achieve the desired orientation and starting point for the diameter to be sampled. During readout, the diameter is sampled at regular intervals (Δk_r) along its length. Since the diameter lengths are constant, the end points lie on the surface of a sphere (Fig. 3.3).

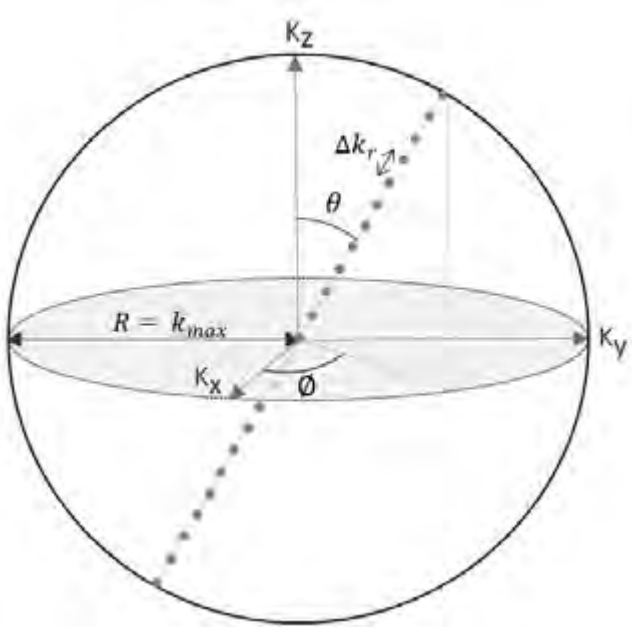

Figure 3.3. A 3D diametric spoke oriented by spherical angles θ and $\emptyset$, with end points that lie on the surface of a sphere in k-space.

Various algorithms exist to sample 3D spherical volumes in this way, with different equations to determine the magnitude of the spherical angles. It is useful to distinguish the various schemes by observing the simplified sampling pattern generated by the diameter end points on the sphere's surface, often referred to as the "trajectory". It is however important to note that every diameter is sampled all along its length to fill k-space inside the sphere. Figure 3.4 is an example of a 3D radial sequence trajectory that only shows the starting points on the surface and orientation of each sampled diameter or "spoke". Using this convention it is clear that the starting points of the diametric spokes in Figure 3.4 generate a spiral trajectory on the surface of the sphere. Since each start point

generates an end point in the other hemisphere, the start points only need to fill the surface of one hemisphere, so that half a spiral trajectory is sufficient to fully sample k-space in a sphere.

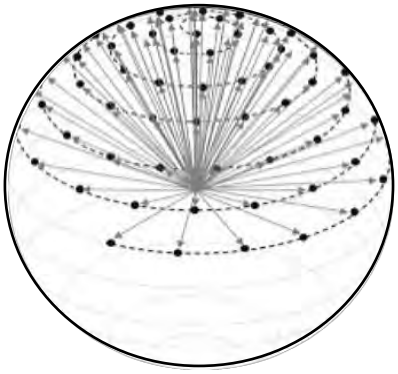

Figure 3.4. An example of a spiral trajectory on the surface of a sphere, where only the orientation and starting points of each diameter readout are illustrated.

Figure 3.5 shows the pulse sequence diagram for a radial sequence that samples one hemisphere with 256 projections.

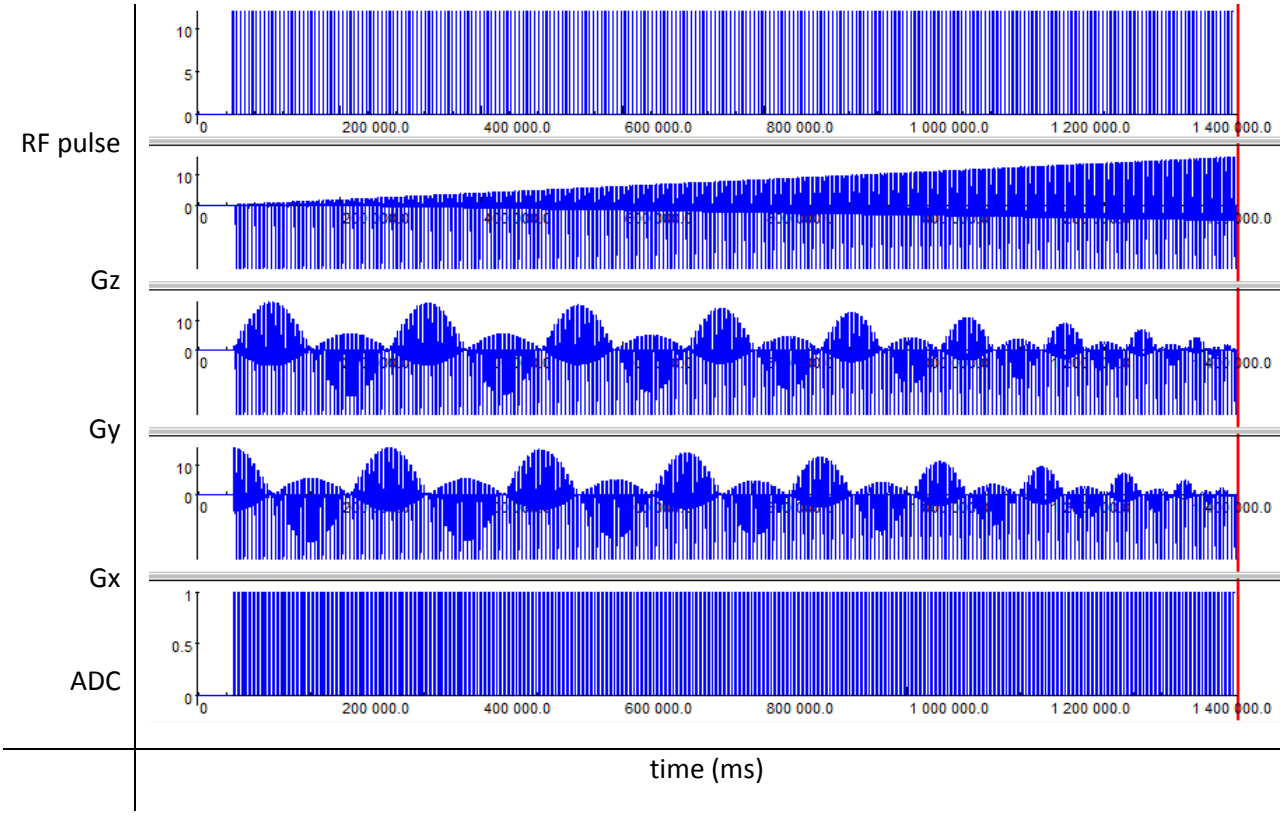

Figure 3.5. Pulse sequence diagram to sample a 3D hemisphere using a spiral trajectory consisting of 256 projections.

Siemens Radial Trajectory

The radial sampling trajectory implemented in the Siemens Cardiovascular (CV) sequence is based on the equations by Saff and Kuijlaars [66] given below.

$$G_z(n) = -\frac{1(n-1)}{N-1}, \qquad 1 \leq n \leq N \tag{3.9}$$

$$\theta(n) = \arccos\big(G_z(n)\big) \tag{3.10}$$

$$\emptyset(n) = \left(\emptyset_{n-1} + \frac{3.6}{\sqrt{N(1-G_z^2)}}\right) mod(2\pi), \qquad 2 \leq n \leq N-1 \tag{3.11}$$

With this method, the user has control of only a single variable, *N*, which is the total number of projections sampled during one acquisition. Therefore, scanning with this sequence would output a single 3D spherical volume of data. In this project, multiple volumes of data were required from a single acquisition, so that navigator images could be reconstructed from each sub-volume. As such, a new trajectory was required that enables the user to specify not only the total number of projections, but also the number of individual sub-volumes that would make up the total data set acquired.

Strategy for a Segmented Scan with Multiple Sub-spirals

A new sampling trajectory was developed, based on equations proposed by Wong and Roos [53], which distribute the end points between multiple spirals on the surface of the sphere. The equations contain two variables: *N*, the number of diameters to be sampled within one spiral pass (equivalent to *N* in the current Siemens implementation of the radial sequence) and a new variable, *M*, the number of interleaved spirals to be generated on the sphere's surface.

The trajectory was defined within the sequence by the following equations:

$$G_z(n) = \frac{n-0.5}{N}, \tag{3.12}$$

$$\emptyset(m,n) = \sqrt{\frac{2N\pi}{M}}\left(\frac{1}{sinG_z(n)}\right) + \frac{2m\pi}{M}, \qquad 0 < \emptyset < 2\pi, \tag{3.13}$$

and,

$$\theta(n) = arccosG_z\,, \qquad 0 < \theta < \frac{\pi}{2}, \tag{3.14}$$

where:

- $G_z(n)$ is the normalised gradient strength in the *Kz* encoding direction
- $\emptyset(m,n)$ and $\theta(m,n)$ are the spherical angles from which *Gx* and *Gy* are calculated
- *N* = The number of diametric spokes per sub-spiral
- *n* is a linear counter from *1* to *N*
- *M* = Total number of sub-spirals
- *m* is a linear counter from *1* to *M*

To illustrate this sampling strategy, a single spiral plotted in Matlab is presented in Figure 3.6.

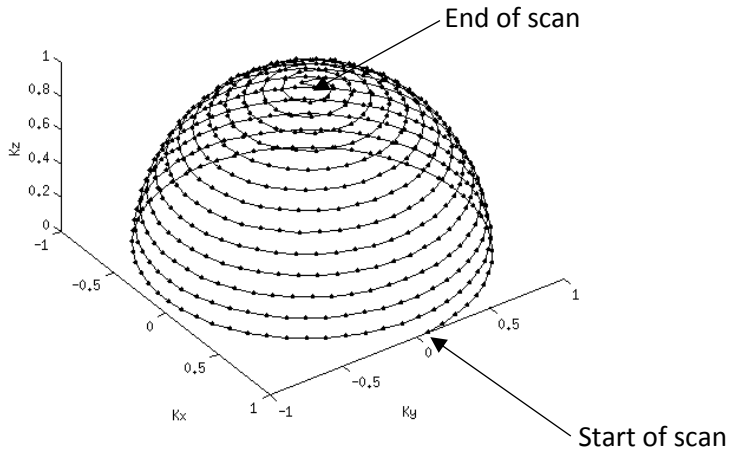

Figure 3.6. Trajectory of the starting points of the diametric spokes generated by equations (3.12) – (3.14) for one sub-spiral.

These equations define the starting points of each diametric spoke to be sampled at readout. The starting points generate a spiral trajectory on the surface of a hemisphere. Note, however, that the end points of the diametric spokes form a spiral trajectory on the opposite hemisphere, so that together the points fill the surface of the entire sphere. To illustrate this, both the starting and end points of each sampled diameter are shown for a half-spiral trajectory in Figure 3.7. Notably, this is a simplified representation of the actual acquired 3D data set since the spherical volume is also filled when the diameters are sampled, as illustrated by the orange line for one diametric spoke in Figure 3.7.

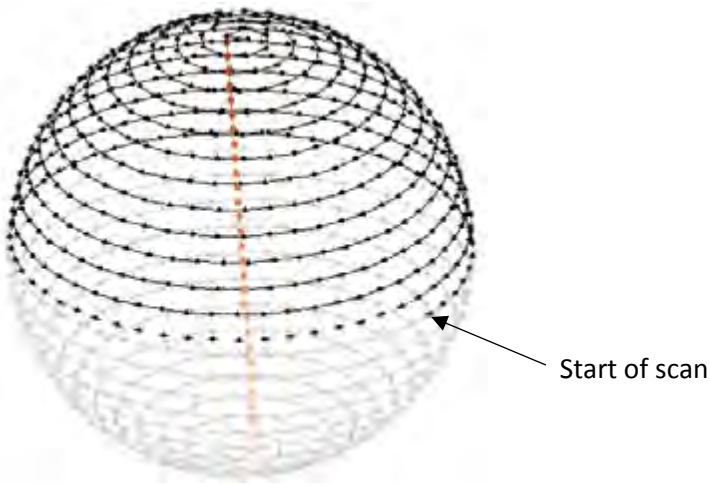

Figure 3.7. The starting (black) and end points (grey) of the diametric spokes for a single half-spiral trajectory cover the surface of the entire sphere. A single sampled diametric spoke is shown in orange to illustrate that points are sampled within the entire spherical volume and not just on the surface.

This new trajectory allows two variables, M and N, to be manipulated to acquire multiple sub-volumes of data (such as the ones plotted in Figures 3.6 and 3.7) within a single acquisition, resulting in a segmented scan. Each sub-spiral is complete within itself comprising both high and low spatial frequencies and covering the k-space field-of view (FOV) from pole to pole. When combined, the sub-spirals interleave to generate a completely filled volume of data as shown in Figure 3.8.

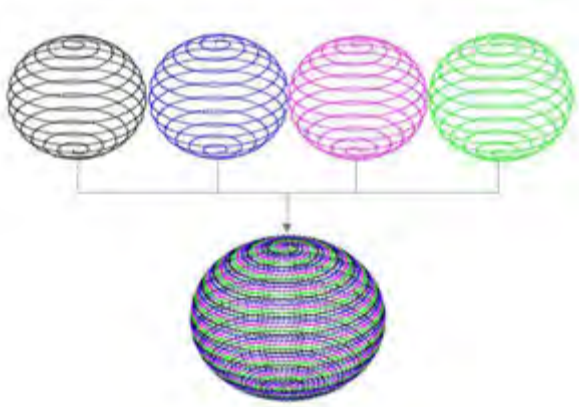

Figure 3.8. Schematic illustrating a complete 3D spherical volume of data, made up of four individual sub-volumes of data.

The pulse sequence diagram in Figure 3.9 generates four interleaved sub-spirals (*M*=4), each comprising *N*=64 diametric spokes, for a total of 256 projections.

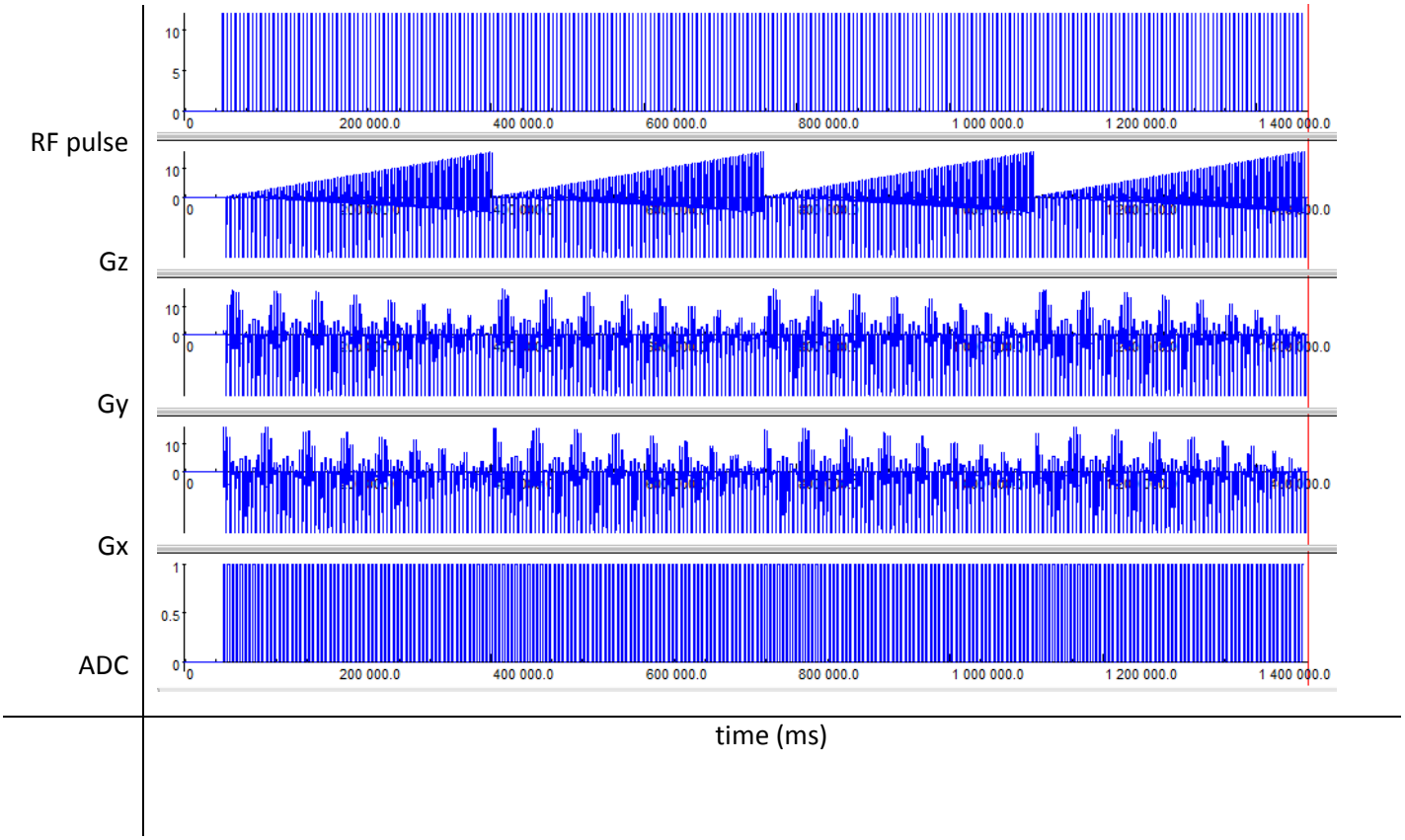

Figure 3.9. Pulse sequence diagram for four interleaved sub-spirals consisting on N = 64 diametric spokes each. Total number of spokes acquired = 256.

A segmented scan is suited to self-navigation, as successive low-resolution images generated by individual sub-spirals can be co-registered to quantify and correct motion. This process will be described in a later chapter but it is necessary to note here that the coding of the new sequence trajectory played an important role in successful reconstruction and registration in this project.

The user now has control over two parameters within the sequence. Firstly the user can specify the number of spiral passes to be completed within an acquisition, i.e. the number of separate and complete spherical data sets (*M*). Secondly, the user has control over the number of spokes to be sampled within each sub-spiral (*N*). The total number of diametric spokes per scan is given by *M*N*.

The parameters *M* and *N* can be optimized with respect to one another. Increasing the number of spokes within each sub-spiral (*N*) will increase the amount of signal per k-space voxel. This increases the signal-to-noise ratio (SNR) of navigator images, but will require a longer scan time to acquire each sub-spiral. Conversely, by increasing the number of sampled sub-spirals per scan (*M),* for a fixed number of spokes, temporal resolution of motion tracking is improved.

Four Different Sub-spiral Distributions

Four different sub-spiral distribution strategies were implemented and compared to determine the method that minimised artifacts in reconstructed navigator images and generated the highest resolution for the final combined volume.

a) Interleaved Sub-spirals

Initially, the equations by Wong and Roos (eqns. 3.12, 3.13, 3.14) were implemented exactly, which achieved a set of interleaved sub-spirals. Figure 3.10 shows the start and end points of the diametric spokes for this sampling scheme for two interleaved sub-spirals comprising 512 diametric spokes each, resulting in a total of 1024 projections. These values were chosen for demonstration purposes only as actual scan values are much larger.

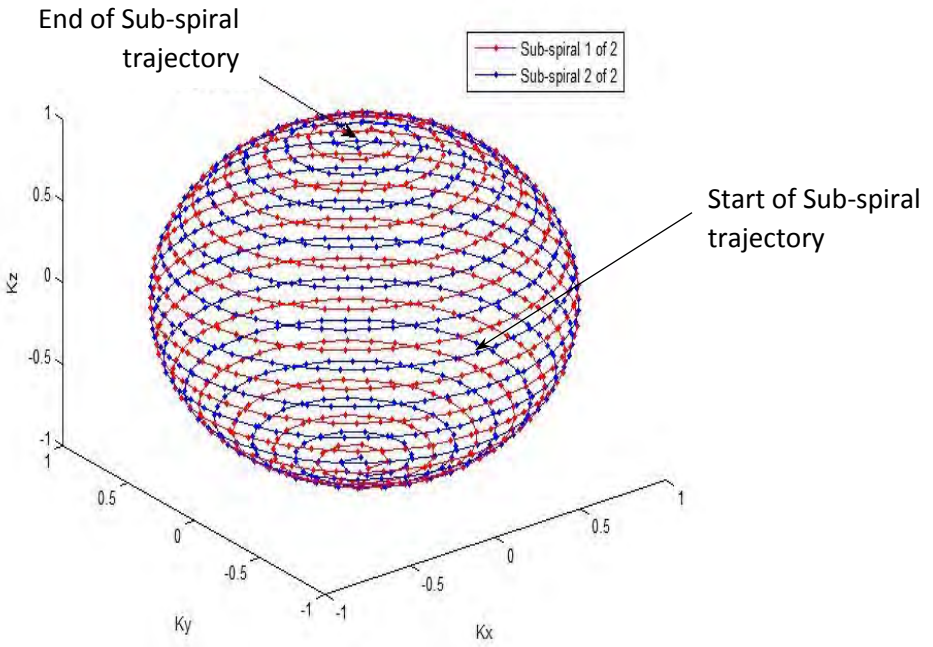

Figure 3.10. Two interleaved sub-spirals, each consisting of N = 512 diametric spokes.

b) Overlapping spirals

Next, overlapping spirals were investigated. With this distribution, the same spiral trajectory is followed in each sub-spiral pass. To achieve this, the original equations for a segmented scan were altered by setting *M*, which alters the azimuth angles ∅, to unity. As a result the azimuth angles (∅) are now the same for every sub-spiral and are given by:

$$\emptyset(n) = \sqrt{\frac{2N\pi}{1}}\left(\frac{1}{sinG_z(n)}\right), \qquad 0 < \emptyset < 2\pi, \qquad 1 < n < N\,. \tag{3.15}$$

The polar angle θ remains:

$$\theta(n) = arccosG_z\,, \qquad 0 < \theta < \frac{\pi}{2}, \qquad 1 < n < N. \tag{3.16}$$

In the source code, M remains the number of sub-spirals specified by the user although it no longer affects the values of the azimuth angle. These equations generate a series of overlapping spirals. Figure 3.11 shows start and end points of the diametric spokes for two overlapping spirals comprising 512 spokes each.

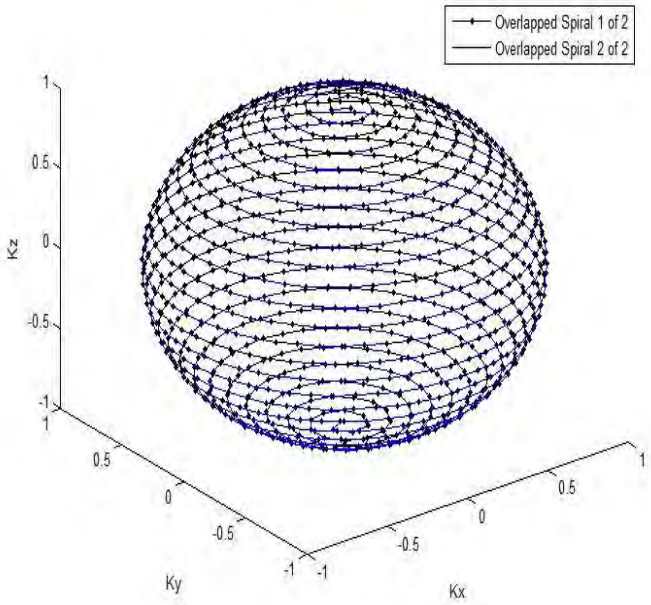

Figure 3.11. Two overlapping spirals, each consisting of N = 512 spokes. The combined volume has 1024 diametric spokes in total.

c) Rotated spirals

As an alternative to sampling the same points in each spiral pass, the equations were altered in such a way that the azimuth and polar angles are rotated along the spiral trajectory for successive sub-spirals by a distance inversely proportional to the number of sub-spirals specified (*M*).

The equations for the azimuth and polar angles become:

$$\emptyset(n,m) = \sqrt{\frac{2N\pi}{1}}\left(\frac{1}{sinG_z(n)}\right) + \frac{m}{M}\left(\emptyset(n+1) - \emptyset(n)\right), \qquad 0 < \emptyset < 2\pi, \tag{3.17}$$

and,

$$\theta(n,m) = arccosG_z + \frac{m}{M}(\theta(n+1) - \theta(n)), \qquad 0 < \theta < \frac{\pi}{2}, \tag{3.18}$$

where:

- n is a linear counter from 1 to N
- m is a linear counter from 1 to M

This samples a series of sub-spirals in a “cork-screw” manner, resulting in different sampled points for each new spiral i.e. rotated sub-spirals (Fig. 3.12).

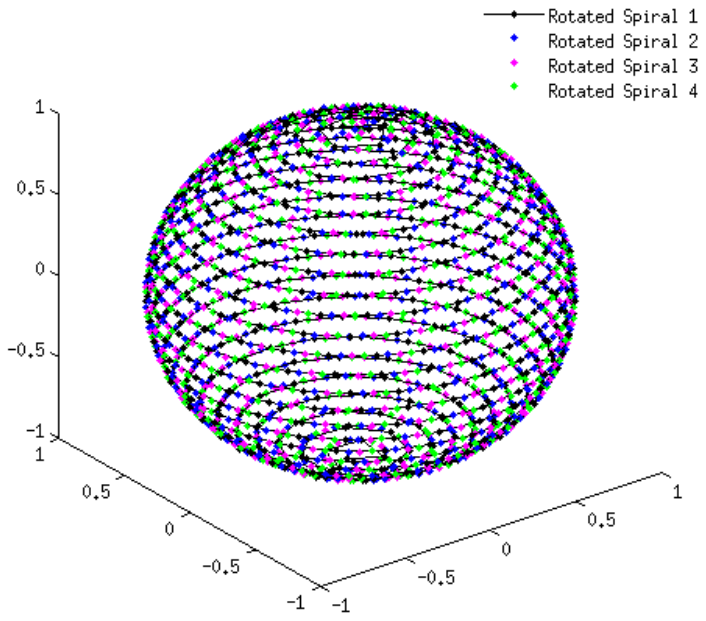

Figure 3.12. Four rotated sub-spirals each consisting of N=512 spokes

d) Indexed (Interleaved) sub-spirals

The fourth strategy was developed to acquire sub-spirals that uniformly sample the final combined volume. The azimuth and polar angles of the diametric spokes to fully sample the 3D volume were pre-calculated using the Wong and Roos [53] equations (3.12 to 3.14) for a single spiral (*M*=1) with the required number of total projections (i.e. *TP* = total number of projections). This generates vectors for both the azimuth and polar angles that have length *TP*.

For each sub-spiral, the gradient strengths are determined from the values of the azimuth and polar angles at the relevant index positions within the pre-determined vectors, resulting in an interleaved sampling of the points on the surface of the sphere. For example, when the total volume is to be made up of six sub-spirals, the first spiral’s gradients will be generated from the values at vector indices 1, 7, 13… etc. and the second will be generated from 2, 8, 14… etc.

In general, the indices (*i*) for sub-spiral *m* are given by:

$$i = m + (n - 1) * M, \tag{3.19}$$

where:

- m is the relevant sub-spiral, 1 < m < M
- 1 < n < N, and N is the number of diametric spokes per sub-spiral

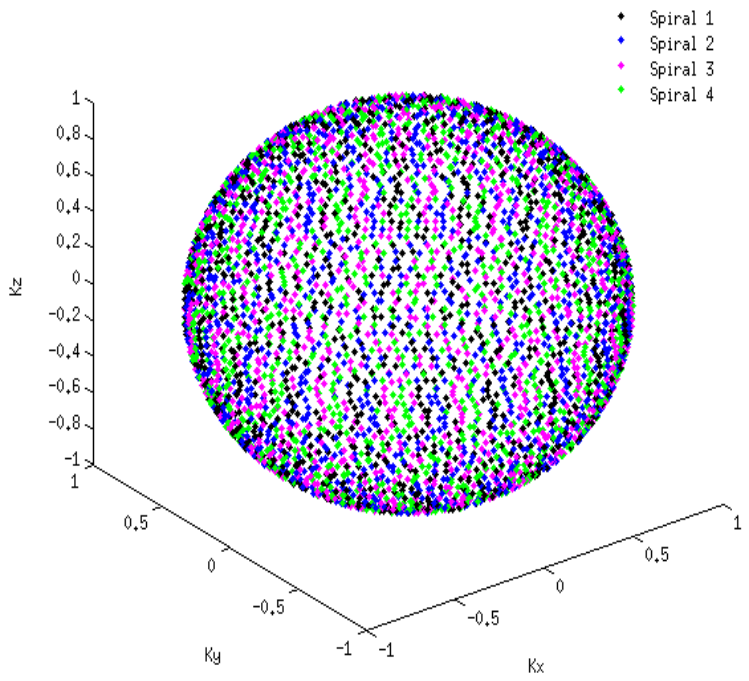

Figure 3.13. A combined volume showing start and end points of all diametric spokes for four sub-spirals, each with N = 512 spokes.

Comparison of Sub-spiral Distributions

To decide on the best sub-spiral distribution, the quality of reconstructed sub-spiral images was compared for the four different methods. Additionally, the image quality of the complete reconstructed data set after combining sub-spirals was assessed. The image quality in both cases was largely dependent on the presence of streaking artifacts which are a result of reconstructing the heavily under-sampled outer edges of the k-space field of view.

In order to evaluate the appearance of streaking artifacts within reconstructed sub-spiral images, phantom scans were performed using a Siemens 32 channel head coil. Each of the four sub-spiral distribution methods were implemented with the following scan parameters: 256 mm FOV, 128 x 128 x128 matrix size, 4^{o} flip angle, TE/TR 2.18/5.8 ms, 399 Hz/px. The total number of diametric readouts was set to 4096 and four sub-spirals (*M*=4) were acquired, each consisting of 1024 spokes (*N*=1024).

The sub-spirals were reconstructed offline using customized Siemens Image Calculation Environment (ICE) code for the CV sequence, which was modified to expect the incoming data according to the four different trajectories. The code for custom reconstruction is explained further in section 3.4. The end-point trajectory for the diametric readouts was also simulated in Matlab for each reconstructed image, to illustrate the simplified sampling distribution in k-space and thereby determine a correlation between the sampling distribution and the presence of streaking artifacts.

An additional simulation was performed in Matlab to illustrate the final sampling distribution for the combined volume when eight sub-spirals (*M*=8) of *N*=512 spokes each (*TP* = 4096) are acquired compared to when a single spiral (*M*=1) of *N*=4096 is acquired. The number of sub-spirals was increased to eight for this exercise to demonstrate the effect of increasing the number of sub-spirals on the sampling distribution for the combined volume, which is related to the achievable resolution of the reconstructed image.

The two methods that uniformly sample the combined volume, namely the interleaved and indexed sub-spiral distributions, were then compared for an increased number of sub-spirals. A phantom scan was acquired for each method with M increased to 12 for a constant *TP* = 12288 (*N* = 1024) to examine the effect of increasing M on the streaking artifacts present in the sub-spiral images. Scan parameters were kept as: 256 mm FOV, 128 x 128 x128 matrix size, 4^{o} flip angle, TE/TR 2.18/5.8 ms, 399 Hz/px.

3.2. Protocol Development

Once the 3D radial sequence had been developed, the scan protocol was optimized to ensure the sequence fulfilled the objectives of this project. Sequence parameters impact scan time, image contrast and image resolution. Often, increasing the effects of one parameter will require sacrificing the improvements made by another and so it was necessary to decide which improvements were most important, and to prioritise the optimisation of the relevant parameters.

Important scan parameters to consider were:

- *TR and TE (ms):* During each TR (time-to-repetition), one spoke is sampled. The longer the time between repeated RF pulse excitations, the longer the scan time. For 3D radial imaging, and especially for a navigating sequence, it was important to minimise the scan time and a good way to do this was to minimise the TR. Fortunately, with the sequence developed here, the use of a partial flip angle and spoiler gradients, allowed the TR to be reduced further than most other sequence types, making it ideal for fast imaging. In the sequence protocol, the TE (time-to-echo) was automatically minimized.

- *Field of View (FOV) and matrix size (mm^3):* The FOV is the sampling area in image space and the matrix size determines the spatial resolution. It was important to choose a FOV that included the entire abdomen of the participant being imaged. A FOV that is too small will lead to wrap-around artifacts in the output image. Therefore, the FOV was set on a patient-specific basis after an initial localizing scan. The matrix size was set to 128x128x128.

- *Receiver bandwidth (Hz/px):* Bandwidth determines the range of frequencies in the readout signal. Increasing the bandwidth results in noisier signals decreasing the SNR of the output image, but also speeds up the image acquisition. For example, doubling the bandwidth results in a decrease in SNR by a factor of $\sqrt{2}$. Since this radial sequence samples the centre of k-space with every spoke, the SNR of the output images is inherently high and so the bandwidth was one parameter that could be increased to decrease scan time.

- *Flip angle (α°):* The flip angle chosen for a particular sequence determines the signal intensity and affects the contrast in the final image. The flip angle that maximises signal intensity can be determined theoretically using the Ernst Angle equation. The flip angle is linked to the RF energy deposited into the system and so strict attention had to be paid to adhere to the SAR limits.

- *Total number of spokes, spokes per sub-spiral (N) and number of sub-spirals (M):* The total number of spokes acquired during the scan was chosen based on the image quality of the final 3D volume. The number of spokes per sub-spiral were chosen based on the quality of the navigator images. Minimising the number of spokes per sub-spiral reduced the length of time it took to acquire each sub-spiral, making it ideal for navigation purposes. However, streaking artifacts appeared when *N* was reduced too far and so the values for *N* and *M* needed to be optimized.

Parameter Optimisation

The MRI pulse sequence developed in this project was designed to run on a clinical whole-body scanner (3T Magnetom Skyra, Siemens Medical Solutions, Erlangen, Germany) equipped with a 45 mT/m gradient system (Siemens Quantum Gradients, slew rate of 200 T/m/s). A Siemens water phantom was used initially to develop the experimental procedures used in this work. Phantom scans

were performed using either a 32 channel Siemens head coil or an 18 channel body array flex coil depending on whether procedures were being developed for adult brain scans or abdominal scans, respectively.

Following phantom experiments, tests were conducted *in vivo* on healthy volunteers. In total, fourteen non-pregnant volunteers were recruited to partake in these experiments. Protocol development was performed in non-pregnant volunteers as for many of the tests the absence of a fetus would not compromise the validity of the results. Furthermore, for ethical and comfort reasons, pregnant mothers could not be scanned repeatedly using slightly altered sequence protocols. Abdominal scans were acquired using the Siemens 18 channel body array flex coil combined with the 18 channel spine array coil. Adult brain scans were acquired using the 32 channel Siemens head coil.

Volunteer scans were conducted on the 3T Siemens Skyra MRI scanners at the Boston Children's Hospital (Boston, USA), the Athinoula A. Martinos Center (Boston, USA) and at the Groote Schuur Hospital (Cape Town, South Africa). Scan protocols were first approved by the Boston Children's Hospital Institutional Review Board, the Partners Healthcare Ethics Committee and the University of Cape Town Human Research Ethics Committee, respectively. The nature of the experiment was fully explained to each volunteer, before obtaining written informed consent from them.

Flip angle optimization

Since the flip angle is directly linked to image contrast and signal intensity, it was important to optimize this parameter first. The flip angle that optimizes SNR can be calculated theoretically for each tissue type based on its T1 value and the TR of the sequence. Since the fetal brain is the region of interest in this work, the optimal flip angle α was calculated using the Ernst angle equation (eqn. 3.2) for a spoiled GRE sequence, given by

$$\alpha_E = \arccos\left(e^{-\frac{TR}{T_1}}\right) = \arccos\left(e^{-\frac{5.8}{2617}}\right) = 3.8°,$$

where *TR = 5.8 ms* and T1 for the fetal brain is estimated to be *2617 ms* [67]. To our knowledge, T1 values are not known for fetal grey and white matter separately and the value used here is an estimate based on results from preliminary research and is an average for both grey and white matter combined.

To achieve enough contrast for the purposes of motion tracking, we wanted to optimize the difference in signal between the fetal brain and the surrounding amniotic fluid. Figure 3.14 shows normalised signal intensity curves (eqn. 3.1) for various tissues that would appear in the large FOV required during an abdominal scan of a pregnant patient. Although the maximum signal for the fetal brain occurs at around 4°, contrast between amniotic fluid and the fetal brain will be maximal at a slightly higher flip angle of around 7°.

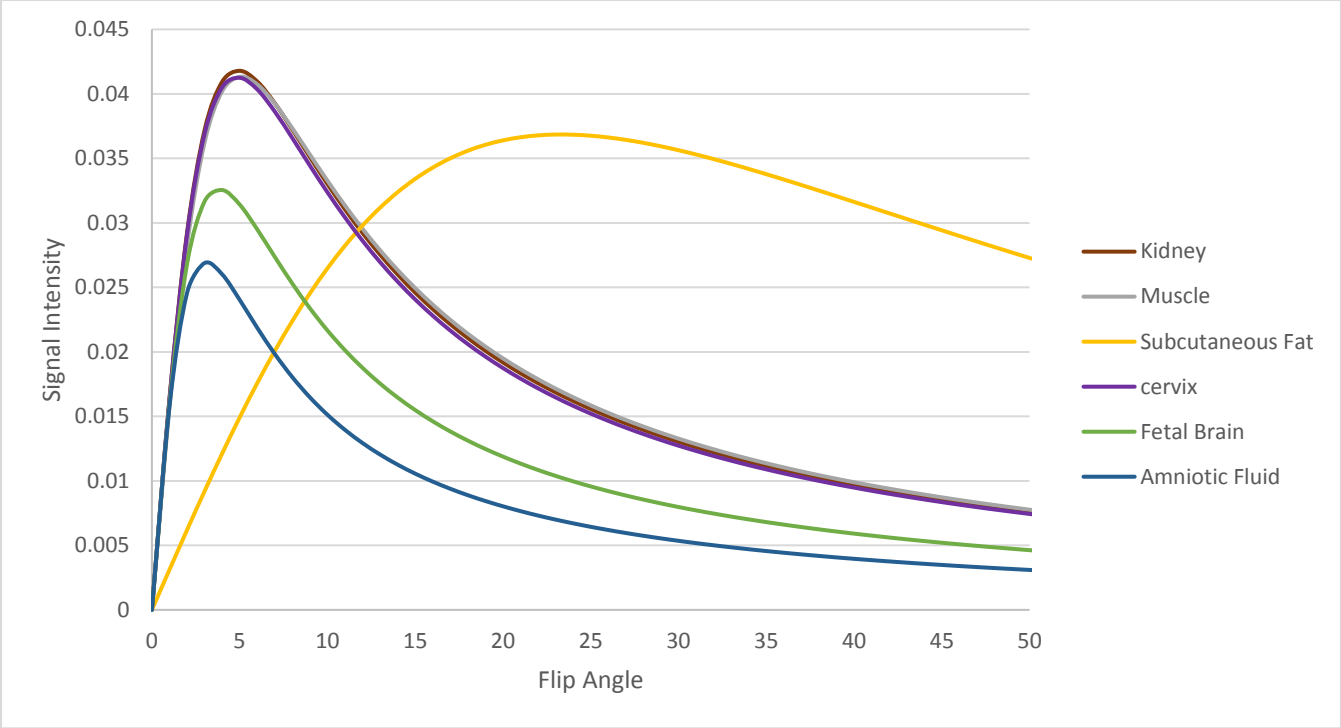

Figure 3.14. Graph to show the variation in signal intensities as a function of flip angle for various tissues in the abdominal region [68]. Scan TE/TR = 2.18/5.8 ms.

Many "real-life" factors, however, affect image contrast and cannot be accounted for using theoretical calculations. Therefore it was necessary to evaluate the reliability of these curves through a series of *in vivo* abdominal scans. Eleven acquisitions were performed in a healthy volunteer with the same protocol but varying flip angles. The 18 channel body array flex coil and 18 channel spine array coil were used to acquire abdominal scans on the 3T Siemens Skyra at Groote Schuur Hospital. The protocol was: 300 mm FOV, matrix size 128x128x128, TE/TR=2.18/5.8 ms, 1002 Hz/px, and TA=47 s. The volume was sampled by a single spiral consisting of 8192 projections. The flip angles were set to 2, 4, 6, 8, 10, 12, 14, 16, 18, 20 and 25 degrees, respectively. No gating or breath hold was implemented.

The data was reconstructed into a series of 3D volumes which were equivalent except for the scanning flip angle at which they were acquired. Tissues that were plotted in Fig. 3.14 were identified within each volume. The tissues which could most easily be identified were the kidney, muscle and subcutaneous fat. The images were imported into Matlab where a spherical region of interest (ROI) was identified in each of the three tissues. The mean signal intensity in each ROI was extracted and plotted as a function of the flip angle. The theoretically determined signal intensity curve for each of these tissues was plotted on the same set of axes to determine how well the predicted values corresponded to the actual measured signal.

Bandwidth and saturation

During the initial *in vivo* abdominal experiments, differences were observed between the artifacts present in images from different participants, even though the scan protocols were equivalent. These artifacts appeared at the abdomen-air interface and were dominant in instances where the participant had a thick layer of subcutaneous fat.

Experiments were performed to assess the appearance of these artifacts, specifically in the presence of fat, to confirm that the signal from fat was the source of the artifacts. For this purpose, the abdomens of two volunteers were scanned, one lean and the other with a thicker layer of subcutaneous fat. The 3D radial sequence was run with a single spiral consisting of 4096 spokes. Other scan parameters were 400 mm FOV, matrix size 128x128x128, TE/TR = 1.46/4.23 ms, 1502 Hz/px, flip angle 4^o and TA = 17 s. Scans were conducted at the Groote Schuur Hospital on the 3T Siemens Skyra with the 18 channel body array flex and 18 channel spine array coils.

Further experiments were performed to assess the effects of receiver bandwidth (BW) and water excitation (WE) on the artifact. The water excitation technique uses a combination of specifically-timed RF pulses that selectively excite water protons only and not fat protons. To this end, abdominal scans were conducted on the same two healthy volunteers using the same scan protocol described above, but with varying bandwidths, specifically 200 Hz/px (low), 500 Hz/px, 1000 Hz/px and 1500 Hz/px (high). For each receiver bandwidth, the acquisition was performed once with, and once without, water excitation selected. In total, eight acquisitions were performed in each volunteer. The images were compared visually to assess the presence of artifacts with each BW/WE combination.

We also examined the effect of WE selection on the scan TR since the addition of WE pulses lengthened the scan time significantly. Therefore, the TR of each scan was recorded and plotted as a function of receiver bandwidth both with and without WE.

Determining optimum values for N and M

Determining the minimum possible number of spokes per sub-spiral (*N*) was an iterative process. The challenge was to minimize *N* so that sub-spirals could be acquired as quickly as possible and also so that more sub-spirals (*M)* could be acquired within a reasonable acquisition time. Recall that for a constant number of total projections (*TP*), *M* and *N* are inversely proportional.

$$Total\ Projections\ (TP) = M\ x\ N \tag{3.20}$$

For a constant number of *TP*, increasing *M* improves the temporal resolution of motion tracking since more sub-spirals are acquired during the scan, which provides more frequent updates on the position of the fetus. However, because *N* has been decreased accordingly, the SNR of navigator images is lowered, which compromises the accuracy of motion registration results. The challenge was to find the most practical values for *M* and *N* where sub-spirals were acquired as rapidly as possible (minimum *N* and maximum *M*) but where streaking artifacts did not threaten to interfere with the motion registration process.

To examine how decreasing *N* affects the image quality of the sub-spirals, 3D radial acquisitions were repeated for varying values of *M* and *N*, keeping the total number of projections constant. Scans were conducted on the 3T Siemens Skyra at Groote Schuur Hospital. The procedure was first conducted on a Siemens water phantom, scanned with a 32 channel Siemens head coil. The scan protocol for phantom scanning was: 300 mm FOV, matrix size 128x128x128, TE/TR =1.65/4.91 ms, 1002 Hz/px, flip angle 8^o. First, a single spiral (*M*=1) of 8192 spokes (*N*=8192) was acquired. In subsequent acquisitions, *N* was decreased to 4096, 2048, 1024, 512 and 256, and *M* increased to 2, 4, 8, 16 and 32, respectively.

The same procedure was repeated *in vivo* to determine the smallest possible number of projections per sub-spiral for both an adult brain scan and also for an abdominal scan. For the brain, the same

protocol was used as for the phantom scans. For the abdomen, the scan protocol was: 300 mm FOV, matrix size 128x128x128, TE/TR 2.18/5.80 ms, 1002 Hz/px, flip angle 8^{o} and with water excitation selected to determine a conservative value.

For abdominal scans, sub-spiral acquisition time was plotted as a function of *M* to illustrate the time it took to acquire a single sub-spiral in each of the scans. Additionally, a graph was plotted to illustrate the effect of decreasing *N* on the signal-to-noise ratio of navigator images. Using a method similar to that described in the flip angle optimization section, the mean signal intensity for an ROI containing muscle tissue was divided by the mean noise in a background region to obtain an estimate for the SNR of each image.

3.3. Comparison between the 3D Radial and 3D Cartesian FLASH Sequences

Effect of Breathing

When imaging the abdominal region, it is necessary to assess the effects of breathing motion on the output images. For shorter scans, the participant could be asked to hold their breath to reduce the appearance of motion artifacts in the final image. However, in a clinical setting, and especially when imaging a pregnant patient, this is not practical. Therefore, to ensure that the experience is as comfortable as possible, the patient should be allowed to breathe freely throughout the scan. This requires an extremely motion-robust sequence for scanning. A radial scanning technique could provide a solution due to its inherent motion insensitivity.

An experiment was conducted to determine the effect and severity of motion artifacts from breathing on the images produced with the 3D radial sequence. Two healthy volunteer abdomens were scanned with the 3D radial sequence. Two radial acquisitions were performed, each with a single spiral consisting of $N = 4096$ projections. For the first acquisition, each subject was asked to hold their breath while in the next acquisition the subjects were asked to breathe normally. The above procedure was repeated with an equivalent 3D Cartesian FLASH sequence. Again, the subjects were asked to hold their breath for the first acquisition and to breathe freely throughout the second. In order to make the radial and Cartesian acquisitions equivalent, it was important to set the bandwidth and total readouts to the same values. Additionally, the TR and TE values were made to be as similar as possible. The total acquisition time was almost equivalent for each scan. In both the Cartesian and radial sequences, the flip angle was chosen to maximise the signal from all tissues, including fat, which enabled a fair comparison between these two sequences. The protocols of the 3D radial and FLASH sequences are presented in Table 3.1.

Table 3.1. The protocols for 3D Cartesian FLASH and 3D radial acquisitions used to evaluate the effect of breathing motion

	3D Cartesian FLASH	**3D radial**
FOV (mm)	400	400
Total scan time (s)	21	20
TE/TR (ms)	1.3/4.2	1.46/4.23
Flip angle (degrees)	25	4
Base resolution	64	128
Pixel size (mm)	6.25	3.125
BW	1002 Hz/px	1002 Hz/px
measurements	64 slices 4096 total readouts	Single spiral of $N = 4096$ projections

Effect of Rigid Body Motion

Other important types of motion to evaluate were rotations and translations since these present a challenge during fetal imaging. These may also arise if the mother breathes heavily, coughs or sneezes during the scan.

In order to illustrate this, a water phantom was scanned with a 3D Cartesian FLASH sequence with equivalent scan parameters to the 3D radial sequence. The 3D Cartesian FLASH was first set up with the desired resolution; base resolution (BR) = 128 and slices = 128, resulting in 2x2x2 mm voxel size. The "elliptical scanning" mode was selected to sample a circular disk in each of the Cartesian 2D slices to reduce the Cartesian scan time and prevent sampling the corners of the cubical field of view (FOV), since these points wouldn't contribute towards the radial sequence comparison anyway. The effective sampling area was therefore reduced by:

$$Sampling\ fraction = \frac{Area\ of\ Circle}{Area\ of\ Square} = \frac{\pi(BR/2)^2}{(BR)^2} = \frac{\pi(64)^2}{(128)^2} \approx 0.79$$

Therefore, the equivalent number of Cartesian readouts was 0.79 x 128 x 128 ≈ 12 943. The 3D radial acquisition was therefore set up with a number of spokes similar to the effective number of Cartesian readouts so that the resolution and total scan time for each acquisition would be similar. This meant that the radial sequence should ideally have $12\,943$ projections in total. The number of diametric spokes was, however, set to $13\,312$ to be divisible by 1024 so that the sub-spirals would fit neatly into the total projections. The final scan protocols are summarised in Table 3.2.

Table 3.2. The protocols for 3D Cartesian FLASH and 3D radial sequences used to evaluate the effects of translation.

	3D Cartesian FLASH	**3D radial**
FOV (mm)	256	256
Total scan time (s)	1 min 16	1 min 10
TE/TR (ms)	1.84/5.8	1.77/5.3
Flip angle (degrees)	11	11
Base resolution	128	128
BW	1002 Hz/px	1002 Hz/px
Other measurements	Slices = 128 Effective total readouts = 12 943 Elliptical scanning 8 mm^3 voxel size	13 spirals of *N* = 1024 spokes Total readouts = 13312 8 mm^3 voxel size

Water phantom and brain scans were performed using a 32 channel Siemens head coil on the 3T Siemens Skyra MRI at the Athinoula Martinos Center in Boston to compare the effects of rigid body motion in Cartesian and radial acquisitions. The phantom was placed on a rig which allowed it to be rotated by a fixed angle, and then back to its original position. During each acquisition the phantom was manually moved for a period of 2 seconds at 38 seconds into the scan, ending again at its original position. Acquisitions were repeated using the 3D Cartesian FLASH and radial sequences.

This procedure was then repeated for an adult brain first with no motion and then where the volunteer was asked to tilt their head down and back to its original position at 38 seconds into the scan, over the course of approximately 4s, which is the time it takes to acquire 1 sub-spiral with 1024 spokes. Images from the 3D radial and 3D Cartesian FLASH acquisitions were compared to evaluate the appearance of motion-induced artifacts in each sequence. For radial acquisitions, the sub-spiral data were combined in k-space prior to image reconstruction.

Since one or two corrupted sub-spirals may minimally affect a radial acquisition if the subject returns to their original position, we were interested to see the effect when the subject does not return to their original position, which would mean that the head is in a different position for all the sub-spirals acquired after the motion event. To this end, the 3D radial acquisition was repeated where the volunteer was asked to nod their head downwards halfway through the acquisition and remain in their new position. Images were reconstructed for the combined data from all the sub-spirals, as well as for each individual sub-spiral. Individual sub-spiral images were co-registered to the first sub-spiral image using FLIRT in FSL [69]. The 3D affine transformations from successive co-registrations were used to plot the motion curves in Matlab.

3.4. Reconstruction of Navigator Images

Customization of Reconstruction code

The 3D radial sequence developed in this project was designed with a new trajectory to facilitate acquisition of sub-volumes of data that could be reconstructed as navigator images to track the motion of the fetus during an acquisition. Since the standard Siemens 3D radial sequence acquires only a single volume of data, the Siemens product reconstruction code needed to be adapted for data from a segmented scan. A method previously developed by Andre van der Kouwe and Himanshu Bhat (2012, [70]) to separate individual sub-sets of data acquired with a segmented scan was modified for the purposes of this project.

Firstly, the code was adapted to receive incoming radial data from the new trajectory chosen for the sequence. This involved re-writing the equations in the Siemens "`trajectory.cpp`" source file. The trajectory calculation script is called by the "`Compute Scan`" function during the reconstruction process.

Next, the code was altered to receive as input in the reconstruction of each sub-spiral a text file specifying the starting spoke number and the number of diametric spokes to be included in the reconstruction of the sub-spiral, as well as a 4x4 transformation matrix. For initial reconstruction of navigator images, the transformation matrix is the identity matrix. Once navigator images have been co-registered to the first navigator image, the transformation matrix output from this co-registration is inserted into the text file. As explained later, these transformation matrices can be used to generate co-registered sub-spiral images. Due to the segmented nature of the data, a series of text files are required. The format of the text files are shown in Table 3.3 for a total volume consisting of N=1024 spokes and M=2 sub-spirals.

Table 3.3. Example of the text files required during image reconstruction for two sub-spirals. The text files specify the starting spoke of each sub-spiral, the number of spokes per sub-spiral, and the transformation matrix from co-registration to the first sub-spiral. The identity matrix is used for initial reconstruction of navigator images before co-registration.

General format	(Index of first sample) (No. of samples to be included) [4x4 transformation matrix]
Spiral_1.txt:	0 512 1 0 0 0 0 1 0 0 0 0 1 0 0 0 0 1
Spiral_2.txt:	512 512 1 0 0 0 0 1 0 0 0 0 1 0 0 0 0 1

In this way, individual sub-spirals that are suitable for self-navigation applications are reconstructed. Once all sub-spiral images have been reconstructed, they can be combined into a single volume using the FSL [71] command "`fslmaths -add`".

Due to restrictions on modifications to the standard Siemens image reconstruction code, reconstruction could only be performed offline. Normally, when a scan is performed, reconstruction occurs rapidly on the scanner using the installed Siemens ICE (Image Calculation Environment) product files. Since the reconstruction method presented here was customized, it was not possible to install the files on the scanner. As a result, this sequence will not be able to perform "real-time" navigation, but recommendations will be made for future development.

Tests to Demonstrate the Potential of a Segmented Scan for Self-navigation Applications

The combination of sub-spirals was demonstrated for a phantom scan acquired using a 32 channel Siemens head coil on the 3T Skyra at Groote Schuur Hospital. Scan parameters were: 300 mm FOV, matrix size 128x128x128, TE/TR 1.65/4.91 ms, 1002 Hz/px, flip angle 8^{o}. Four sub-spirals with $N = 1024$ spokes were acquired. Images were first reconstructed for the individual sub-spirals and then sub-spiral images were combined in image-space to generate a single volume. The average SNR of the sub-spiral images was compared to the SNR for the combined image, extracted using Matlab.

The acquisitions described previously in section 3.3 where the participant was asked to rotate their head downwards to a new position halfway through the acquisition, were used here to illustrate the benefits of a segmented scan. The protocol is given again for convenience: 256 mm FOV, 11^{0} flip angle, 128x128x128 matrix size, BW = 1002 Hz/px, TE/TR = 1.77/5.3 ms, scan time 1 min 05 seconds, total readouts = 13 312, 13 spirals of N=1024 spokes each.

The image was first reconstructed using data from all the sub-spirals combined to demonstrate the effect of including sub-spirals corrupted by motion on the final image. Then, each of the 13 subsets of data were individually reconstructed and co-registered using FLIRT in FSL [69] to the first sub-spiral, yielding 12 (in general, M-1) transformation matrices. The process is illustrated in Figure 3.15.

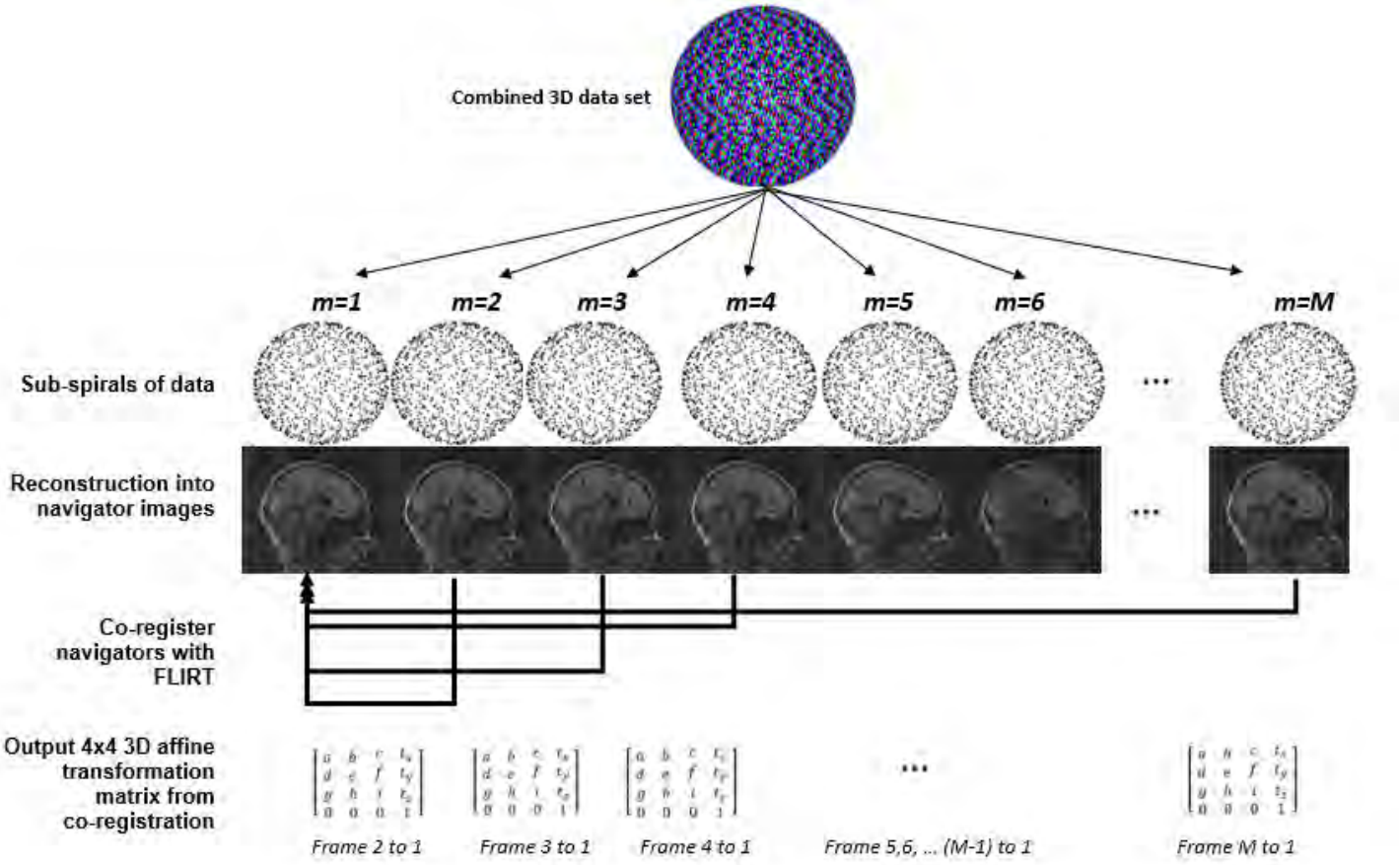

Figure 3.15. Schematic to illustrate reconstruction and co-registration of sub-spiral navigator images

Translation in each direction was computed from the transformation matrices and plotted to illustrate the type of motion that occurred and which sub-spiral was most severely affected. The most severely affected sub-spiral was excluded from subsequent image reconstructions. However, the head was still in a different position for sub-spirals acquired before and after the motion, so that sub-spirals cannot simply be combined after discarding the corrupted volume. Since there is no mechanism to co-register sub-spiral k-space data, sub-spirals preceding the corrupted acquisition were combined to reconstruct an image of the head from data acquired before the motion occurred, and the sub-spirals after to reconstruct an image based on data acquired after the motion. As such, each image was reconstructed from a reduced number of sub-spirals, and as such fewer diametric spokes, limiting the achievable SNR.

We were interested in examining whether combining sub-spiral images in image space, after applying co-registration, would improve image quality, as all except severely corrupted sub-spirals could then be used in the reconstruction of the final image. To this end, the 4x4 3D affine transformation matrices generated from the co-registration of individual sub-spiral images to the first sub-spiral image, were entered into the text files used during sub-spiral image reconstruction. This allows motion correction to be performed directly to each sub-spiral image immediately following reconstruction, yielding a set of co-registered sub-spiral images. The resulting co-registered sub-spiral images were then combined to obtain a final image. Severely motion-corrupted sub-spirals were excluded from the final volume. This process is illustrated in Figure 3.16.

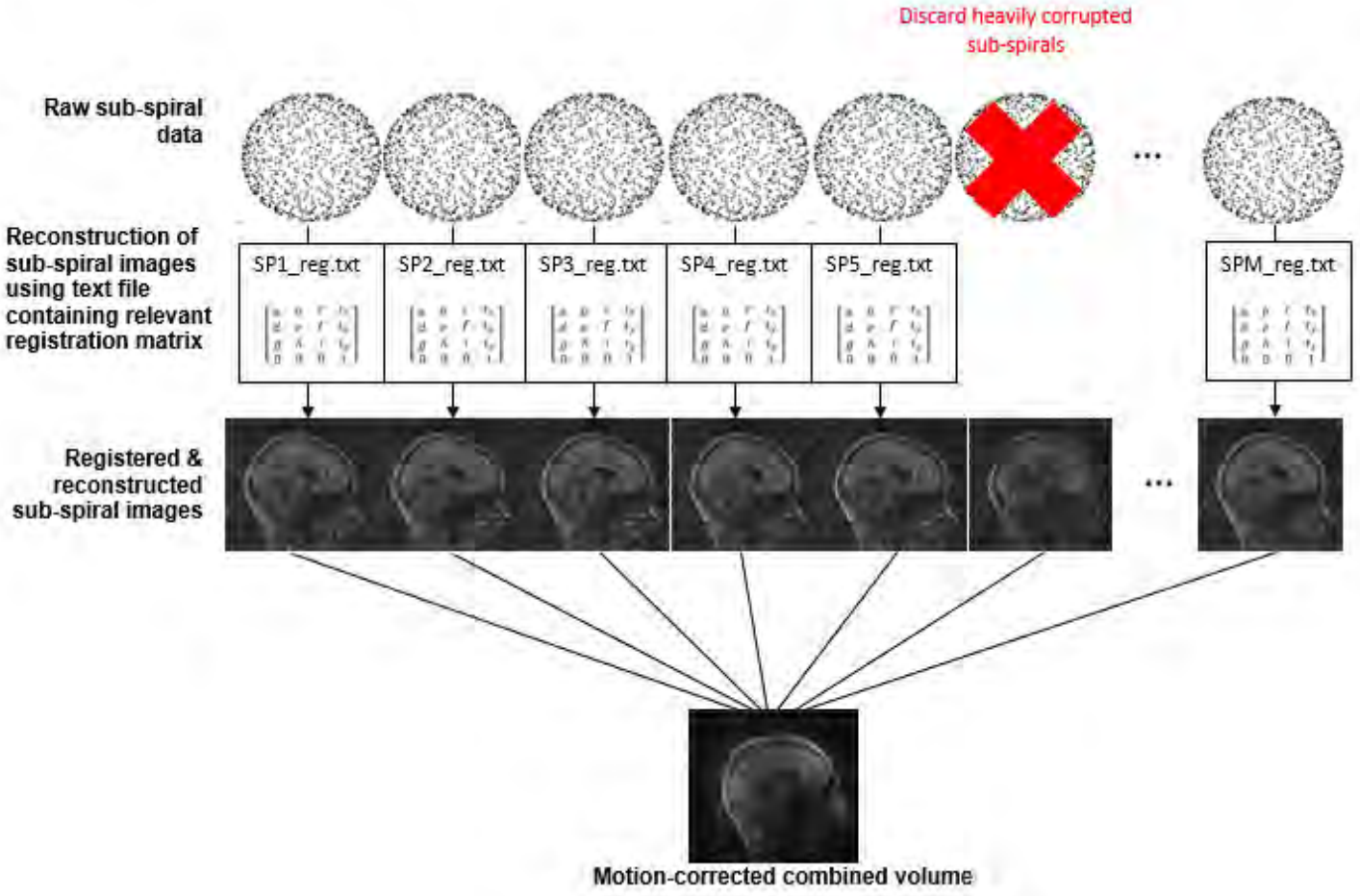

Figure 3.16. Schematic to show how the registration matrices can be used to perform motion correction directly during sub-spiral image reconstruction to generate a set of co-registered sub-spiral images. The sub-spiral images are then combined into a single motion-free volume.

Reconstructing with a Smaller Base Resolution

One of the benefits of offline reconstruction is the freedom to manipulate scan parameters post scan. Streaking artifacts are characteristic to radial sampling and the navigator images produced in this work were heavily affected by them. The artifacts appear due to the severely under-sampled edges of the k-space field of view (FOV). During protocol development, we determined the fewest number of spokes for which the streaking artifacts did not corrupt the navigator images. But, even with the minimum number of spokes possible, the acquisition of navigator images took too long to provide temporally accurate information on the motion of the fetus. Additionally, even at a minimum acquisition time of 2.6 seconds per sub-spiral when imaging the adult brain, streaking artifacts threatened to obstruct the motion registration process.

The challenge was to shorten the acquisition time for each sub-spiral, without compromising the image quality any further. Since the protocol parameters had already been optimized, the influence of parameters that can be manipulated during image reconstruction was investigated.

In MRI, the matrix size is the number of pixels that constitute the k-space Field of View (FOV) in the *X, Y,* and *Z* dimensions,

$$Matrix\ Size\ = \frac{Field\ of\ View}{Pixel\ Size}. \tag{3.21}$$

In 3D imaging, where the base resolution (BR) is defined as the number of points sampled during a single readout, the matrix size can also be given by

$$Matrix\ Size = BR(x) * BR(y) * BR(z). \tag{3.22}$$

The matrix size and base resolution are chosen to optimize the spatial resolution of the final image and are specified by the user in the scan protocol. Reconstructing at the scanned base resolution will reconstruct the image over the entire k-space FOV. To reduce the severe streaking artifacts arising from undersampled data at high spatial frequencies in sub-spiral images with limited numbers of spokes, a method was implemented that allows the user to specify a reduced base resolution to be used during sub-spiral image reconstruction. Therefore, the user is able to reconstruct the image using only data from the densely sampled central region of k-space. If this method reduces the artifacts within the navigator images, sub-spirals could be sampled using fewer spokes, reducing the time required for acquisition of navigator images.

A phantom was scanned using a 32 channel Siemens head coil with a total of 8192 diametric spokes and a minimum *N* of 512 (section 3.2) spokes per sub-spiral. Other scan parameters were: 300 mm FOV, matrix size 128x128x128, TE/TR 1.65/4.9 ms, 1002 Hz/px, flip angle 8^{o}. The sub-spirals were reconstructed at base resolutions of 128 and 64, respectively, to evaluate the effect of BR on the appearance of streaking artifacts in the navigator images.

An adult brain was scanned twice using the same protocol and head coil as for the phantom scan above. The volunteer was asked to shift their head to a new position halfway through the scan and remain there. In the first acquisition, *M*=24 sub-spirals each consisting of *N*=512 spokes were acquired. The acquisition was then repeated with *N* reduced to 256 and *M* increased to 48 sub-spirals.

A single sub-spiral from each scan was reconstructed at base resolutions of 128 (the scanned resolution), 96 and 64, to illustrate the effect on the image quality of reconstructing at a reduced base resolution.

The 24 sub-spirals, each with *N* = 512 spokes, from the first scan were reconstructed at the scanned base resolution of 128 and co-registered to the first sub-spiral to produce a plot of the motion that occurred during the scan. All sub-spiral images, except those corrupted by motion, were then reconstructed again with their transformation matrices applied directly during image reconstruction and combined to generate a final volume. This image was compared to that obtained when all sub-spiral k-space data are combined prior to image reconstruction.

To determine whether navigator images acquired with fewer than *N*=512 spokes could be reconstructed at a reduced base resolution to improve the accuracy and temporal resolution of their co-registration results, the 48 sub-spirals acquired with *N*=256 spokes each during the second scan were reconstructed at a base resolution of 64. Each navigator image was co-registered to the first sub-

spiral to produce transformation matrices. Each sub-spiral was then reconstructed once more, but this time at the scanned base resolution of 128 with the relevant transformation matrix included during image reconstruction. Co-registered sub-spiral images were combined into a single volume. This process is illustrated in Figure 3.17.

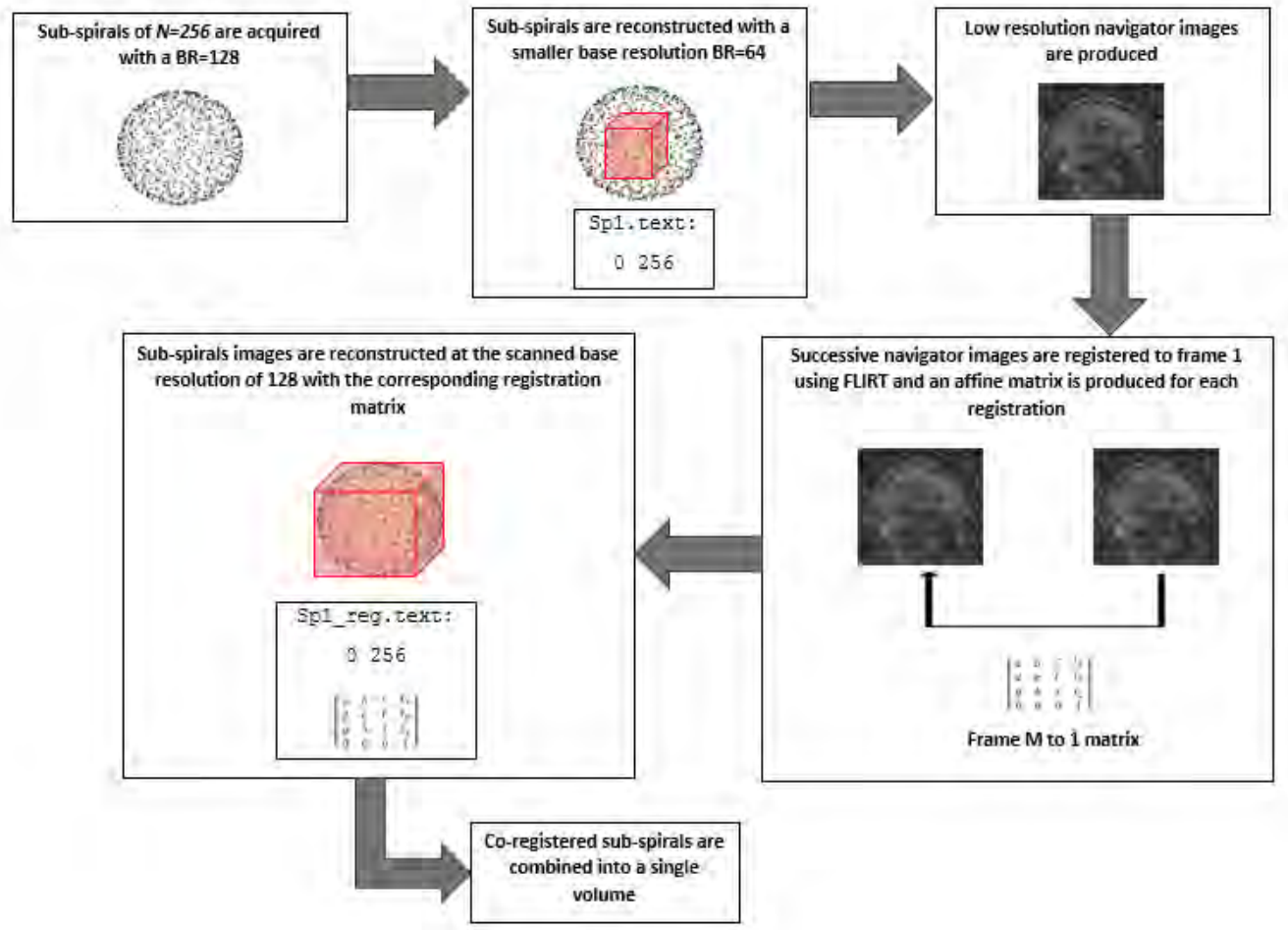

Figure 3.17. Flow diagram to illustrate how navigator images can be reconstructed at a reduced base resolution to improve co-registration accuracy. Reconstruction including motion correction is then repeated at the original base resolution to obtain co-registered navigator images that can be combined to obtain a final image.

3.5. *In vivo* Fetal Scans with the Optimized Protocol

Fetal scans were acquired in two pregnant mothers – one before protocol optimization and the other after. In each case the sequence developed here was added to the end of the imaging protocol with the consent of the mother. Both scans were performed on 3T Siemens Skyra MRI scanners using the Siemens 18 channel body array flex and 18 channel spine array coils. In the first case, a healthy volunteer (subject A) pregnant with twins at 36 weeks gestation recruited as part of a different research study received scanning at the Boston Children's Hospital. In the second case, the protocol was added at the end of the imaging session for a mother (subject B) at around 33 weeks gestation who received fetal scanning at Groote Schuur Hospital for clinical reasons. The scan parameters for the two protocols are summarised in Table 3.4. For the second acquisition, scan parameters were selected based on tests performed in normal abdominal scans. As such, a higher flip angle of 7 degrees was chosen to optimize the contrast between the fetal brain and amniotic fluid and a higher BW of 1000 Hz/px to decrease the scan TR. In addition, WE was selected to reduce the appearance of artifacts and more sub-spirals comprising fewer spokes were acquired.

Table 3.4. Fetal protocols for scanning pregnant patients with the 3D radial FLASH sequence

	First Scan Subject A	**Second Scan Subject B**
FOV (mm)	400	400
Total scan time	1 min 35 seconds	1 min 15 seconds
TE/TR (ms)	2.33/5.8	2.39/6.56
Flip angle (degrees)	Ernst angle of 4	7
Base resolution	128	128
BW	399 Hz/px	1002 Hz/px
Other measurements	Total projections = 16384 8 spirals of *N* = 2048 Voxel size = 3mm^3	Water Excitation Selected Total projections = 12 288 12 spirals of *N* = 1024 Voxel size = 3mm^3

During the acquisition, the Normal Mode specific absorption rate (SAR) measured by the scanner was recorded. This value is calculated taking into account the RF energy deposition for a specific sequence and protocol as well as the patient-specific height and weight measurements to provide a value for the energy absorption in W/Kg as well as a percentage of the SAR limit. For fetal scans, a limit of 2W/Kg is imposed on the Siemens MRI machines [46].

Images reconstructed from sub-spiral data without and with co-registration were compared. First, images were reconstructed from sub-spiral data combined in k-space without any co-registration. To examine the potential of using sub-spiral data for motion tracking, individual sub-volumes were then reconstructed at a reduced base resolution of 64 and co-registered to the first navigator image. The masking tool in FSL [71] was used to select the fetal brain as the ROI to be co-registered. Sub-spiral image reconstruction was repeated at the scanned base resolution and the corresponding transformation matrices applied before combining the co-registered sub-spiral images in image-space to produce the final image for comparison with the first volume obtained by combining sub-spiral data in k-space.

4. Results

4.1. Sequence Development

Tests to Compare Sub-spiral Distributions

Streaking artifacts in the sub-spiral and final combined images were compared for the four different sampling schemes using data acquired in a phantom. The simplified end-point trajectories for each scheme were plotted in Matlab and are presented above the corresponding reconstructed images. Significant streaking artifacts are present in the interleaved sub-spiral (Fig. 4.1a), and in both the sub-spiral and combined image reconstructed from data acquired using overlapping sub-spirals (Fig. 4.2).

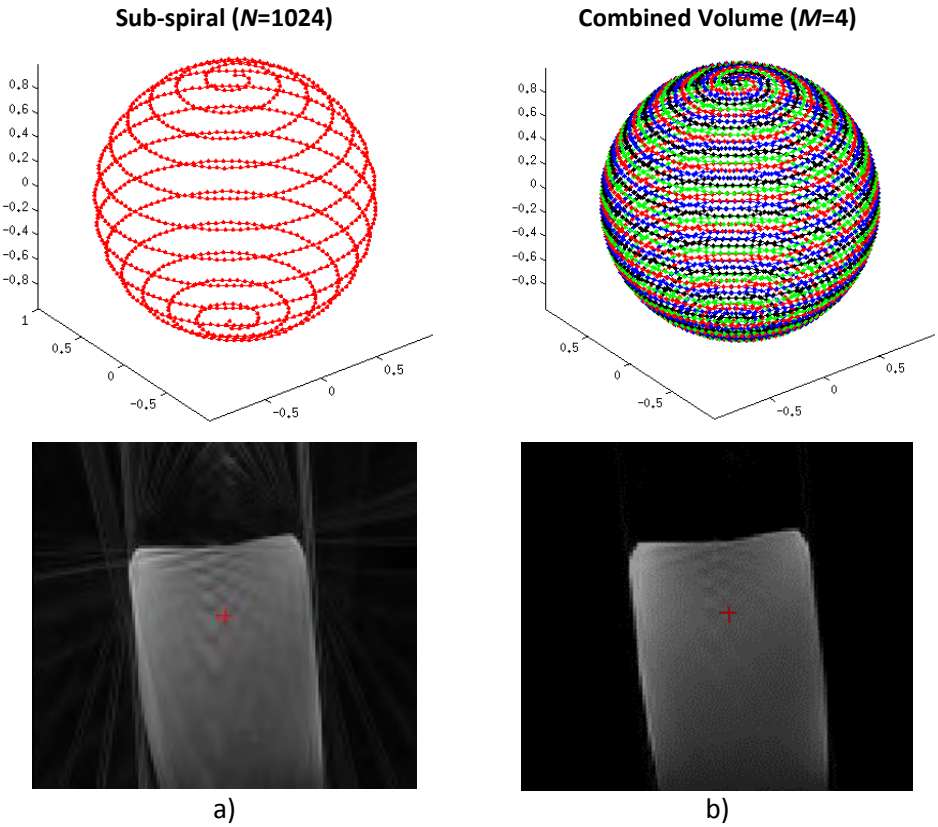

*Figure 4.1. (a) Phantom image reconstructed from one of four **interleaved sub-spirals** and (b) the final image reconstructed after combining all the sub-spirals. The distribution of end points on the surface of the sphere is shown above for a single sub-spiral (left) and for all the sub-spirals combined (right).*

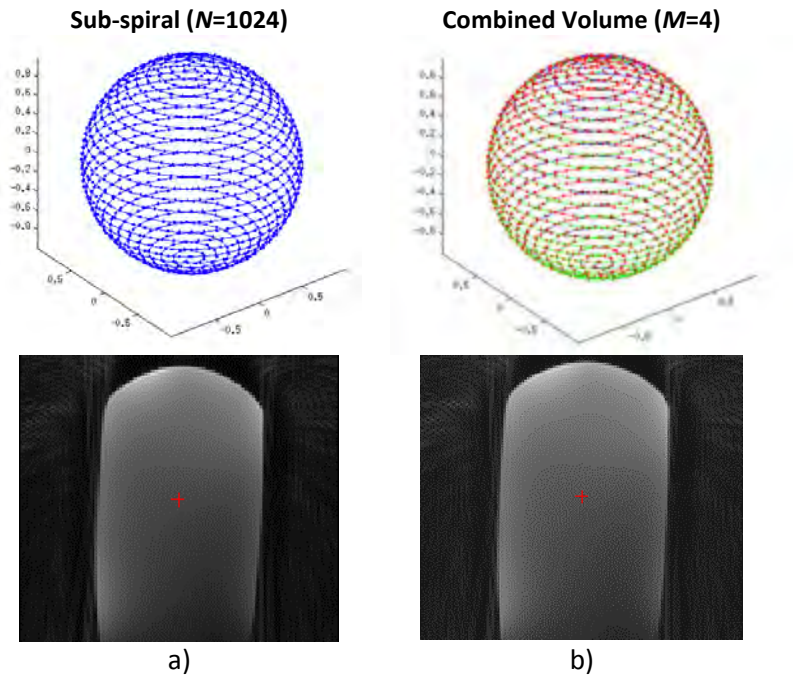

*Figure 4.2. (a) Phantom image reconstructed from one of four **overlapping sub-spirals** and (b) the image reconstructed from the combination of the sub-spirals. The distribution of end points on the surface of the sphere is shown above for a single sub-spiral (left) and for all the sub-spirals combined (right).*

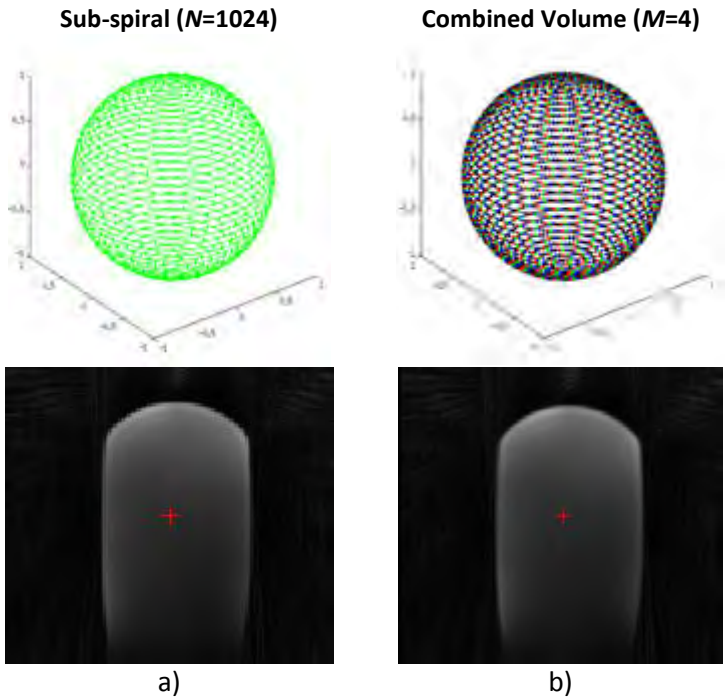

*Figure 4.3. (a) Phantom image reconstructed from one of four **rotated sub-spirals** and (b) the image reconstructed from the combination of all the sub-spirals. The distribution of end points on the surface of the sphere is shown above for a single sub-spiral (left) and for all the sub-spirals combined (right).*

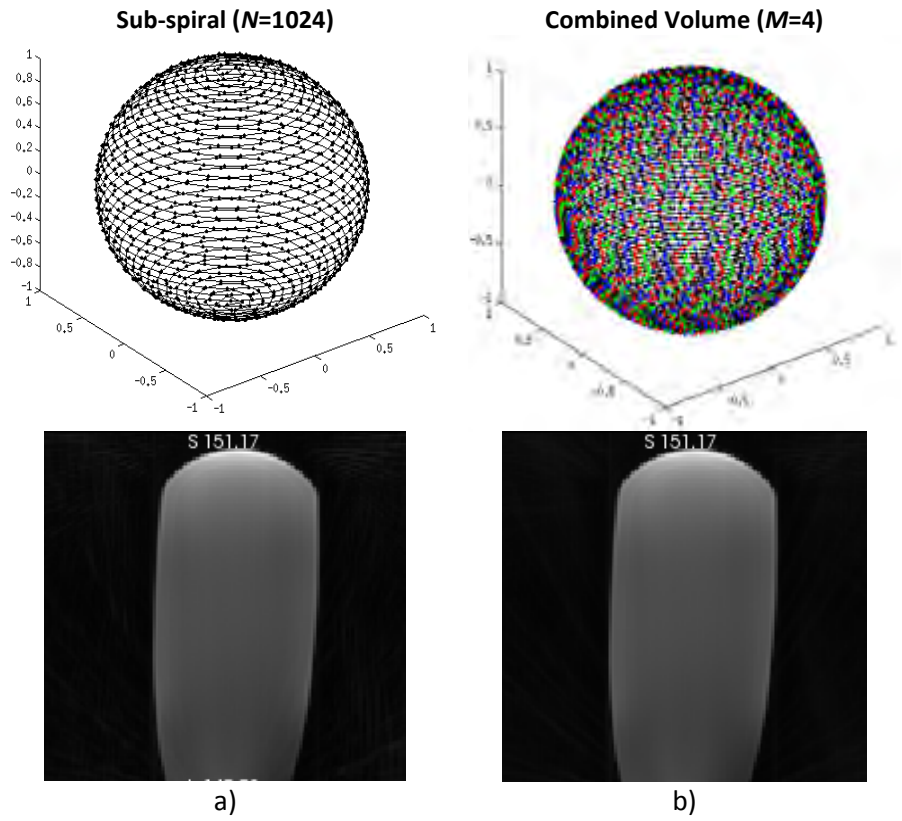

*Figure 4.4. (a) Phantom image reconstructed from one of four **indexed sub-spirals** and (b) the image reconstructed from the combination of all the sub-spirals. The distribution of end points on the surface of the sphere is shown above for a single sub-spiral (left) and for all the sub-spirals combined (right).*

Interleaved and indexed sub-spirals, when combined, yield the same distribution of end points on the surface of the sphere as a single spiral with the same total number of projections. This is illustrated by comparing, for each sampling scheme, the distributions of end points on a sphere when eight sub-spirals (*M*=8*, N*=512) are combined to the distribution for a single spiral with the same total number of projections (*M*=1, *N*=4096) (Fig 4.5).

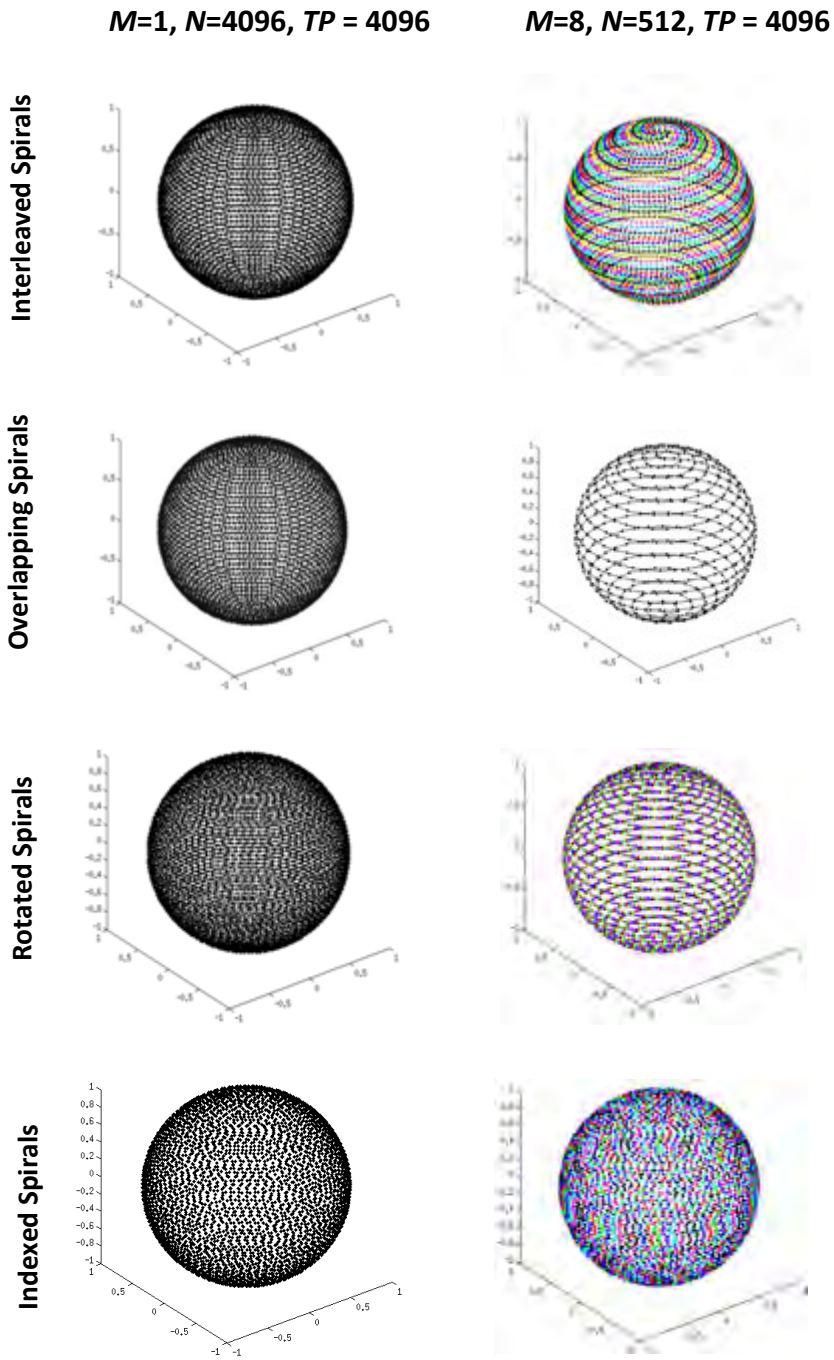

Figure 4.5. Distribution of end points on the surface of a sphere compared for a single spiral with 4096 total projections (left) and 8 sub-spirals, each comprising 512 diametric spokes for a total of 4096 projections (right), for each sampling scheme.

Finally, the effect of increasing M to 12 was compared in interleaved and indexed sub-spiral images for a fixed number (*TP* =12288) of diametric readouts (Figs. 4.6 and 4.7). Each sub-spiral comprises 1024 diametric spokes. Streaking artifacts were much more prominent in the sub-spiral reconstructed from data acquired using the interleaved sampling strategy (Fig. 4.6).

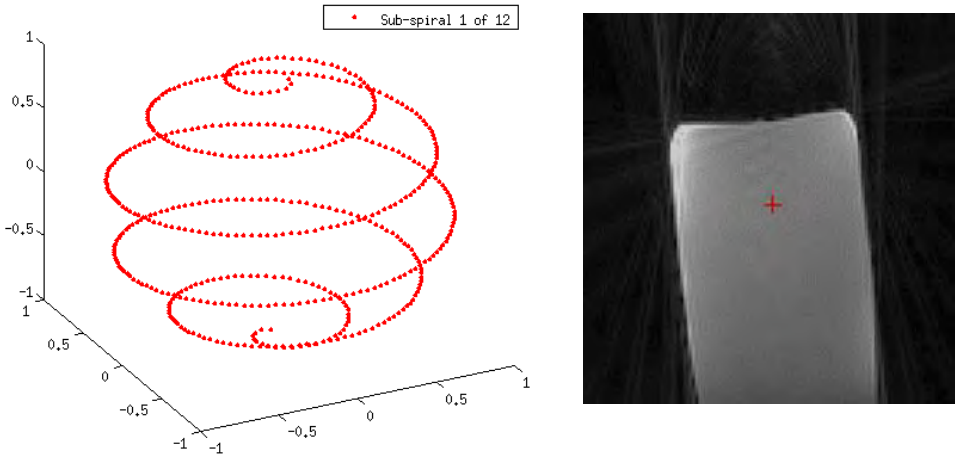

*Figure 4.6. (Left) simplified sampling distribution of end points of diametric spokes on the surface of the sphere for one of twelve sub-spirals for the **interleaved** sampling strategy. The reconstructed image on the right is for a single sub-spiral from this sampling strategy.*

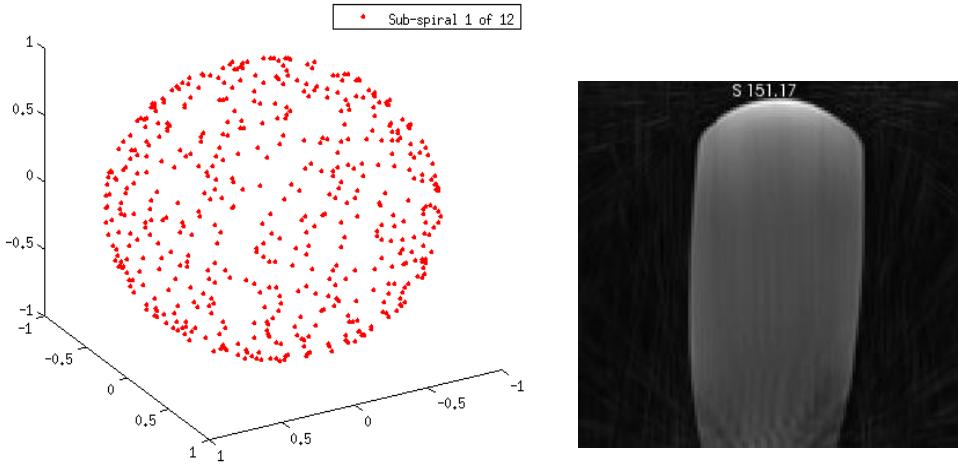

*Figure 4.7. (Left) simplified sampling distribution of end points of diametric spokes on the surface of the sphere for one of twelve sub-spirals for the **indexed** sampling strategy. The reconstructed image on the right is for a single sub-spiral from this sampling strategy.*

4.2. Protocol Development

Flip angle optimisation

Figure 4.8 shows abdominal images acquired with three different flip angles. The variations in signal intensity as a function of flip angle are compared in kidneys, muscle and subcutaneous fat in Figure 4.9. The measured values closely follow the theoretically-predicted curves.

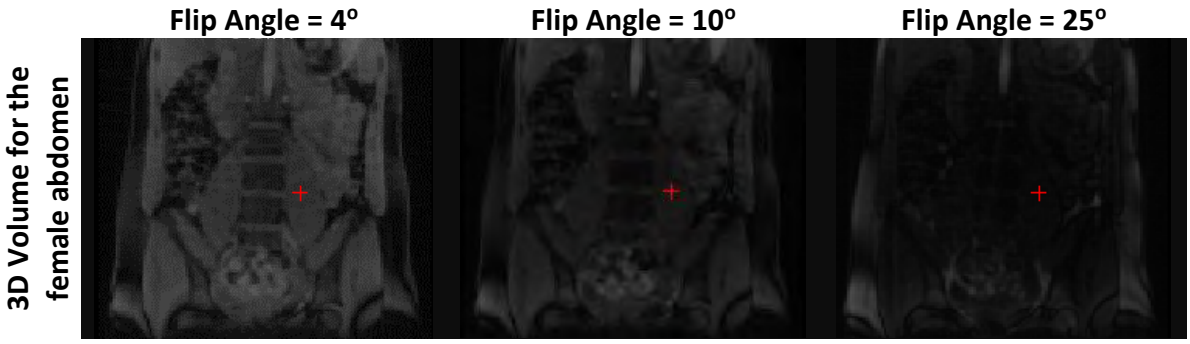

Figure 4.8. Series of images from an abdominal scan illustrating the variation in signal intensity for a particular region of interest for different flip angles.

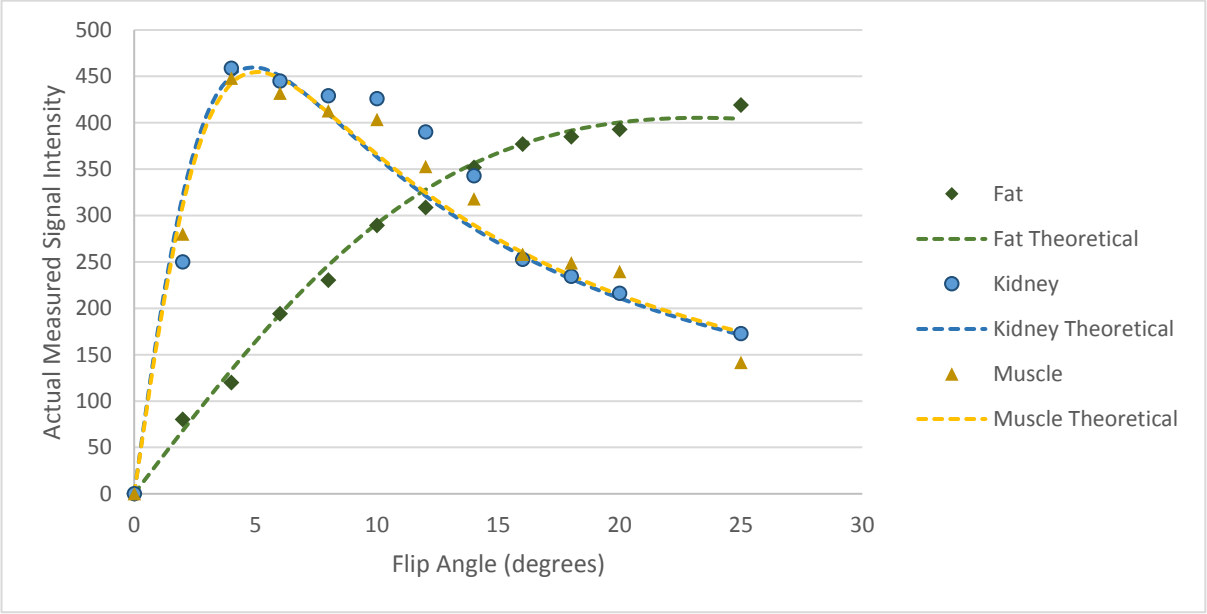

Figure 4.9. Comparison of measured and theoretical signal intensity as a function of flip angle in fat, kidney and muscle.

Bandwidth and saturation

Figure 4.10 demonstrates the increase of streaking artifacts in subjects with a thicker layer of subcutaneous fat compared to leaner subjects. Images acquired with different receiver bandwidths, both with and without water excitation (WE), are compared in Figure 4.11 for subjects with less and more subcutaneous fat. While the effect of WE is negligible in leaner subjects, there is a noticeable improvement in image quality and a reduction in the presence of streaking artifacts in images acquired with WE in subjects with a thicker layer of subcutaneous fat.

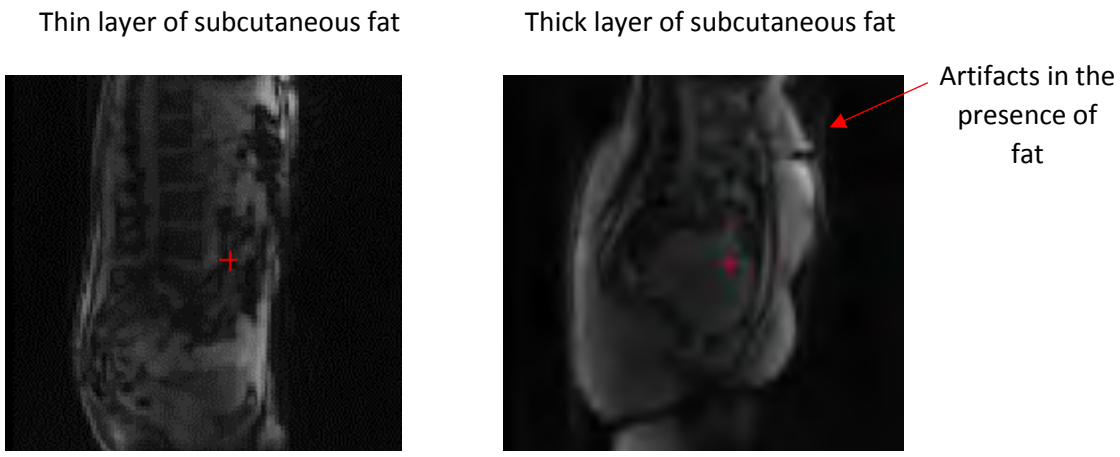

Figure 4.10. Images acquired with different receiver BWs, both with and without WE, in subjects with more (left) and less (right) subcutaneous fat.

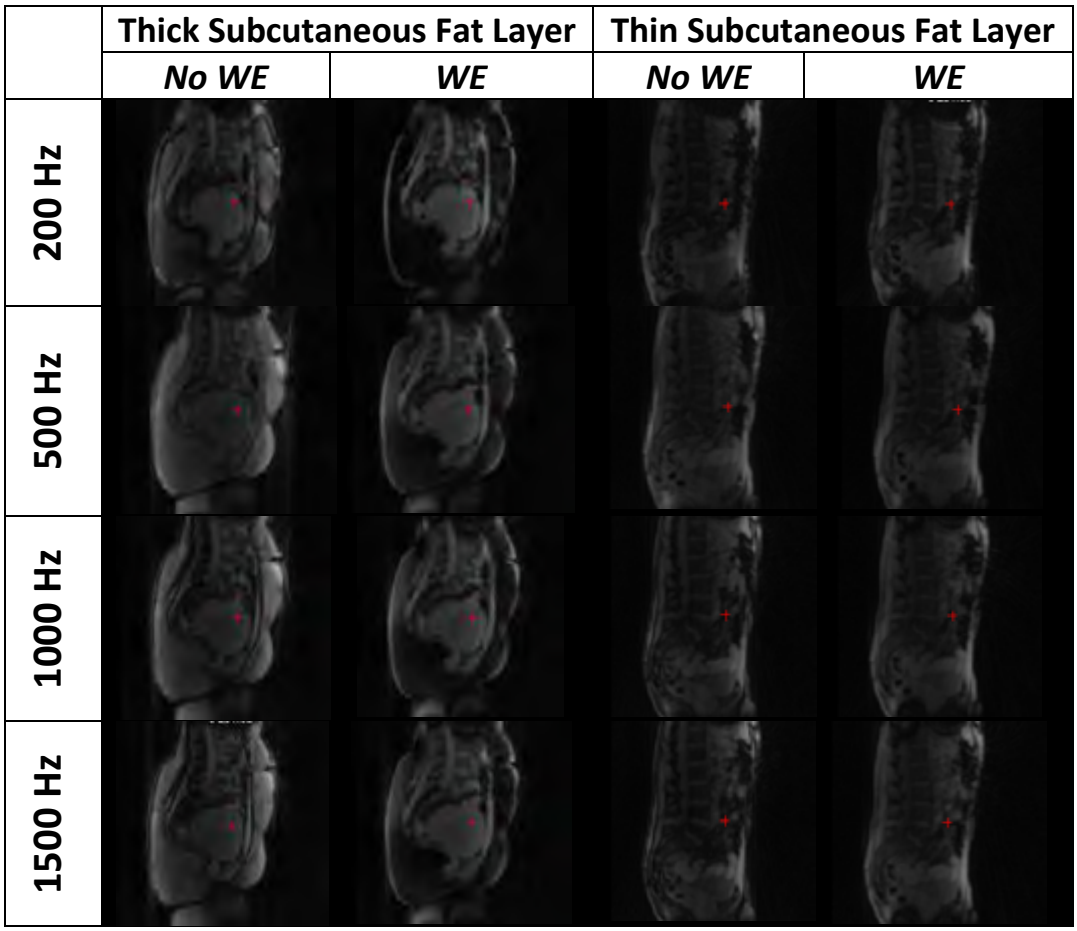

Figure 4.11. Scan images acquired with different receiver BWs, both with and without WE, in subjects with less and more subcutaneous fat.

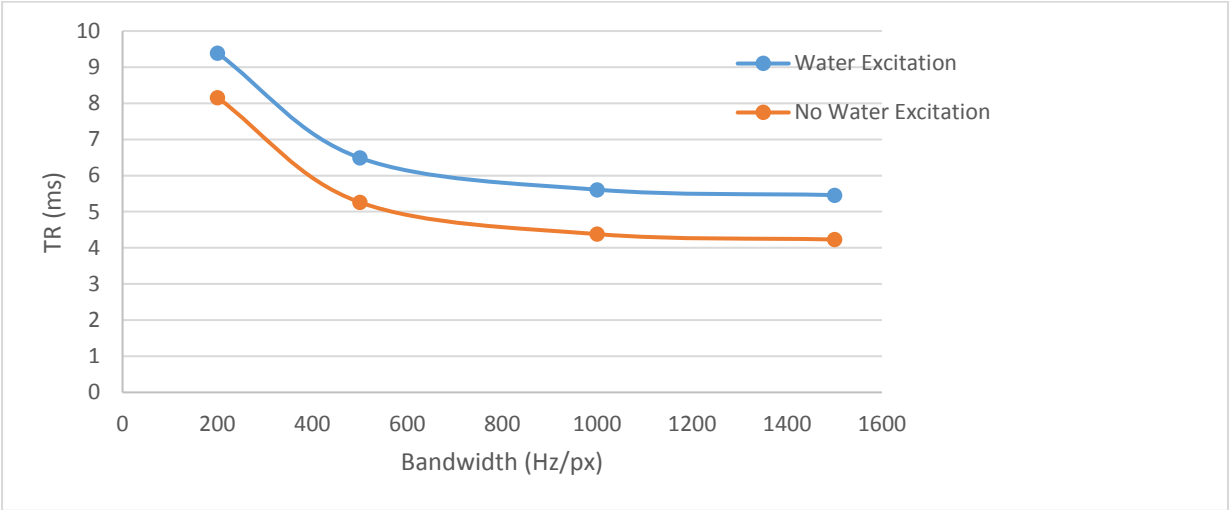

Figure 4.12. Graph to show the relationship between increasing bandwidth on the scan TR with and without water excitation selected.

Figure 4.12 illustrates the relationship between bandwidth and scan TR for instances where water excitation is and is not selected. From the graph in Figure 4.13, it is evident that the TR significantly decreases with increasing bandwidth, but then plateaus at about 1000Hz/px. This graph also shows how water excitation pulses increase the minimum TR and as such the scan time. This increase becomes significant when one considers the acquisition time of a spiral. For example, one spiral (N=4096) with no water excitation and a bandwidth of 1000 Hz/px could be acquired in 18 seconds. For the same bandwidth, applying water excitation increases the acquisition time to 23 seconds, which corresponds to a 28% increase in scan time.

Determining optimum values for N and M

The images in Figure 4.13 are for a single sub-spiral from a series of phantom scans acquired using the head coil where the total number of projections was kept constant while *M* and *N* were varied iteratively. The corresponding sub-spiral end-point trajectory plots are shown above each navigator image. Even with *N*=512 spokes per sub-spiral, the streaking artifacts appeared outside the phantom, suggesting that the images could provide useful information on the position of the phantom through co-registration. Sub-spirals of *N*=512 projections were acquired in 2.6 s.

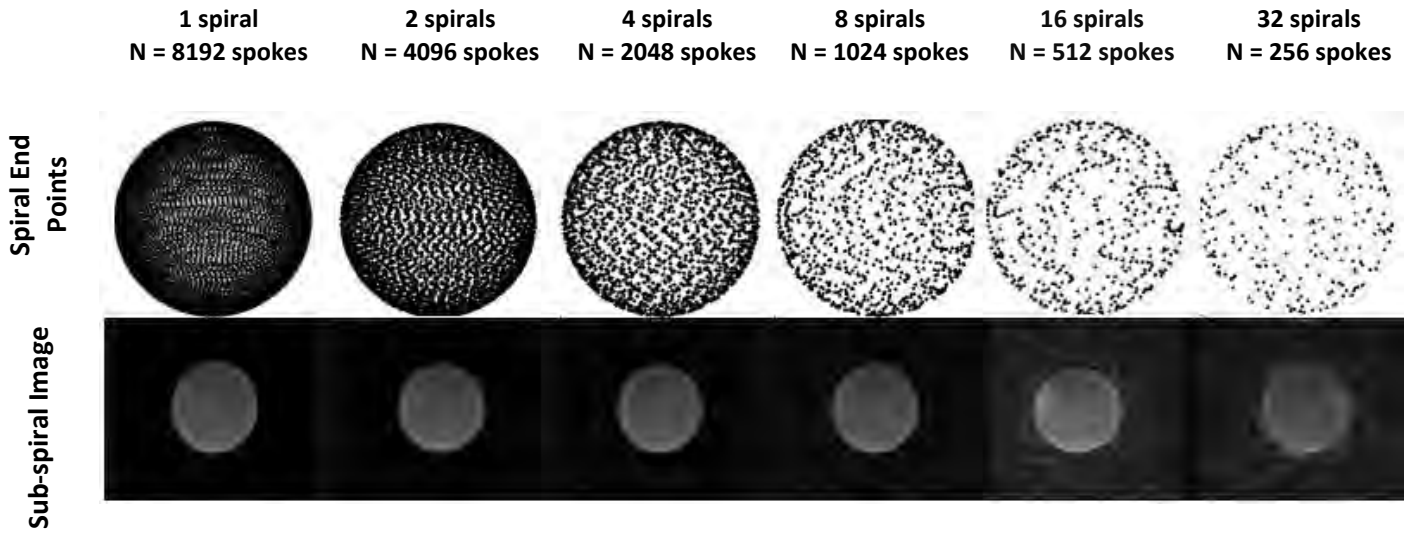

Figure 4.13. Series showing the effect of decreasing N on the appearance of streaking artifacts in sub-spiral images for a constant TP = 8192. The phantom was scanned using the 32 channel head coil using the following protocol: 300 mm FOV, matrix size 128x128x128, TE/TR 1.65/4.91 ms, 1002 Hz/px, flip angle 8°.

It is worth noting that even for a single sub-spiral of *N*=8192 projections, the volume is under-sampled towards the edges. According to eqn. 2.9, the number of diametric readouts (N_{diam}) required to achieve isotropic resolution for a base resolution (BR) of 128 is given by

$$N_{diam} = 2\pi(BR)^2 = 102\,944.$$

As such, even the image acquired with a single sub-spiral is under-sampled by a factor of about 12, and this factor increases proportionally for sub-spirals with fewer projections. An under-sampling factor, $F_{undersampled}$, can be defined as follows:

$$F_{undersampled} = \frac{N_{diam}}{N}.$$

The series of images in Figures 4.14 and 4.15 show the effect of decreasing *N* on sub-spiral image quality and the presence of streaking artifacts in the brain and abdomen, respectively. Based on these images, we decided that for a brain scan the minimum number of projections per sub-spiral that produced acceptable images is *N* = 512. These spokes can be acquired in 2.6 s (TR = 4.91 ms x 512 spokes). For these values, the brain sub-spiral volumes are under-sampled by a factor of 201.

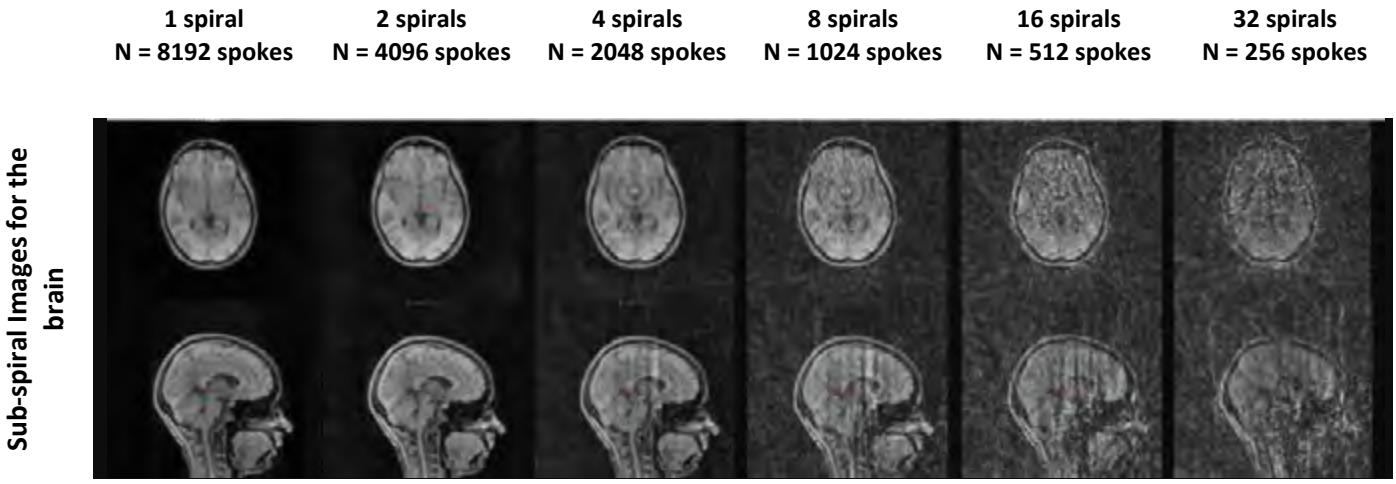

Figure 4.14. Axial (top) and sagittal (bottom) views of sub-spiral images of the brain acquired with decreasing numbers of diametric spokes, N. The total number of projections, TP, remained constant (TP = 8192). Images were acquired using the 32 channel head coil with the following protocol: 300 mm FOV, matrix size 128x128x128, TE/TR 1.65/4.91 ms, 1002 Hz/px, flip angle 8°.

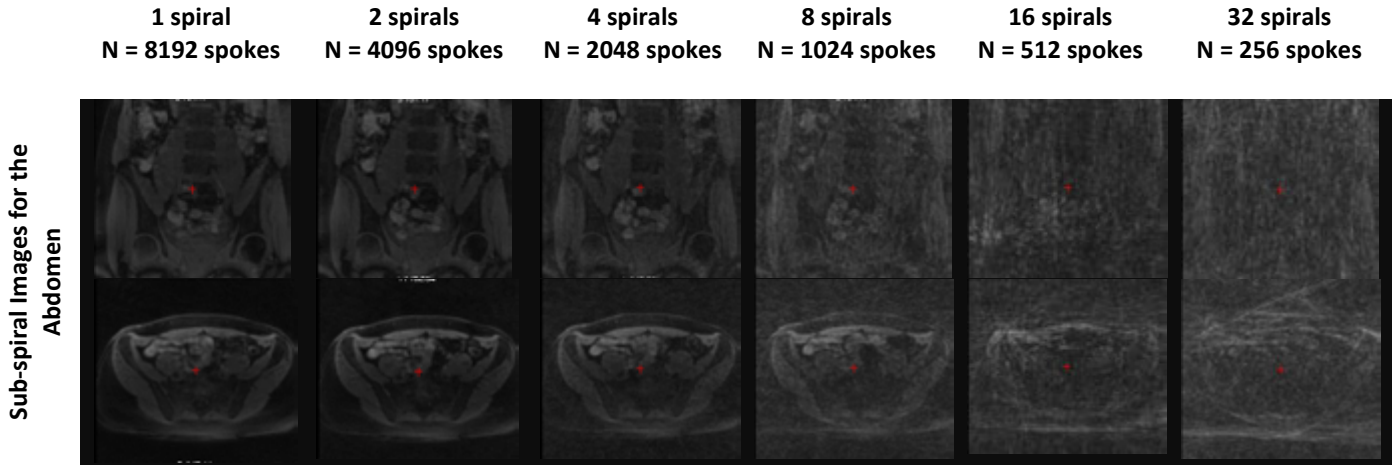

Figure 4.15. Coronal (top) and axial (bottom) views of sub-spiral images from abdominal scans acquired with decreasing N and constant TP = 8192. Scans were acquired using the 18 channel body array flex and spine array coils with the following protocol: 300 mm FOV, matrix size 128x128x128, TE/TR 2.18/5.80 ms, 1002 Hz/px, flip angle 8^{o} and with water excitation applied.

In contrast, for abdominal scans, sub-spirals acquired with 512 diametric spokes were severely degraded. As such, the minimum number of spokes per sub-spiral for abdominal scans was deemed to be 1024, which can be acquired in 5.9 s with WE applied, or 5 s without WE applied. Figures 4.16 and 4.17 show how sub-spiral acquisition times and SNR decrease for increasing numbers of sub-spirals and fewer spokes per sub-spiral, respectively. SNR was calculated in an ROI in muscle.

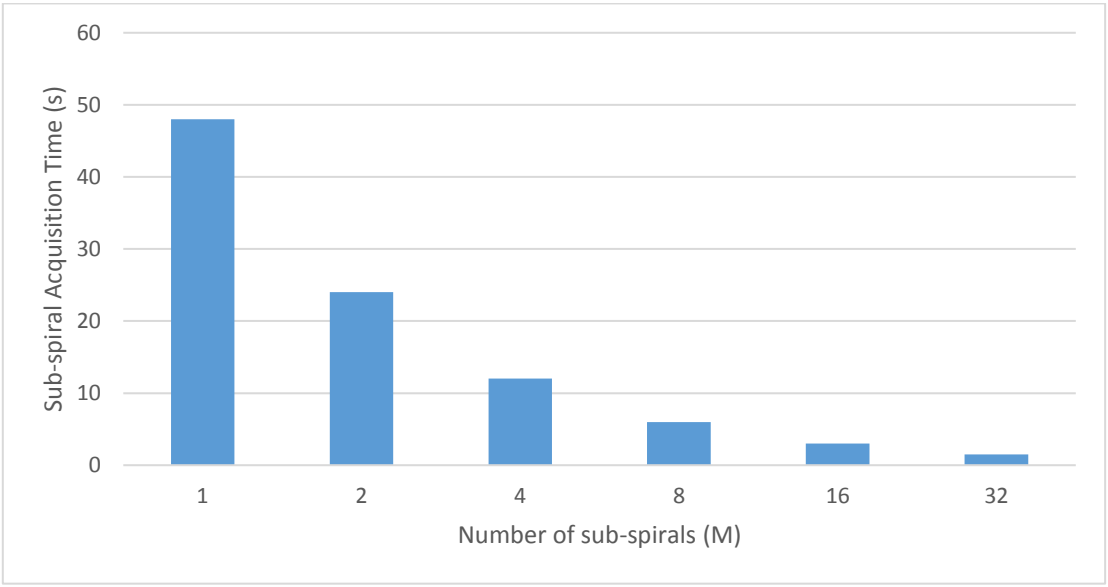

Figure 4.16. Graph showing how the acquisition time per sub-spiral decreases as the number of sub-spirals, M, increases, for a fixed total number of projections (TP = 8192) and fixed scan time of 48 seconds.

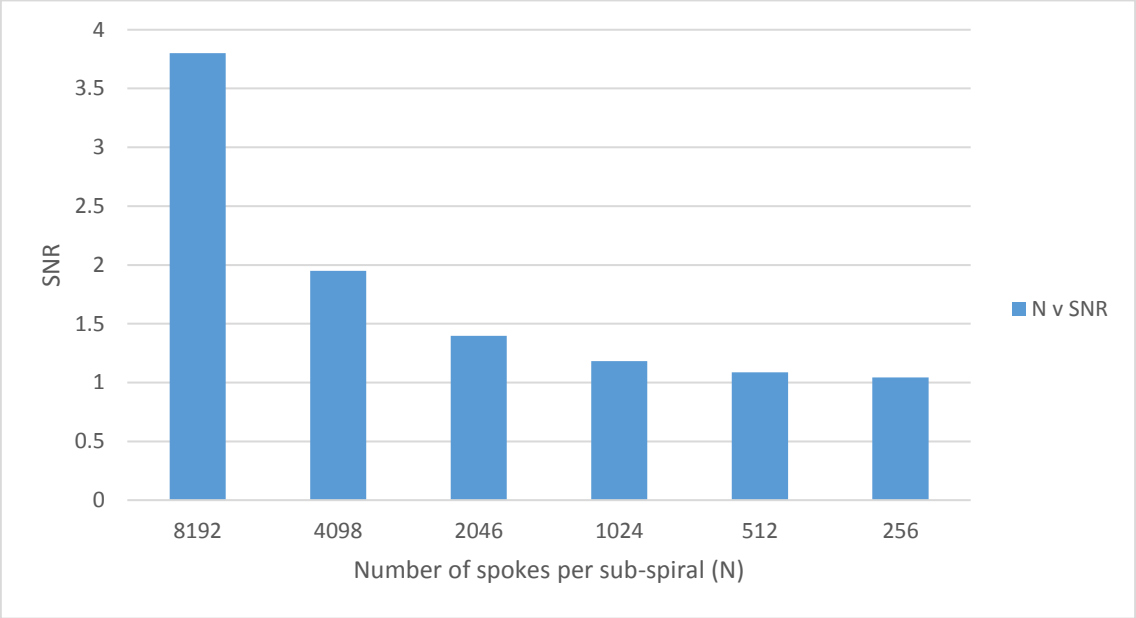

Figure 4.17. Graph showing how the signal-to-noise ratio (SNR) in muscle of sub-spiral images acquired during an abdominal scan decreases with decreasing numbers of diametric spokes, N.

4.3. Comparison between the 3D Radial and 3D Cartesian FLASH Sequences

Effect of Breathing

The images presented in Figure 4.18 demonstrate in two volunteers how breathing-motion artifacts present differently in 3D Cartesian and radial FLASH acquisitions. The images from breath hold acquisitions are presented on the left, and images acquired during free breathing on the right. The signal from fat is very difficult to spoil because fat has a short T1 and relatively long T2, and the accumulated gradient moment is not constant due to respiratory-related motion. Therefore fat gives rise to visible artefacts in the output images.

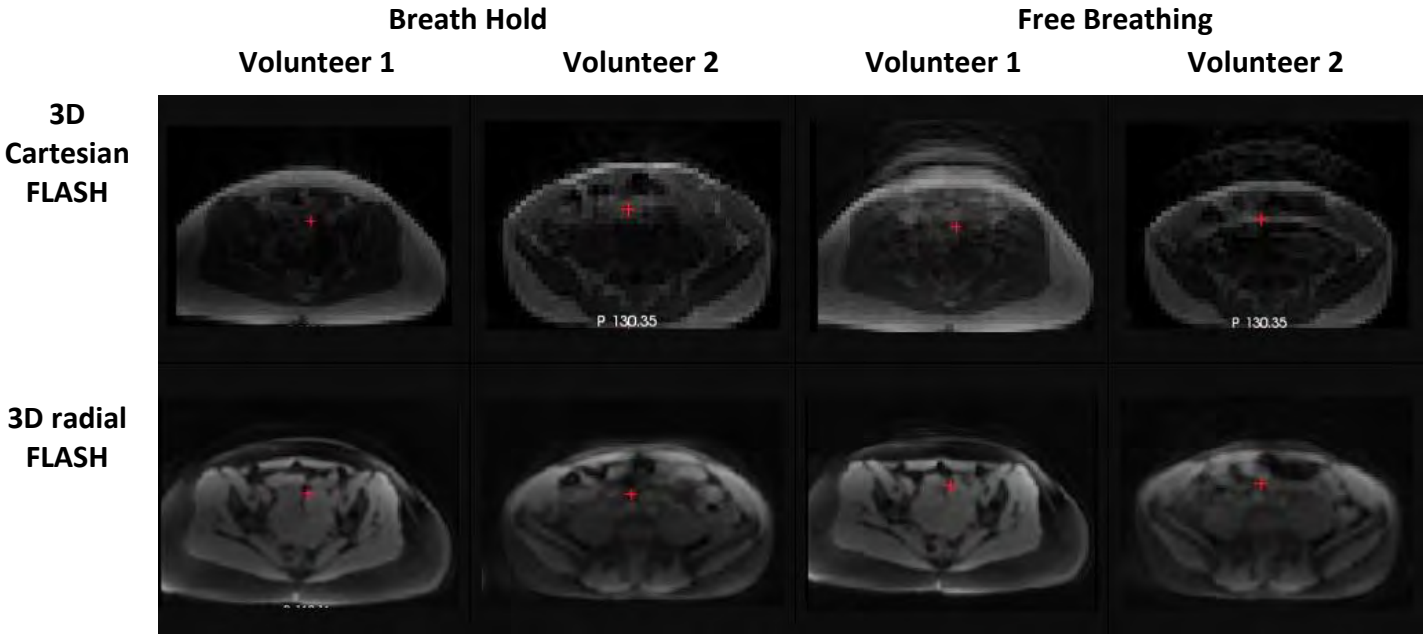

Figure 4.18. Figure showing the effect of breathing motion on images acquired with 3D Cartesian FLASH and 3D radial FLASH sequences. The images on the left were acquired in a single breath hold while the subject breathed freely during acquisition of the images on the right. Radial protocol: 400 mm FOV, matrix size 128x128x128, TE/TR 1.46/4.23 ms, flip angle 4^o. Cartesian protocol: TE/TR 1.3/4.2 ms, 400 mm FOV, 5 mm slice thickness, 25^o flip angle, base resolution 64.

Effect of Rigid Body Motion

3D Cartesian FLASH **3D radial FLASH**

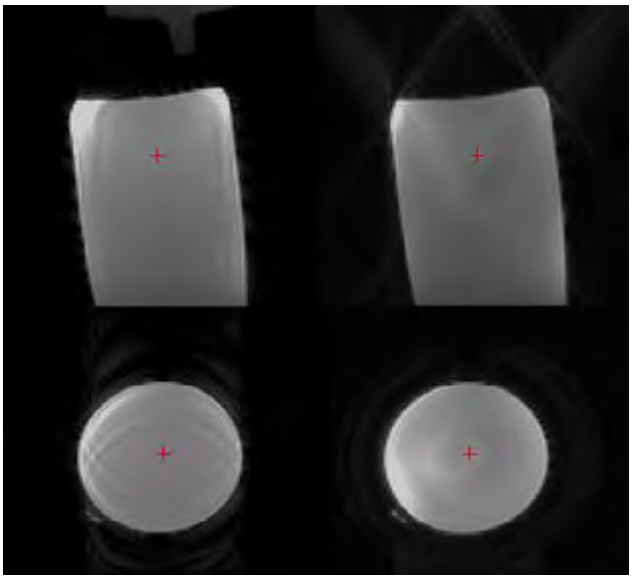

Figure 4.19. Figure comparing the effects of motion on phantom images acquired with the 3D Cartesian FLASH and 3D radial FLASH sequences. The phantom was manually moved for a period of 2 seconds at 38 seconds into the scan.

Figures 4.19 and 4.20 show phantom and brain scans, respectively, acquired with the 3D Cartesian and radial sequences in the presence of motion. In both these cases, the object returned to its original position after the motion occurred and the motion lasted roughly 2-4 s, which is of the order of the time it takes to acquire a single sub-spiral during a radial acquisition. Figure 4.21 is the corresponding motion plot to show how the participant tilted their head down and back to its original position during the acquisition of sub-spiral 8. In contrast, the subject did not move his head back to its original position for the image acquired with the radial sequence in Figure 4.22. Figure 4.23 is the corresponding motion plot that shows how the subject remained in the new position after moving his head in the z-direction (nodding motion) between the acquisition of sub-spirals 7 and 8.

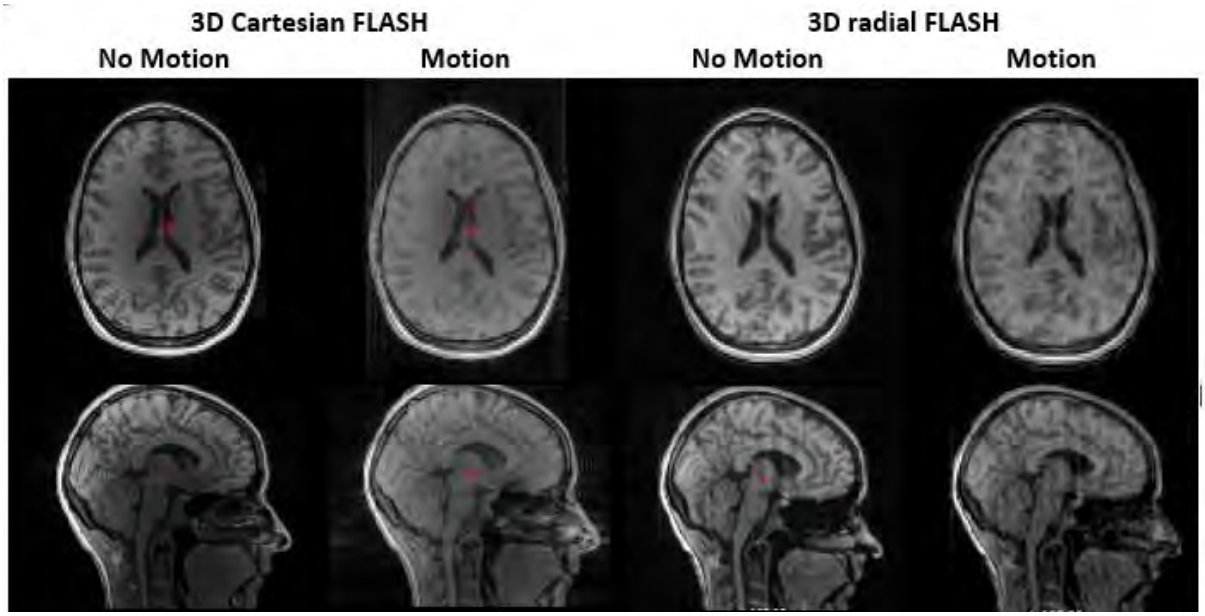

Figure 4.20. Axial and sagittal images comparing the effects of motion in 3D Cartesian FLASH and 3D radial FLASH acquisitions when scanning an adult brain. The volunteer was asked to tilt their head down and back again at 38 seconds into the scan, over the course of approximately 4s.

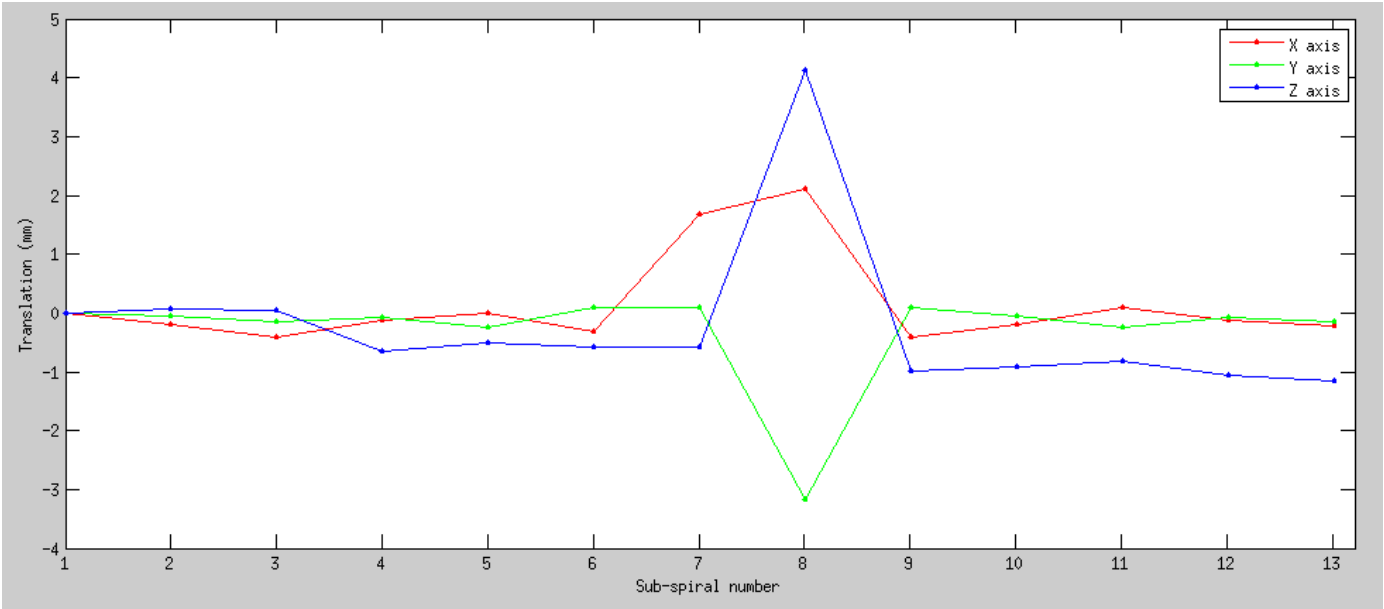

Figure 4.21. Motion plot generated by registering sub-spiral images for M=2, 3….13 to the first sub-spiral image.

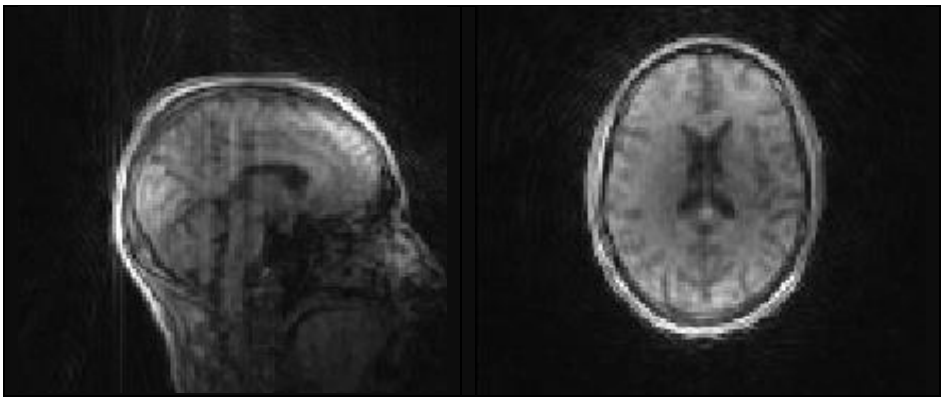

Figure 4.22. Sagittal and axial images from a 3D radial acquisition when the volunteer did not return to his/her original position after moving.

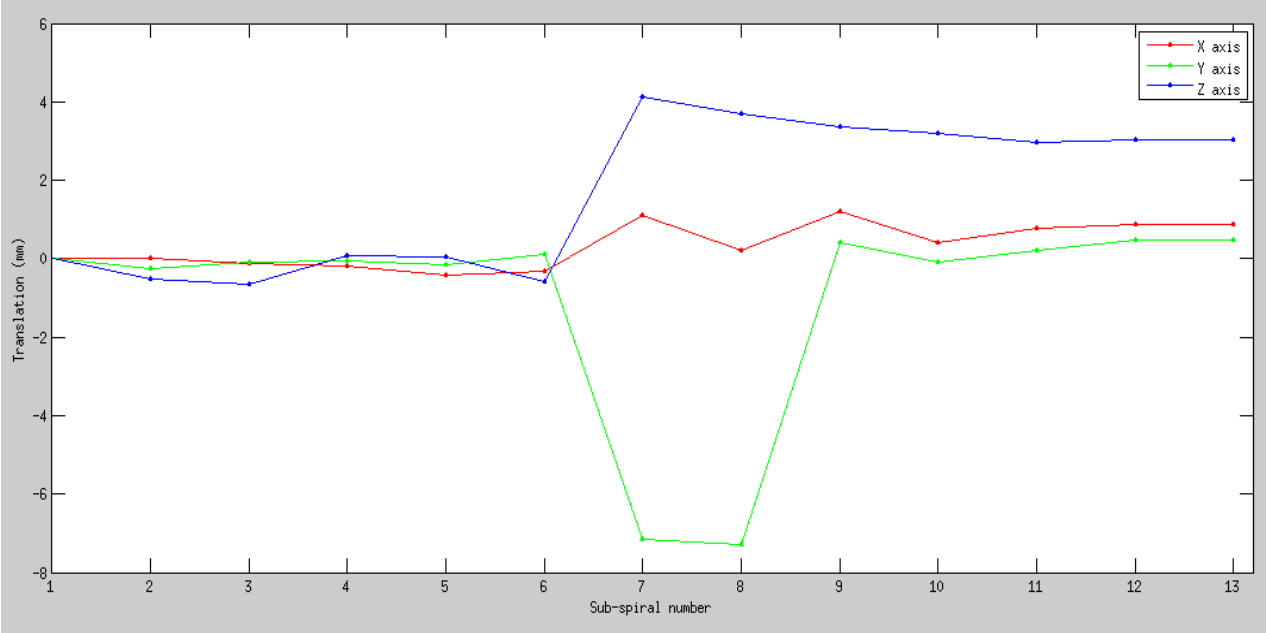

Figure 4.23. Motion plot generated by registering sub-spiral images for M=2, 3….13 to the first sub-spiral image.

4.4. Reconstruction of Navigator Images

Tests to Demonstrate the Potential of a Segmented Scan for Self-navigation Applications

Figure 4.24 shows phantom images for each of four sub-spirals as well as the image generated after combining the sub-spiral images. Limited streaking artifacts are evident outside the region of interest in sub-spiral images. SNR in the region of interest in the individual sub-spiral images was and average of 3.29 and in the combined volume was 5.62.

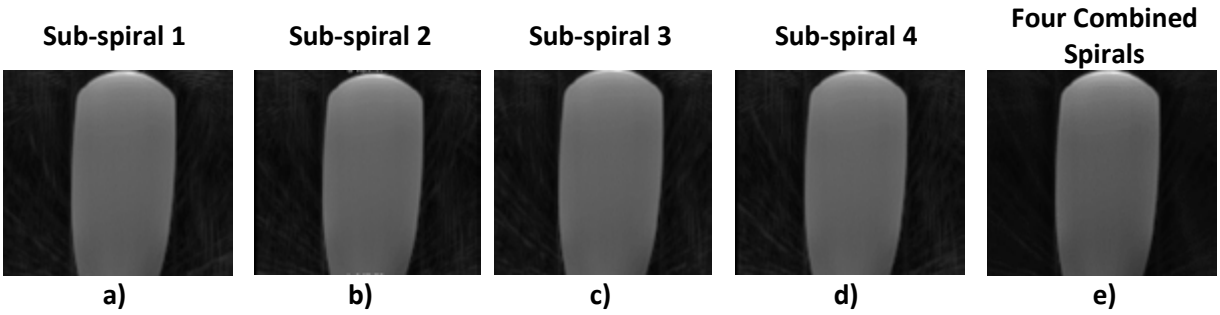

Figure 4.24. Phantom images for each of four sub-spirals (a-d) comprising N=1024 spokes, as well as the image produced by combining sub-spiral images in image-space (e).

Figure 4.25 is the corrupted image reconstructed from the combination of all sub-spirals for an adult volunteer who moved intentionally once mid-way during the acquisition. Figure 4.26 shows two sub-spiral images from the same acquisition. The image for sub-spiral 7 shown on the right is severely corrupted compared to the image for sub-spiral 2 on the left. Motion plots demonstrate significant translation (of the order of 4 to 8 mm) in the y and z directions between the acquisitions of sub-spirals 6 and 7 (Fig. 4.27). Figure 4.28 shows images reconstructed from the combination of sub-spiral data before the motion occurred (1 to 6) and after the motion occurred (8 to 13), excluding the motion corrupted sub-spiral 7.

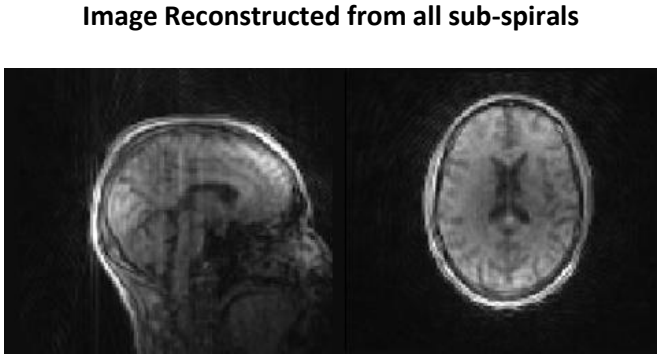

Figure 4.25. Image reconstructed using all sub-spirals, including those corrupted by motion.

Sub-spiral 2 **Sub-spiral 7**

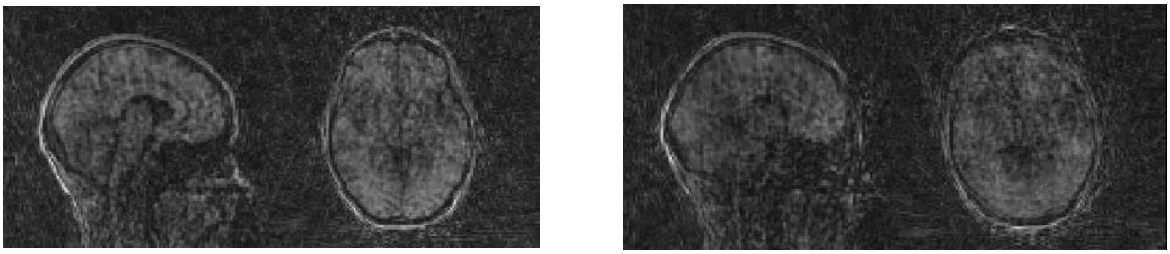

Figure 4.26. Two sub-spiral images. Each sub-spiral comprised N=1024 diametric spokes. The image on the right is severely corrupted by motion.

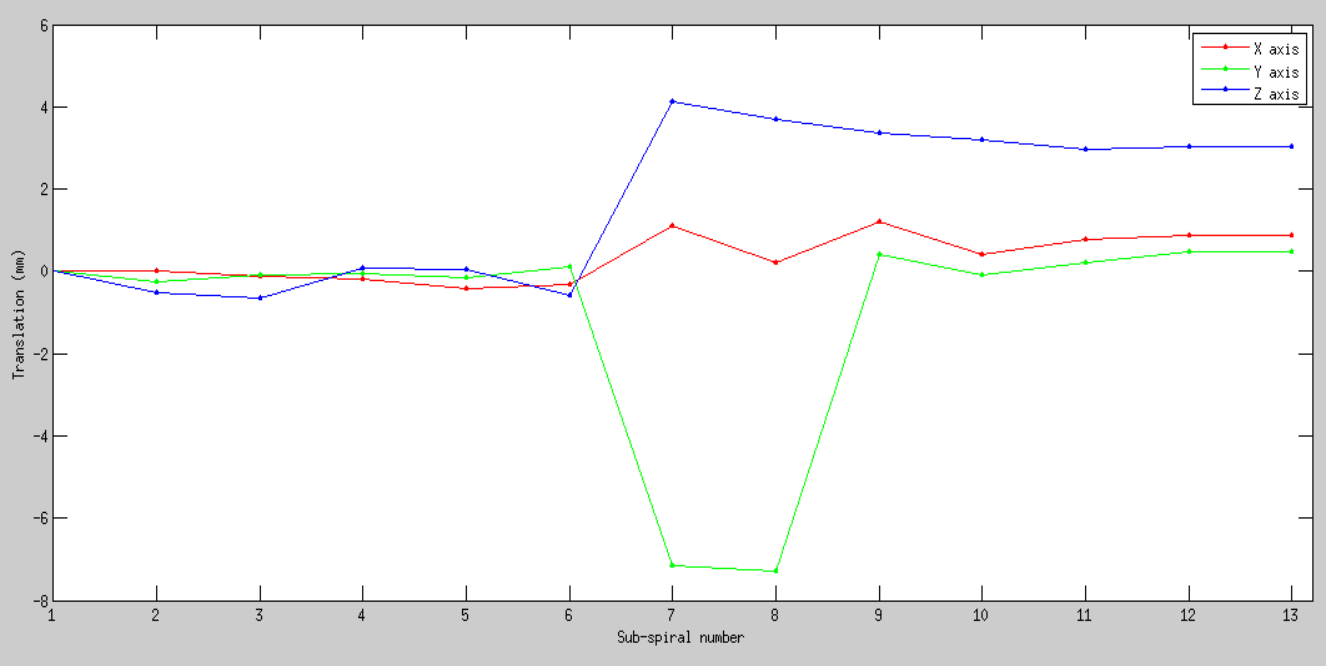

Figure 4.27. Motion plot showing translation during the scan.

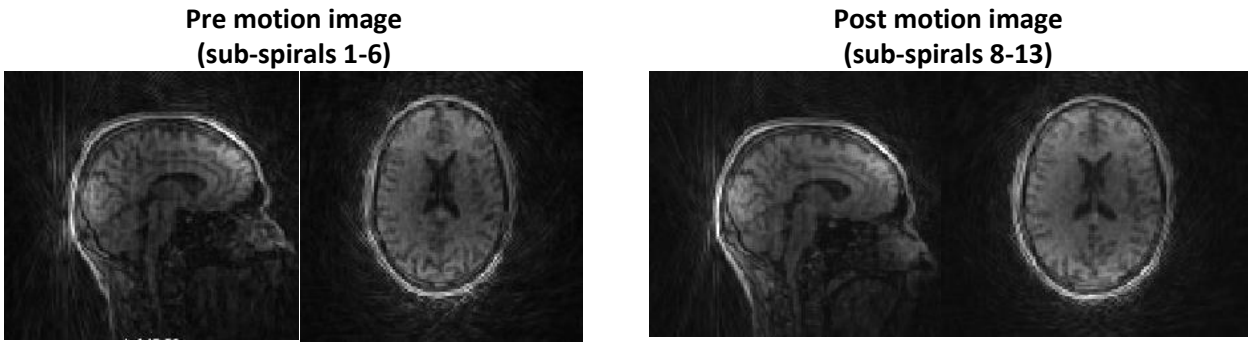

Figure 4.28. Images reconstructed from sub-spirals preceding the motion (left) and from sub-spirals acquired after the motion occurred (right). The motion-corrupted sub-spiral was excluded from image reconstruction.

Next we examined the effect of applying motion correction directly to each reconstructed sub-spiral image before combining these into a single volume. The transformation matrices were added to the text file that is used during image reconstruction and applied immediately to the reconstructed sub-spiral images. Entries in a typical text file are shown for one sub-spiral in Figure 4.29. Combining these co-registered sub-spiral images, after exclusion of the severely motion-corrupted sub-spiral 7, generates the image shown in Figure 4.30.

```
                1024        1024

4x4 3D Affine   0.9645    -0.2183    -0.1486     61.6193
transformation  0.2416     0.9566     0.1628    -55.0300
matrix          0.1066    -0.1929     0.9754     14.3030
                0          0          0          1
```

Figure 4.29. Text file containing the registration matrix used during the reconstruction of sub-spiral 2

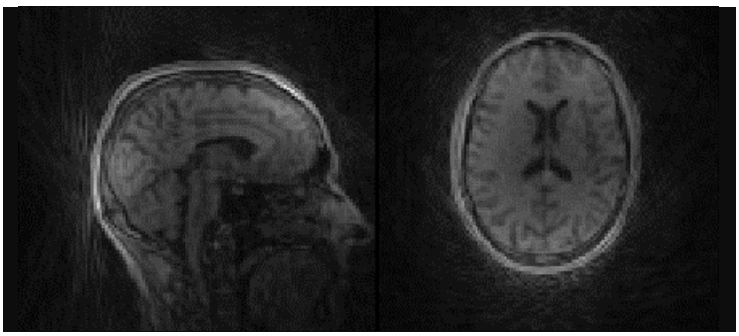

Figure 4.30. Image obtained by combining co-registered sub-spiral images. Severely corrupted sub-spiral images were excluded.

Reconstructing with a Smaller Base Resolution

Nyquist artifacts that arise from under-sampling the outer edges of k-space are reduced in phantom navigator images reconstructed at a reduced base resolution of 64 (Fig. 4.32) compared to the scan base resolution of 128 (Fig. 4.31).

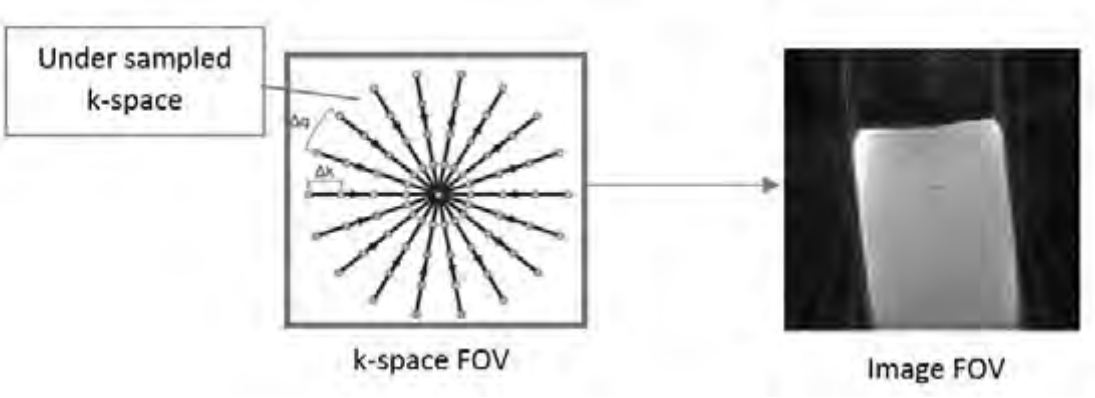

Figure 4.31. Figure to show the presence of streaking artifacts due to under-sampling of high spatial frequencies. Reconstructed base resolution is 128.

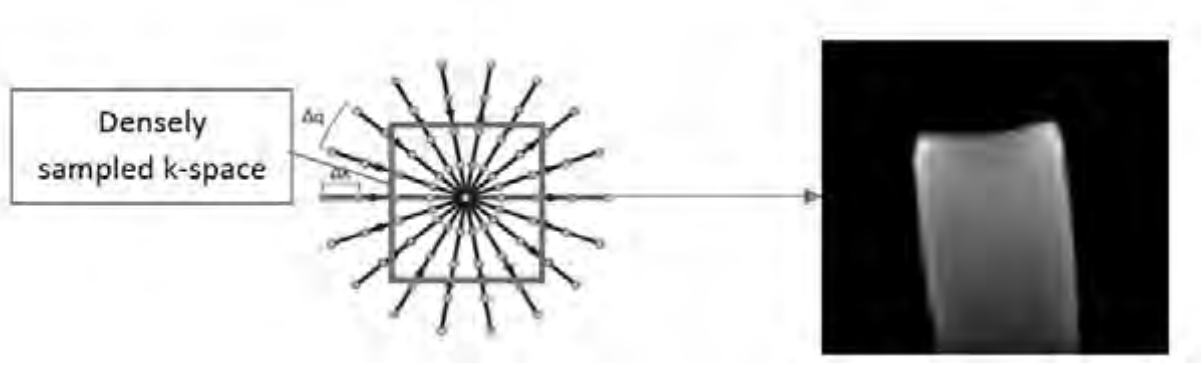

Figure 4.32. Figure to show how streaking artifacts can be reduced by reconstructing the image at a reduced base resolution of 64.

Figure 4.33 compares single sub-spiral images acquired with 512 or 256 diametric spokes, respectively, and reconstructed at the scanned base resolution of 128, or reduced base resolutions of 96 and 64. Notably, the image reconstruction time decreases significantly as the base resolution is reduced. Sub-spiral images unaffected by motion were selected for this comparison.

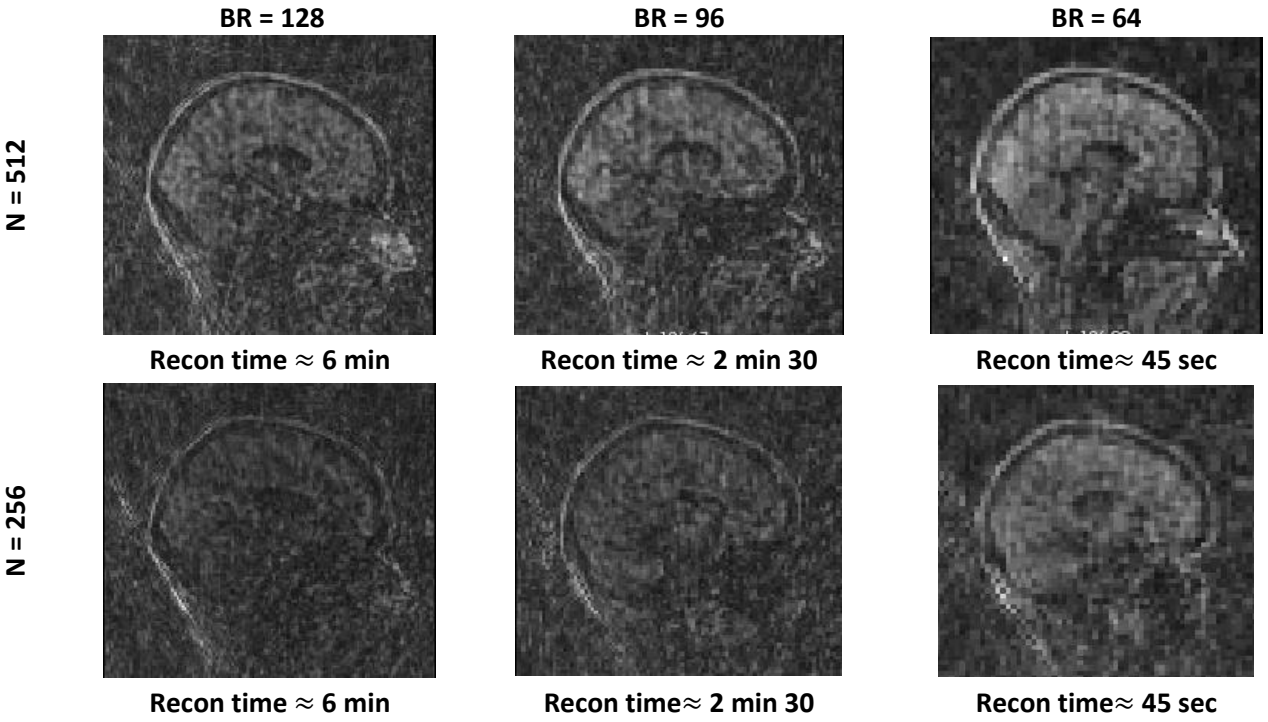

Figure 4.33. Comparison of sub-spiral images acquired with different numbers of diametric spokes and reconstructed at different base resolutions. Image reconstruction times are also given.

Figure 4.34 shows how the subject moved during the first acquisition, for which 24 sub-spirals were acquired with 512 diametric spokes each. The temporal resolution of motion tracking is determined by the sub-spiral acquisition time, which was 2.6 s in this case. Despite significant translations in the y-direction, it was only the large translation in the z-direction corresponding to lowering of the chin (head nodding) between sub-spirals 12 and 13 that resulted in a severely corrupted sub-spiral image. As such, data from sub-spiral 13 was discarded and not included in the final image generated when the co-registered sub-spiral images were combined.

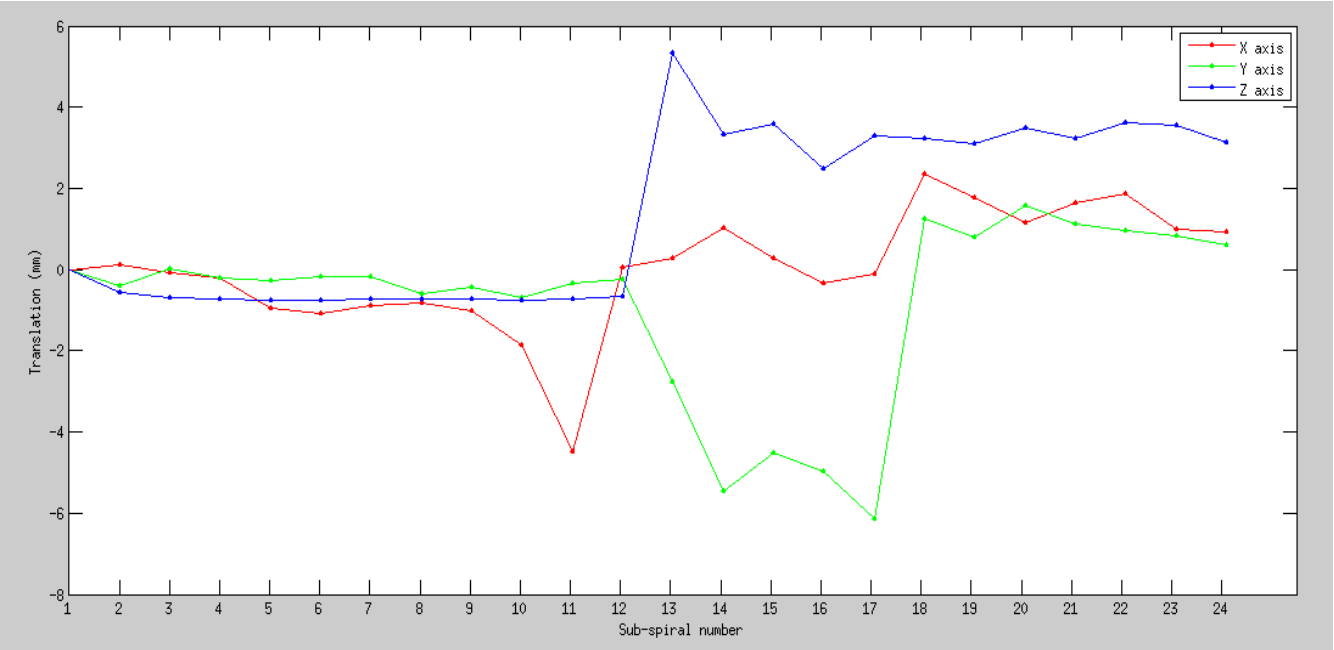

Figure 4.34. Motion plot showing translations in each direction during the first acquisition acquired with 24 sub-spirals comprising 512 spokes each.

Figure 4.35 compares the image obtained when combining sub-spiral data in k-space prior to reconstruction to the image obtained when combining co-registered sub-spiral images in image-space. The image on the left was obtained by performing reconstruction after combining the k-space data of all 24 sub-spirals. As such, data from motion corrupted sub-spirals and sub-spirals acquired when the head was in a different position are included in this image, leading to reduced image quality compared to the image on the right that was obtained by combining co-registered sub-spiral images after discarding any motion corrupted sub-spiral images.

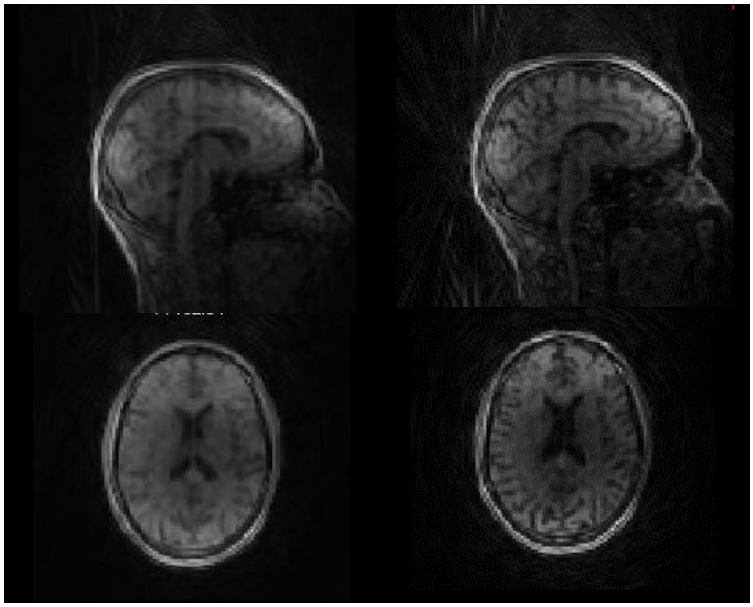

Figure 4.35. Comparison of image quality when sub-spiral data are combined in k-space (left) or image-space (right). For the image on the left, data from all 24 sub-spirals were combined in k-space prior to image reconstruction, while the image on the right was obtained by combining the 23 non-motion-corrupted co-registered sub-spiral images.

Figures 4.36 and 4.37 show the same results for the second acquisition during which 48 sub-spirals were acquired with *N*=256 diametric spokes each, reducing the sub-spiral acquisition time to 1.25 s. However, in this case sub-spiral images were initially reconstructed at a reduced base resolution of 64 to reduce Nyquist artifacts arising from under-sampling of k-space. The motion plot demonstrates that this strategy facilitated accurate co-registration of sub-spiral images enabling motion tracking at a higher temporal resolution. The images of sub-spirals which were significantly corrupted by motion, were excluded from subsequent reconstructions. Sub-spiral images were then reconstructed again at the scanned base resolution of 128 and co-registered using the previously computed transformation matrices before being combined to obtain the final volume shown on the right in Figure 4.37. The image on the right shows significant improvement compared to the image on the left that was reconstructed after combining k-space data from all 48 sub-spirals.

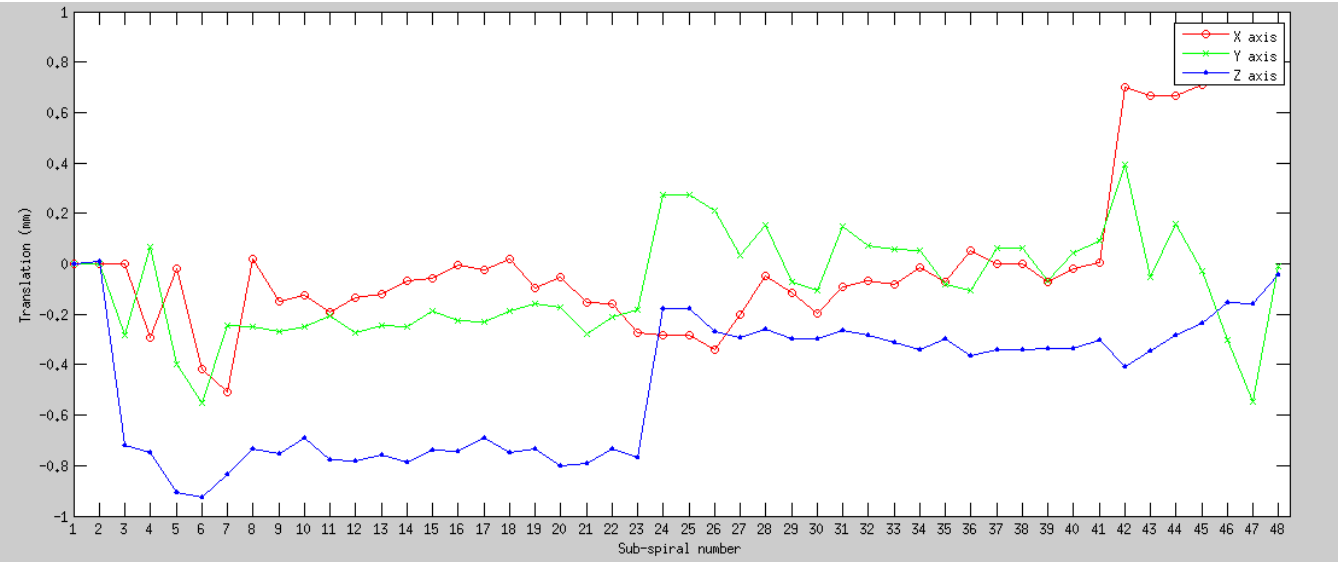

Figure 4.36. Motion plot showing translations in each direction during the second acquisition acquired with 48 sub-spirals comprising 256 spokes each.

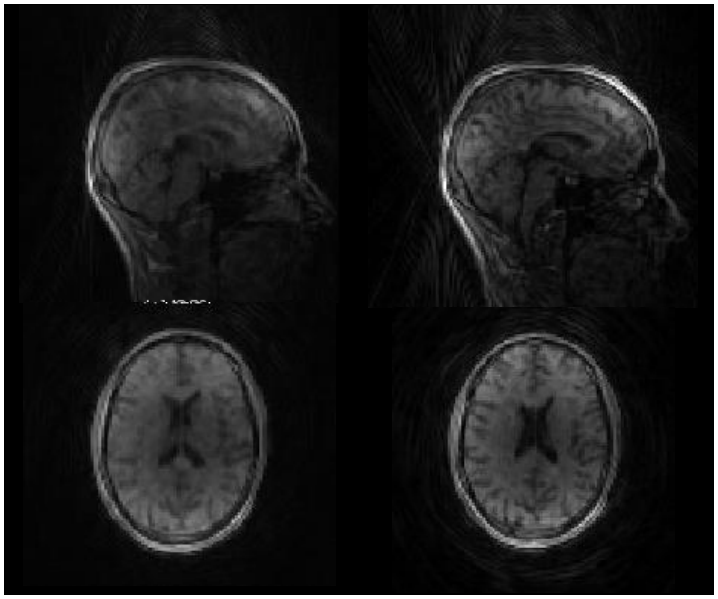

Figure 4.37. Comparison of images constructed from sub-spiral data that were combined in k-space (left) or image-space (right). For the image on the left, data from all 48 sub-spirals were combined in k-space prior to image reconstruction, while the image on the right was obtained by combining the 46 non-motion-corrupted co-registered sub-spiral images.

4.5. *In vivo* Fetal Scans with the Optimized Protocol

The images in Figure 4.38 were acquired in subject A, a healthy volunteer pregnant with twins. The acquisition was performed with the Ernst flip angle of 4° to maximise signal for a TR of 5.8 ms and a T1 value of 2617 ms. Figures 4.39 and 4.40 are images acquired with a higher BW and at a higher flip angle of 7° in the second pregnant mother, subject B. Figure 4.39 show some of the sub-spiral images and Figure 4.40 the image obtained after combining data from all the sub-spirals in k-space prior to reconstruction. During the acquisition the SAR measured in Normal Mode over the torso was 0.7 W/kg, which is about 35% of the maximum allowed SAR of 2 W/kg.

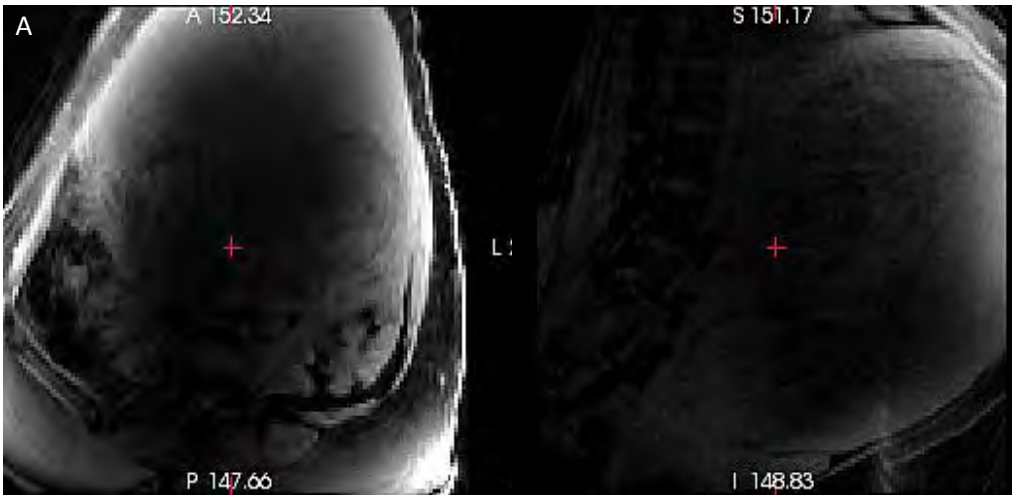

Figure 4.38. Fetal images acquired at the Ernst angle of 4° in the first volunteer (A) pregnant with twins at around 36 weeks gestation. This image was produced from reconstructing all 16384 spokes.

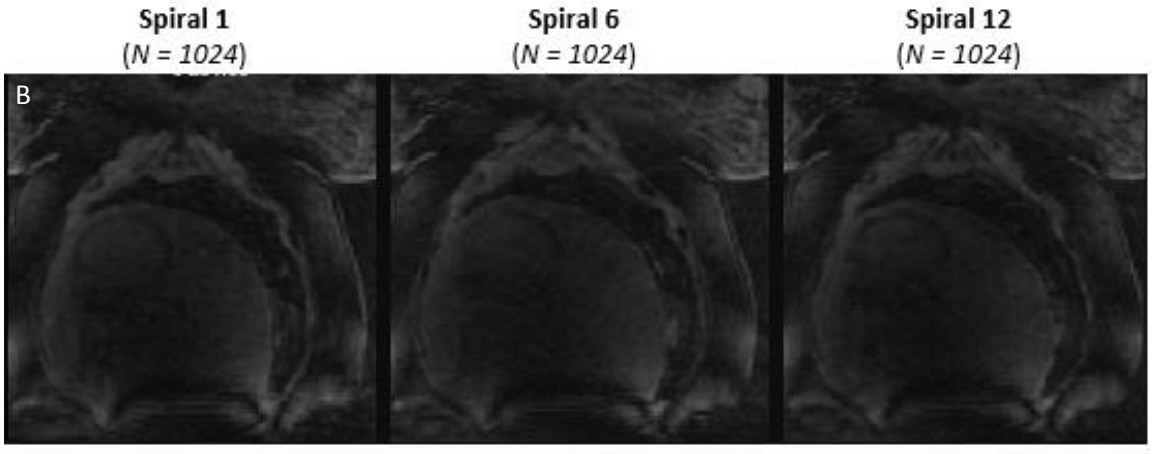

Figure 4.39. Individual sub-spiral images acquired in subject B at around 33 weeks gestation. Each sub-spiral comprised 1024 spokes. The flip angle was 7 degrees and the BW 1002 Hz/px.

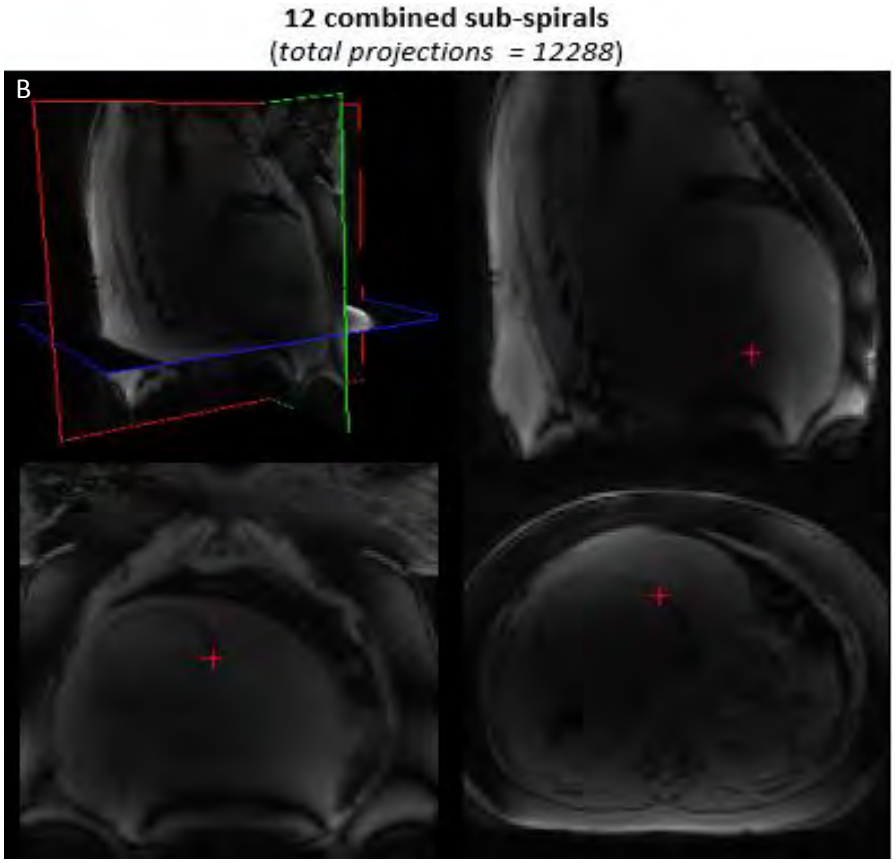

Figure 4.40. Sagittal, coronal and axial views of the image obtained in subject B after combining data from all 12 sub-spirals. The 12 288 projections were acquired in 1 min 15 s.

Figure 4.41 compares images for a single sub-spiral (*N* = 1024 spokes) acquired in subject B reconstructed at the scanned base resolution of 128 and a reduced base resolution of 64. Figure 4.42 demonstrates that images reconstructed at the reduced base resolution could be used for accurate motion tracking of the fetal brain throughout the scan. The transformation matrices generated from this co-registration were then used to register sub-spiral images reconstructed at the scanned base resolution before combining them into a single volume in image-space. The image generated in this way is compared in Figure 4.43 to the one obtained when combining k-space data from all the sub-spirals prior to reconstruction.

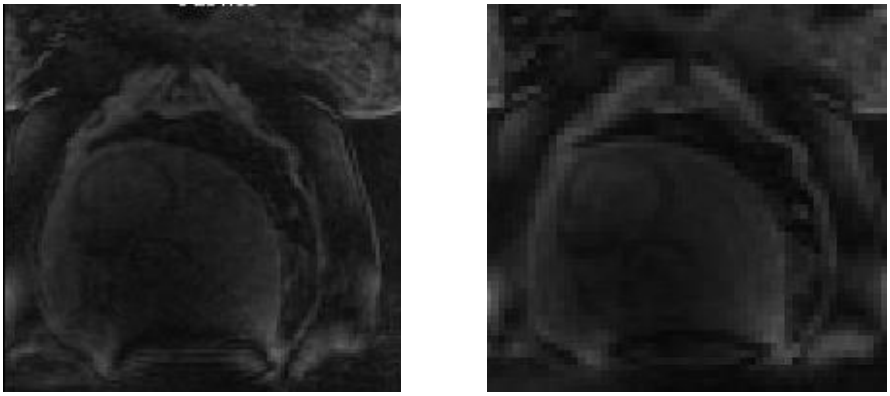

Figure 4.41. Sub-spiral 1 acquired in subject B with 1024 diametric spokes reconstructed at a base resolution of 128 (left) and 64 (right), respectively.

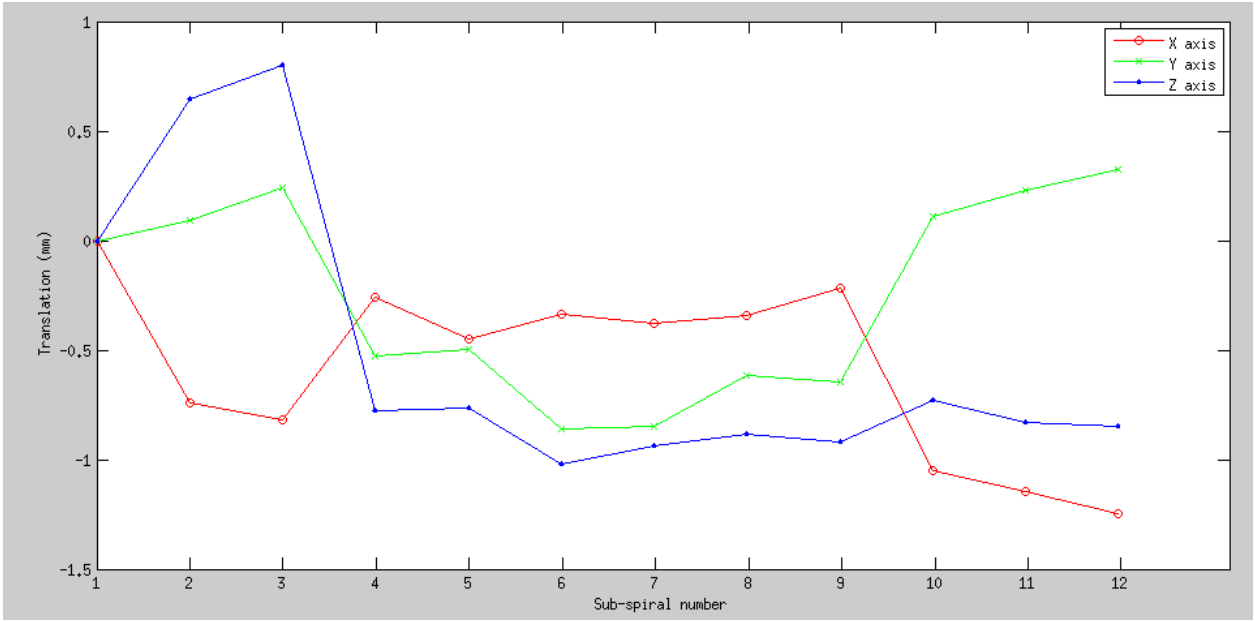

Figure 4.42. Motion plot produced from co-registering successive fetal navigator images acquired in subject B to the first navigator image.

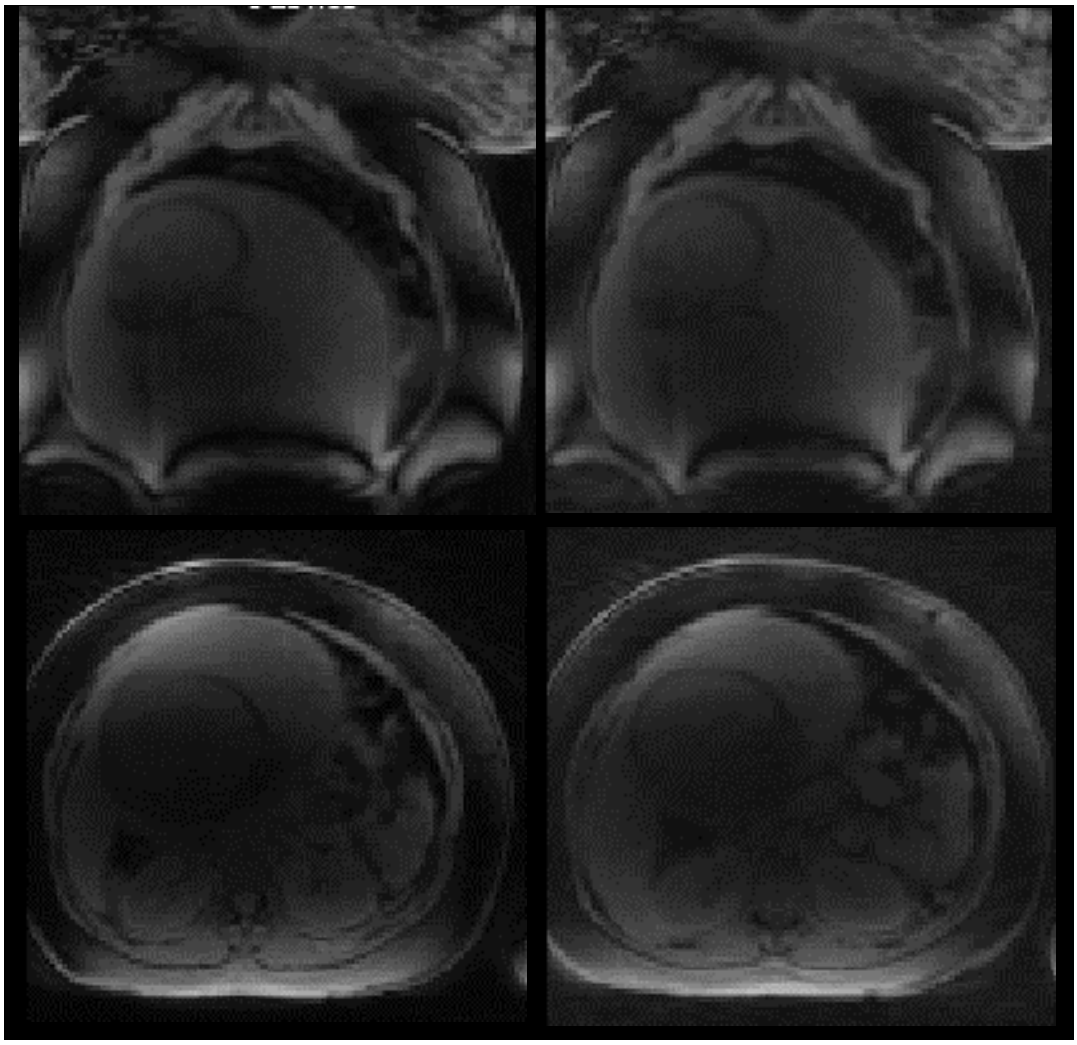

Figure 4.43. Coronal (top) and axial (bottom) view of the image obtained in subject B when combining data from individual sub-spirals in k-space before reconstruction (left) compared to the image obtained when combining co-registered sub-spiral images in image-space (right).

5. Discussion

5.1. Sequence Development

The 3D radial mode of the standard Siemens CV sequence that was used as the basis for this work, has not been modified since its introduction in software version VB17 in 2008 [72]. Therefore, some modifications were needed before an optimized radial trajectory could be developed. Spoiler gradients were added to the Gradient Echo mode of the standard Siemens CV sequence after each readout. These gradients destroy any residual transverse magnetization so that the generated signal depends on longitudinal magnetization only. This makes the image contrast easier to control when optimizing the flip angle for the final scan protocol and enables shorter TR times since there is no need to wait for the transverse magnetization to relax, thus facilitating shorter scan times.

Subsequently, the sequence was modified to acquire a segmented scan comprising multiple sub-volumes of data within a single acquisition. Equations developed by Wong and Roos [53] that allow the user to specify the number of sub-volumes and the number of projections per sub-volume were implemented. Since the starting points of the diametric spokes generated by these equations are distributed on the surface of a hemisphere, and the end points on the opposite hemisphere, a half-spiral trajectory of starting points from equator to pole fully samples k-space in a spherical volume. Since each diameter contains both high and low spatial frequencies, a low resolution image can be reconstructed from a sub-spiral containing relatively few diametric spokes making it suitable for self-navigation applications. The series of low-resolution images generated at constant time intervals provide information on the position of the object being scanned throughout the scan and successive images can be co-registered to provide information on motion that may have occurred.

The quality of the images reconstructed from each sub-spiral and from the combination of the sub-spirals were compared for four different starting point trajectories, namely interleaved sub-spirals, overlapping sub-spirals, rotated sub-spirals, and indexed sub-spirals. Interleaved sub-spiral images were heavily corrupted by streaking artifacts (Fig. 4.1a). Although start and end points would be uniformly distributed on the surface of a sphere if the total number of projections were used in a single spiral, increasing the number of sub-spirals reduces the number of projections per sub-spiral. This increases the steps between successive polar angles and reduces increments between successive azimuth angles, which essentially leads to larger gaps between levels in the spiral trajectory and more densely spaced points on the trajectory. Unsampled k-space in the gaps between adjacent levels in the spiral trajectory gives rise to streaking artifacts. These artifacts disappear when all the sub-spirals are combined prior to reconstruction of the final 3D volume due to the gaps in k-space being filled (Fig. 4.1b). The quality of the sub-spiral navigator images could be improved by increasing the number of spokes (*N*) per sub-spiral, which would reduce the polar angle increments and introduce more levels in the spiral trajectory. This would, however, increase the time required to acquire each navigator volume and jeopardize the temporal accuracy of motion tracking.

Modifying the sampling scheme to generate a single overlapping sub-spiral comprised of a subset of the total number of projections, reduces the gaps between levels in the spiral trajectory and increases the distance between adjacent starting points on the spiral trajectory, resulting in starting points that are uniformly distributed on the surface of the hemisphere. This sampling strategy reduced the streaking artifacts in the sub-spiral image (Fig. 4.2a). However, repeatedly sampling a number of identical undersampled sub-spirals still results in a final volume that is sparsely sampled, albeit uniform. Since streaking artifacts arise from unsampled gaps in k-space and these occur in the same

position for every sub-spiral, artifacts are amplified in the image reconstructed from the combined sub-spirals (Fig. 4.2b).

The rotated spiral distribution reduced the accumulation of streaking artifacts in the image reconstructed from the combined sub-spirals (Fig. 4.3b). Since each sub-spiral now samples different points in k-space, the combination of the sub-spirals results in a more densely sampled k-space, thus reducing artifacts arising from unsampled k-space. Notably, for the combined volume the start and end points are not distributed uniformly on the surface of the sphere, as polar angles were not computed based on the total number of projections but using the number of projections per sub-spiral resulting in larger gaps between spiral levels than would be required for uniform sampling, which may explain why the resolution of the final reconstructed image is lower than would be expected for 4096 projections.

The combined indexed sub-spirals achieve a densely-packed uniform distribution of start and end points on the surface of a sphere, thus minimizing streaking artifacts in the final combined image (Fig. 4.4b). Although not immediately obvious, the start and end points are not uniformly distributed for the individual sub-spirals using this strategy. This is most evident in Figure 4.7, for larger values of M, and arises from the fact that rotations at different levels of the spiral trajectory consist of different numbers of points, so that the indexed points are effectively randomly distributed on the surface of the sphere. Despite this non-uniform distribution, no artifacts are evident in the sub-spiral images in Figure 4.4a. This random distribution further minimizes the risk of interaction between sub-spiral signals (eddy currents) and prevents super-positioning of streaking artifacts when the same area of k-space is unsampled.

The different strategies essentially achieve either uniform sampling of start and end points for the individual sub-spirals or for the combination of sub-spirals. This is illustrated in Figure 4.5 where the distribution of start and end points for 8 combined sub-spirals corresponds to the uniform distribution arising from a single spiral with the same total number of projections only for the interleaved and indexed sub-spirals. Optimizing the sub-spiral sampling distribution, as in the overlapping and rotated sub-spirals, limits the resolution of the final image due to non-uniform sampling of k-space in the combined volume. It is worth noting that even though the overlapping sub-spirals achieve a uniform distribution of start and end points for both individual sub-spirals and the combined volume, both volumes are severely undersampled resulting in gaps in k-space which give rise to significant streaking artifacts. Since our ultimate aim is to obtain the best possible image after combining the sub-spirals, the optimal strategy should achieve a densely-packed uniform sampling of the combined volume, while minimizing artifacts in the individual sub-spirals used for motion tracking.

The temporal resolution of motion tracking with sub-spiral images can be increased by increasing the number of sub-spirals per acquisition. Since increasing the number of interleaved sub-spirals, increases regions of unsampled k-space between levels of the spiral trajectory in individual sub-spirals causing significant streaking artifacts in the sub-spiral images (Fig. 4.6), the indexed sampling strategy was chosen for this project. This sampling scheme provides a complete data set with optimal sampling of k-space.

5.2. Protocol Development

Due to the uniqueness of the 3D radial sequence developed here, it was necessary to determine protocol values specifically suited for scanning a fetus with this sequence. This proved challenging since there were no similar protocols to our knowledge which could be used as a starting point. Additionally, due to the scarcity of pregnant mothers requiring MRI for clinical reasons and the

complicated ethics surrounding scanning pregnant volunteers, protocol parameters needed to be optimized based on abdominal and brain scans performed in non-pregnant volunteers.

Optimal Flip Ange Choice

Since the measured signal intensities for different flip angles closely followed those predicted by the signal equation (eqn. 3.1) in kidneys, muscle and subcutaneous fat for a healthy non-pregnant volunteer (Figs. 4.8 and 4.9), we decided to use the flip angle that should theoretically provide optimal contrast between amniotic fluid and fetal brain, namely 7 degrees. It should be highlighted though that T1 values are not known for fetal white and grey matter separately, but only an estimate of T1 for fetal brain tissue [67]. As such, we were not able to select a flip angle that would optimize contrast between white and grey matter.

Bandwidth and Saturation Choice

Fine streaking artifacts were present in participants who had a thicker layer of subcutaneous fat (Fig. 4.10). The dependence on fat originally suggested some form of chemical-shift artifact. Since chemical-shift artifacts appear mostly in the frequency encoding dimension in Cartesian scans, the acquisition of data in all three dimensions simultaneously followed by re-gridding could cause the artifact to appear differently. The images in Figure 4.11 show that for such participants, applying water excitation reduces the appearance of these artifacts. For lean participants, where minimal artifacts appear at the air-skin interface anyway, the addition of a water excitation pulse did not make a noticeable difference and was therefore considered unnecessary.

For volunteers with more subcutaneous fat, increasing the bandwidth did not reduce the appearance of artifacts. The very bright signal from fat was increasingly visible at higher bandwidths. In these participants, in addition to water excitation being selected, the fewest artifacts were present at bandwidths of 500 Hz/px and 1000Hz/px. For lean participants where the signal from fat did not present a problem, the best image contrast was obtained at bandwidths greater than 1000 Hz/px.

While increasing the bandwidth in Cartesian sampling schemes reduces the displacement of the chemical-shift, the effect of BW is not so obvious in radial sampling where the artifact appears as a smear rather than a distinct translation. Since increasing the bandwidth did not appear to reduce the streaking artifacts in the images in Figure 4.11, they may not be related to chemical-shift at all. The artifacts could be a result of re-gridding the radial data, where the complex interpolation of sampled points causes signal aliasing from intense signals (such as those from fat) similar to those artifacts commonly seen in CT scans. This may explain why suppressing the signal from fat during the scan reduced the appearance of these artifacts while increasing the bandwidth was ineffective.

Increasing the bandwidth is, however, still attractive due to the substantial reduction in TR, allowing faster acquisition of sub-spirals. Since WE increases the TR (Fig. 4.12), it was decided that WE would be applied only in subjects with a substantial amount of fat. Usually, the bandwidth is chosen to achieve a balance between the shortest possible acquisition time (TE and TR) and a good SNR. In radial sequences, where the centre of k-space is significantly oversampled resulting in inherently high SNRs, higher bandwidths are possible. For these reasons, higher bandwidth values were chosen when possible to enable the shortest possible acquisition time.

Optimized values for M and N

For phantom and brain images the reconstructed sub-spirals began to display heavy Nyquist artifacts, amongst others, with fewer than N=512 projections (Figs. 4.13 and 4.14). For this number the volume is under-sampled by a factor of 201. Although the general edge detail can still be distinguished in images acquired with fewer than 512 spokes, the accuracy of motion registration may be

compromised due to the software incorrectly detecting streaking artifacts as important edges to co-register between the navigator images. Since the varying position of streaking artifacts between images is independent of the motion of the participant, registering these with one another will provide incorrect feedback.

For abdominal scans, where there are many more structures to identify and many more tissue types contributing to the signal, the fewest number of spokes that produced acceptable sub-spiral images was N=1024 (Fig. 4.15). These could be acquired in 5 seconds without WE. Figs 4.16 and 4.17 demonstrate that one cannot decrease the number of points per sub-spiral to speed up navigator image acquisition times without sacrificing image SNR, supporting the decision to limit the minimum N for abdominal scans to 1024. These results suggest that a minimum of 1024 diametric spokes would be required per sub-spiral for fetal scans.

5.3. Comparing a 3D Cartesian sequence with the 3D radial sequence

From the images in Figure 4.18 it is clear that breathing strongly affects the image quality of the 3D Cartesian scan. For this particular orientation of the participant within the scanner, breathing occurred in the Ky phase-encoding direction. As a result, severe ghosting is present in the phase-encoding direction of the image. Additionally, the ghosting artifacts overlap the anatomy which makes it very difficult to distinguish different tissues. Conversely, the 3D radial sequence exhibits very few breathing artifacts even though the breathing was continuous throughout the scan. The artifacts that are present are dispersed across the image and appear predominantly in the background so that even though they are visible, they do not accumulate over one region of anatomy and interfere with distinguishing important anatomical structures. This supports the use of radial rather than Cartesian sequences for scanning pregnant patients since the mother can breathe freely over the course of the scan without affecting the quality and usefulness of the final image.

Rotations and translations also affect the 3D radial FLASH and Cartesian scans differently. Figure 4.19 shows how motion is dispersed in all directions in the radial acquisition, thereby having an averaging effect on the artifacts. In contrast, the Cartesian sequence displays heavy ghosting artifacts in the phase encode direction. Even more notable is the difference between the effect of motion on the adult brain images in Figure 4.20, where shifting artifacts are clearly visible for the Cartesian scan but the radial scan does not have many obvious artifacts even though the scans and type of motion were equivalent.

It is likely in practice that the fetus will shift to a new position all together, possibly many times throughout the course of a scan. From the images presented in Figure 4.22, it seems possible that such severe motion may not mean that the data is rendered useless since much of the object information is preserved even though the head moved to a new position during the scan. Furthermore, there was enough detail in the individual sub-spiral images for accurate co-registration and motion tracking, despite motion of the order of 4 to 8 mm (Fig. 4.23). This is in contrast to other navigator studies where severe motion of the fetus during the acquisition of a Cartesian slice caused tracking to fail [63]. As such, radial acquisitions hold great promise for real-time motion tracking during fetal scanning. Sub-spiral images can also be co-registered and combined in image-space after acquisition.

The results from these experiments demonstrate that Cartesian sequences are more susceptible to motion artifacts than the radial sequence developed here, and that the latter is a better choice for imaging the fetus. It is also known from literature that the radial sequence is not “fussy” about when motion occurs in the scan, since every projection contributes equally to both the contrast and edge

detail in the reconstructed image. With a Cartesian sampling scheme, motion that occurs during the sampling of the central few lines in k-space for every 2D slice will have a greater effect on the image quality as these are the only lines sampling the lower spatial frequency information. Furthermore, motion that occurs during the Cartesian scan will be concentrated in two directions whereas the 3D radial sequence disperses the effect of motion between three dimensions which lessens their appearance and makes the radial sequence inherently motion-insensitive.

5.4. Reconstruction of Navigator Images

The Siemens image reconstruction code was successfully modified to reconstruct individual sub-volumes of data. The results demonstrate in a stationary phantom that individual sub-spiral images can be reconstructed and then combined in image-space to yield an image with improved SNR and fewer streaking artifacts (Fig. 4.24).

For an adult brain scan where motion was intentionally performed and a volume produced by combining spiral subsets of data in k-space was corrupted by motion artifacts (Fig. 4.25), reconstructed sub-spiral images were used successfully to track motion throughout the scan. Motion could be detected visually by viewing the sub-spiral images in series (Fig 4.26), or quantified through co-registration of every sub-spiral image to the first sub-spiral image using FLIRT in FSL (Fig. 27). The motion plots corresponded well to the nodding motion that the subject was instructed to perform once during the scan. Sub-spiral images heavily corrupted by motion could be identified and discarded.

A limitation of combining sub-spiral data in k-space is that even after discarding data from corrupted sub-spirals, the position of the object being imaged may still differ in different sub-spirals due to the motion that occurred. Since there is no mechanism to co-register images in k-space, combining sub-spiral data in k-space prior to image reconstruction is not optimal in cases where motion occurred. One possible solution is to combine sub-spiral data from periods of quiescent motion to reconstruct separate sub-images containing only sub-spirals from periods when the imaged object was in the same position (Fig. 4.28). Each of these sub-images will have improved SNR compared to individual sub-spiral images. Although the SNR of the sub-images is lower than the image reconstructed from all the sub-spirals combined (Fig. 4.25), blurring due to motion is significantly reduced and the anatomical detail is clearer, providing more accurate diagnostic information. It is also possible to co-register these sub-images and combine them to produce a final image with improved SNR.

An alternative approach is to co-register sub-spiral images before combining them in image-space to generate the final image. Registration of the sub-spiral images was shown to be sufficiently accurate that applying the transformation matrices to the sub-spiral images before combining them produced an image with improved image quality and reduced blurring due to motion than the image reconstructed from the combined k-space data (Fig. 4.30). Effectively, the final image constructed in this way comprises only data from motion-free sub-spirals, which have all been co-registered, significantly reducing the effects of motion.

The temporal resolution of motion tracking is limited by the time it takes to acquire a single sub-spiral, which is determined by the number of diametric spokes acquired per sub-spiral. During protocol development it was shown in phantom and brain scans that sub-spiral images acquired with fewer than N=512 diametric spokes demonstrated severe streaking artifacts compromising accurate co-registration required for motion tracking, thus limiting the achievable temporal resolution (Fig. 4.31). To reduce streaking artifacts, which arise from under-sampling at the edges of k-space, a method was developed and implemented to reduce the k-space FOV during sub-spiral image reconstruction by

specifying a smaller base resolution. This effectively means that only data from the densely sampled central region of k-space are included in the reconstruction process thus reducing the appearance of streaking artifacts in the sub-spiral images (Fig. 4.32). Reduced spatial resolution and increased SNR were clearly visible in the sub-spiral images reconstructed at lower base resolutions (Fig. 4.33). Using this method, sub-spiral images comprising only 256 diametric spokes could be accurately co-registered, despite lower spatial resolution and increased blurring (Fig. 4.36), facilitating motion tracking at a higher temporal resolution. Prior to combining sub-spiral images to generate the final image, sub-spiral images were reconstructed again at the higher scanned base resolution and co-registered using the transformation matrices computed using the low-resolution sub-spiral images. The final image demonstrated visible improvements compared to the image reconstructed using the combined k-space data (Fig. 4.37). These methods hold great promise for more rapid motion correction during fetal scanning.

After the reduction of typical streaking artifacts, heavy aliasing was still visible in the background of navigator images in the form of diffuse, radiating bands of signal. Since more artifacts appear with fewer and fewer radial samples, their appearance is likely still linked to the heavy under-sampling of k-space. Aliasing artifacts that originate from regions of high signal intensity in the form of fine, bright lines were also frequently visible in the reconstructed images. Upon further investigation it was discovered that these forms of artifacts are common in PROPELLAR (Periodically Rotated Overlapping Parallel Lines with Enhanced Reconstruction) imaging and result from re-gridding with imperfect estimations during image reconstruction [73], [74]. Since radially sampled points are distributed between their closest corresponding positions on the regular Cartesian grid, inaccuracies are introduced in terms of the true signal coming from each k-space voxel. This translates into aliasing artifacts once the Fast Fourier Transform (FFT) is applied. With fewer and fewer radial samples, the error increases, since the sampled data are spread further apart and some voxels in the Cartesian grid will not be assigned a portion of signal. These artifacts are more prominent in regions with high signal intensity due to the fact that the intense signal from an originally sampled voxel is spread across neighbouring voxels during re-gridding so that it appears to leak across the image. Because the co-registered sub-spirals were combined in image space after re-gridding had already taken place, the artifacts are not reduced when the sub-spiral images are combined.

5.5. *In vivo* Fetal Scans with the Optimized Protocol

Conscientious choices were made throughout the project to ensure that the sequence was safe for scanning the fetus. The 3D radial sequence was developed to deposit low levels of RF energy by choosing the smallest possible flip angle for good contrast. Other precautions included setting the RF pulse type to “low SAR” and the Gradient mode to “whisper” in the scan protocol. These settings elongate the length of time over which the RF pulses and gradients are applied, which translates to a shallower gradient slope and minimises the risk of peripheral nerve stimulation in the patient. A shallower gradient also means that significantly less noise is generated during the scan. These choices were effective since during pregnant scans, the SAR value measured in Normal Mode over the torso was well under the machine-regulated SAR limit.

In the early stages of protocol development, it was noted that fetal scans conducted at the Ernst angle of 4^{o} did not provide good contrast for observing the fetal brain (Fig. 4.38). Therefore, a more suitable protocol was developed, which included a higher flip angle of 7^{o}, through a series of normal abdominal scans. Scanning with this protocol still produced images with very low signal and little contrast between the fetal brain and surrounding amniotic fluid, even though the flip angle was chosen to

optimize this contrast. It should be noted that we did not expect to see a contrast between the grey and white matter within the fetal brain since the T1 value used was an average of the grey and white matter combined and an estimate from preliminary research [67].

The outline of the fetal skull can be identified within sub-spiral images consisting of *N*=1024 spokes (Fig. 4.39) and a smoother image is produced when all sub-spirals are combined in k-space and then reconstructed into a single volume (Fig. 4.40). Although the contrast obviously needs to be improved, we were content with the lack of streaking artifacts within reconstructed sub-spiral images and the minimal artifacts in the combined volume since the mother breathed freely throughout the scan and the sub-spirals had not been co-registered to produce this volume.

A slight improvement in SNR is visible in navigator images reconstructed at a reduced base resolution of 64 (Fig. 4.41), but the improvement is not as noticeable compared to the brain navigator images in section 4.4. This is because the acquired fetal navigator images have inherently low signal to begin with and the poor contrast of sub-spiral images is not simply due to under sampling of the k-space periphery. Therefore, reconstructing the central region of k-space does not significantly improve the SNR or contrast. The navigator images were co-registered and a motion plot was produced (Fig. 4.42). Since sub-spiral images were not clear, it was difficult to tell whether the plot correctly reflected the motion performed during the acquisition and since there are many more structures to register than just the fetal brain, it is likely that the plot is not an accurate reflection of the motion of the fetal brain alone. This was supported by the fact that there did not appear to be any improvement in the image clarity once co-registered sub-spiral images were combined into a single volume, when compared to the reconstructed volume from combining motion-affected sub-spirals (Fig. 4.43).

General discussion of the 3D radial FLASH sequence

The 3D radial spoiled GRE (FLASH) sequence has proton-density weighting, some T1 and a little T2* contrast. In the context of fetal brain imaging, since subacute blood shows up bright in PD images, this sequence could provide information on developing brain haemorrhages. However, to achieve a more useful T1-weighting, the low signal and poor tissue contrast produced in the images from fetal scans by this sequence still needs to be improved. Since poor tissue contrast is a characteristic of ultrashort FLASH sequences, an available solution is to apply an appropriate inversion pulse sequence before running the radial FLASH sequence to increase the amount of T1 weighting [14].

For brain and abdomen scans, the 3D radial FLASH sequence was able to provide clear images with good contrast from large sets of data (Fig. 4.14 and 4.15 for *N*=8192 projections). Navigator images produced by this sequence were unfortunately heavily corrupted by artifacts stemming from a number of sources, mostly linked to the reconstruction process. This limited the minimum sub-spiral acquisition time to 2.6s for brain scans (i.e. *N*=512 spokes) and 5.9s (WE selected) for abdominal scans (*N*=1024 spokes). However, it is encouraging to note that by using more accurate (and complex) reconstruction algorithms, the navigator images from this sequence could be reconstructed from fewer spokes, which would make their acquisition faster. At least 4 navigator images can be produced within the “golden rule” limit of 25s for a fetal scan [6], so although the speed of navigator acquisitions may not compete with other navigator sequences, this is a good start towards fetal self-navigation.

In fact, it is very useful that this sequence has been developed with the capacity for self-navigation. This eliminates the necessity for pilot scans to decide where to place the navigator, which often have to be repeated anyway since the baby moves [63], [10]. It also eliminates the need to increase the scan TR since the navigator images themselves contribute towards the signal of the final volume, making this a very efficient method for navigation since no data is “wasted”.

6. Conclusions

In conclusion, a 3D radial sequence was developed that could sample successive subsets of data over the course of an acquisition, demonstrating the possibility of using such an approach for self-navigation. End points of diametric spokes for each sub-spiral are selected in an interleaved fashion from the complete set distributed uniformly on the surface of a sphere. Reconstructing each sub-volume of data produces a series of low resolution navigator images that can be co-registered to provide accurate and regular updates on the motion of a particular region of interest during the acquisition. This has particular relevance to applications in fetal MRI where the fetal brain is likely to move multiple times during an acquisition. Whereas motion would normally result in artifacts in the final images, navigator images with this approach are instead co-registered to correct for motion between successive sub-spirals while corrupted sub-spiral images are discarded. Co-registered navigator images are then combined in image space to produce a final image with improved SNR. The end point trajectory for this radial sequence was designed in such a way that when subsets of data are combined the output volume is uniformly sampled in k-space, thereby minimising the risk of Nyquist streaking artifacts in the final volume due to under-sampling. When compared to an equivalent 3D Cartesian sequence, such as those currently used for fetal MRI, the radial sequence demonstrated improved tolerance to the effects of breathing and rigid body motion. The results presented provide strong evidence of the suitability of radial techniques in applications with strict motion-robustness requirements such as fetal imaging.

One limitation of this project was the few opportunities to perform *in vivo* fetal scans due to the complicated ethics surrounding scanning the fetus for research purposes when the scan was clinically indicated. The objectives of this project were fulfilled to the best of our abilities considering the limitations placed on acquiring fetal scans. Although working protocols could be established for scanning adult brains and abdomens with this sequence, there were insufficient opportunities to optimise the protocol for fetal scanning. The protocol that was used provided low contrast for the fetal brain thus limiting the use of fetal navigator images in the reconstruction/registration section of this work. However, the selected protocols provided good contrast in adult brains and registration with navigator images from these scans was successfully implemented, demonstrating the role of segmented acquisitions when scanning in the presence of motion.

Reconstruction of subsets of k-space data to generate navigator images illustrated some of the challenges associated with radial sampling. In addressing these challenges for the custom sampling scheme used in our sequence, a method was established to reconstruct navigator images at a lower base resolution that reduces the effects of under-sampling at the edges of k-space. This method may be useful in any application where streaking artifacts in images produced with radial sampling need to be reduced. In particular this is very useful when generating rapid low-resolution navigator images. Most registration software perform well even at low spatial resolutions.

An added benefit of reducing the reconstructed base resolution is the resulting increase in signal to noise ratio of navigator images. Since more information was visible in images produced from fewer spokes, the minimum *N* required for sub-spirals when imaging the adult brain could be reduced to 256, which could be acquired in 1.25 seconds.

This result suggests that fewer spokes should be used to produce navigator images during fetal scans, which would decrease the acquisition time of each sub-spiral and therefore improve the temporal accuracy of registration with future applications for fetal navigation. Intra-spiral motion would not only be minimised by the reduction in spiral acquisition time, but its effects are also minimised by the

use of a radial trajectory to acquire each of these sub-spirals which was shown to be more motion-robust that a Cartesian sampling strategy.

In summary, the work presented here provides convincing evidence for the potential role of the 3D radial sequence developed here in fetal MRI and its ability to address many of the problems associated with motion during fetal MRI.

Project Limitations and Future Work

The Gradient Echo setting of the Siemens Cardiovascular (CV) sequence was chosen to develop further due to its unique properties and to explore the applications for T1 weighted images in fetal MRI as an alternative to the numerous existing publications related to sequences that provide T2 weighting. Modifications to the CV sequence included introducing spoiler gradients to eliminate transverse magnetization before the application of each RF pulse, allowing for shorter repetition times between pulse applications and better control of the image contrast produced by the sequence. In hindsight, however, the acquired image signal was very low and an undesirable level of proton-density weighting was produced as opposed to the originally sought T1 weighting. For future works, it may be better to remove the spoiler gradients in to increase the amount of signal generated. An alternative method, as mentioned in the Discussion section, would be to apply an inversion pulse sequence prior to the radial FLASH sequence to increase the amount of T1-weighting.

Another limitation to this work was the lack of opportunities presented for me to scan pregnant patients, which would have enabled more relevant protocol optimization. Access to fetal scans purely for research purposes was limited to my time in Boston, USA, and the few research scans performed during this time were in high demand by more senior researchers who naturally had first priority. Fetal scanning for research is not performed at Groote Schuur Hospital and so access to fetal scans after returning to South Africa was limited to instances where a pregnant mother, referred for clinical reasons, provided their consent for my sequence to be tested at the end of their clinical scan. This occurred on one occasion during this research.

This meant that although protocol parameters were predicted from scanning normal abdomens, the increased presence of fat, amniotic fluid and the fetus changed the imaging environment too substantially to make these predictions relevant. Unfortunately, the T1 value from which the optimum flip angle was calculated was an average for fetal grey and white matter combined and so the calculated flip angle was not expected to produce good contrast inside the fetal brain. In future, separate T1 values for fetal grey and white matter should be acquired to calculate the best flip angle for maximum contrast between these two tissues. It is also suggested to scan multiple pregnant volunteers with varying flip angles to practically determine the optimum flip angle for contrast. Although in this instance there was no choice, it was not ideal for the aims of this project to scan fetuses at a later gestational age since the fetus then has little room to move limiting the potential to assess the efficacy of motion correction strategies.

Since SAR limitations reduced the maximum allowable flip angle to 50 degrees, the achievable image quality was limited. For flip angles below this value the achievable signal and image contrast are very low and a proton density weighted image is produced. In future work it is recommended that the SAR value for the sequence be reduced by elongating the RF pulse application at the expense of a small increase in the TR. This would allow a larger flip angle with higher signal.

Once a working protocol has been established for scanning pregnant patients with this sequence, we recommend that fetal navigator images be acquired with fewer projections than the minimum stated value of N=1024 and reconstructed at a reduced base resolution so that navigator images can be

acquired faster and with fewer spokes. One method to increase the speed of sub-spiral acquisition would be to implement compressed sensing techniques that require even fewer samples in k-space, which would enable the acquisition of navigator images with the same resolution but from fewer spokes. Alternatively, combining this sequence with parallel imaging techniques whereby the local spatial sensitivities of the individual coil elements are used in combination with traditional spatial encoding using the gradients, will speed up the process of image encoding and reduce the duration of the navigator window. This time reduction could be traded off against TR to reduce SAR and increase the possibility for real-time navigation.

The appearance of streaking artifacts from regions of high signal intensity, highlighted the aliasing effects as a result of re-gridding radially acquired data during image reconstruction. To reduce the appearance of artifacts in the reconstructed images, a more accurate method for re-gridding should be implemented than the approach that was used in this work. However, greater computational power will also be needed to deal with the complex algorithms required for more accurate reconstruction and also to speed up the process so that navigator images can eventually provide updates on motion during an acquisition in real-time. Further, the artifacts in the final volume could be reduced by developing a strategy to combine the sub-spirals after registration in k-space rather than in image space. We predict that this would eliminate many of the visible artifacts as gaps in k-space will be filled and the full benefit of acquiring a uniformly sampled final volume will become more apparent.

7. References

[1] American College of Radiology and Society for Pediatric Radiology, "ACR-SPR Practice Guideline for the Safe and Optimal Performance of Fetal Magnetic Resonance Imaging (MRI), Resolution (11)," *American College of Radiology Journal,* 2015.

[2] P. E. Grant, L. Wald and E. Adalsteinsson, "Potential Risks of Fetal Magnetic Resonance Imaging: 3 Tesla Compared to 1.5 Tesla," Fetal-Neonatal Neuroimaging and Developmental Science Center, Boston, 2014.

[3] A. Stecco, A. Saponaro and A. Carriero, "Patient safety issues in magnetic resonance imaging: state of the art," *Radiologica Medica,* vol. 112, pp. 491-508, 2007.

[4] M. Frates, A. Kumar, C. Benson, V. Ward and C. Tempany, "Fetal anomalies: comparison of MR imaging and US for diagnosis.," *Radiology,* vol. 232, pp. 398-404, 2004.

[5] L. J. Erasmus, D. Hurter, M. Naude and H. G. Kritzinger, "A short overview of MRI artefacts," *South African Journal of Radiology,* vol. 26, pp. 13-17, 2004.

[6] A. Gholipour, J. A. Estroff, C. E. Barnewolt, R. L. Robertson, E. Grant, B. Gagoski, S. K. Warfield, O. Afacan, S. A. Connolly, J. J. Niel, A. Wolfberg and R. V. Mulkern, "Fetal MRI: A Technical Update with Educational Aspirations," *Concepts in Magnetic Resonane Part A,* vol. 43 A, no. 6, pp. 237-266, 2015.

[7] C. Limperopoulos and C. Clouchoux, "Advancing Fetal Brain MRI: Targets for the Future," *Seminars in Perinatology,* vol. 33, pp. 289-298, 2009.

[8] H. A. Feldman, J. Brown, G. Chaing and V. Dialani et al., "Brain volumetry in fetuses referred for ventriculomegaly," *AJR Am J Roentgenol,* vol. 189, no. 1, pp. 145-151, 2007.

[9] C. McKenzie et al., "ASSET Enhanced SSFSE Imaging of the fetus," *Proc. Intl. Soc. Mag. Reson. Med.,* vol. 11, p. 60, 2004.

[10] C. Malamateniou, S. Malik and S. Counsell et al., "Motion-compensation techniques in neonatal and fetal MR imaging," *American Journal of Neuroradiology,* vol. 34, pp. 1124-1136, 2013.

[11] K. T. Block, "Advanced Methods for Radial Data Sampling in Magnetic Resonance Imaging," Ph.D. Dissertation, Gottingen University, Gottingen, 2008.

[12] P. Brynolfsson, "Using Radial k-space Sampling and Temporal Filters in MRI to Improve Temporal Resolution," Umea University, Umea, Sweden, 2010.

[13] R. Hashemi, W. Bradley and C. Lisanti, MRI: The Basics, Philadelphia, USA: Lippincott, Williams and Wilkins, 2004.

[14] W. Grodd, U. Klose, D. Peterson and T. Nägele, "Improved contrast and temporal resolution with MR snapshot FLASH imaging of the brain," *Neuroradiology,* vol. 33, pp. 282-285, 1991.

[15] P. Sprawls, “Chapter 9: Spatial Characteristics of the Magnetic Resonance Image,” in *The Physical Principles of Medical Imaging*, Atlanta, Georgia, USA, Meical Physics Pulblishing, 2000.

[16] P. Golland, “Spatial Encoding in MRI and How to Make it Faster,” Massachusetts Institute of Technology, Boston, 2000.

[17] Y. Yamashita, T. Namimoto and Y. Abe et al., “MR Imaging of the Fetus by a HASTE Sequence,” *American Journal of Radiology,* vol. 168, pp. 513-519, 1997.

[18] E. M. Bellon, “MR Artefacts: A Review,” *American Journal of Radiography,* vol. 147, pp. 1271-1280, 1986.

[19] A. Elstar, “mriquestions.com,” 2015. [Online]. Available: http://mriquestions.com/hastess-fse.html. [Accessed 1 May 2016].

[20] M. Patel, R. Klufas and R. Alberico et al., “Half-Fourier Acquisition Single-Shot Turbo Spin-Echo (HASTE) Comparison with Fast Spin-Echo MR in Diseases of the Brain,” *American Society of Neuroradiology,* vol. 18, pp. 1643-1640, 1997.

[21] A. M. Hubbard, M. P. Harty and L. J. States, “A New Tool for Prenatal Diagnosis: Ultrafast Fetal MRI,” *Seminars in Perinatology,* vol. 23, no. 6, pp. 437-447, 1999.

[22] R. V. Mulkern, “Fast Imaging Principles,” in *MR Imaging of the Brain and Spine, 3rd ed*, Philadelphia, Lippincott Williams & Wilkins, pp. 176-178.

[23] R. F. Busse and S. J. Riederer, “Reducing SAR in Real-Time SSFSE Imaging with Variable-Flip Hard Refocusing RF Pulses,” in *International Society for Magnetic Resonance in Medicine*, Glasgow, 2001.

[24] J. Hennig, M. Weigel and K. Scheffler, “Multiecho Sequences With Variable Refocusing Flip Angles: Optimization of Signal Behaviour Using Smooth Transitions Between Pseudo Steady States (TRAPS),” *Magnetic Resonance in Medicine,* vol. 49, pp. 527-535, 2003.

[25] S. Tocchio et al., “MRI Evaluation and Safety in the Developing Brain,” *Seminaars in Perinatology,* vol. 39, no. 2, pp. 73-104, 2015.

[26] R. F. Busse and S. J. Riederer, “Reducing SAR in Real-Time SSFSE Imaging with Variable-Flip Hard Refocusing RF Pulses,” *Proc. Intl. Soc. Mag. Reson. Med,* vol. 9, p. 1790, 2001.

[27] S. N. Saleem, “Fetal MRI: An approach to practice: A review,” *Journal of Advanced Research,* vol. 5, pp. 507-523, 2014.

[28] H. Shinmoto, K. Kashima and Y. Yuasa et al., “MR imaging of non-CNS fetal abnormalities: a pictoral essay,” *Radiographics,* vol. 20, pp. 1227-1243, 2000.

[29] N. Adzick, T. Crombleholme and A. M. Hubbard et al., “Congenital chest lesions: diagnosis and characterization with prenatal MR imaging,” *Journal of Radiology,* vol. 212, pp. 43-48, 1999.

[30] H. Dean, F. Smith and D. J. Lloyd et al., “Fetal fat measurement by magnetic resonance imaging,” *Joural of Radiology,* vol. 62, pp. 603-607, 1989.

[31] Y. Zur, M. Wood and L. Neuringer, “Spoiling of transverse magnetization in steady-state seqeunces,” *Magnetic Resonance in Medicine,* vol. 21, pp. 251-263, 1991.

[32] T. T. Hayat, A. Nihat and M. Martinez-Biarge et al., “Optimization and initial experience of a multisection balanced steady-state free precession cine sequence for the assessment of fetal bahviour in utero,” *American Journal of Neuroradiology,* vol. 32, pp. 331-338, 2011.

[33] S. N. Saleem, M. S. Zaki, N. A. Soliman and M. Momtaz, “Prenatal MRI diagnosis of molar tooth sign at 17-18 weeks of gestation in two fetuses at risk for Joubert Syndrome and related cerebellar disorders,” *Neuropediatrics,* vol. 42, pp. 35-38, 2011.

[34] S. N. Saleem, “Fetal Cardiac Magnetic Resonance (CMR), Echocardiography - New Techniques,” *InTech,* vol. 10, pp. 167-184. Available from: http//www.intechopen.com/articles/show/title/fetal-cardiac-magnetic-resonance-cmr-, 2012.

[35] D. G. Kruger, G. S. Slavin and R. Muthupillai et al., “An orthogonal correlation algorithim for ghost reduction in MRI,” *Magnetic Resonance in Medicine,* vol. 38, pp. 678-686, 1997.

[36] M. M. Chen et al., “Guidelines for Computed Tomography and Magnetic Resonance Imaging Use During Pregnancy and Lactation,” *Obstetrics and Gynecology,* vol. 112, no. 2, pp. 333-339, 2008.

[37] E. S. Gilbert, “Ionizing Radiation and Cancer Risks: What Have We Learned From Epidemiology,” *International Journal of Radiation Biology,* vol. 85, no. 6, pp. 467-482, 2009.

[38] T. Victoria, D. Jaramillo and T. Paul et al., “Fetal magnatic resosnance imaging: jumping from 1.5 to 3 tesla (preliminary experience),” *Journal of Pediatric Radiology,* vol. 44, pp. 376-386, 2014.

[39] H. Clements, K. Duncan and K. Fielding et al., “Infants exposed to MRI in utero have a normal paediatric assessment at 9 months of age,” *Journal of Radioloy,* vol. 73, pp. 190-194, 2000.

[40] R. Kok, M. de Vries and A. Heerschap et al., “Absence of harmful effects of magnetic resonance exposure at 1.5T in utero during the third trimester of pregnancy: a follow-up study,” *Magnetic Resonance Imaging,* vol. 22, pp. 851-854, 2004.

[41] D. J. Panagopoulos, O. Johansson and G. L. Carlo, “Evaluation of Specific Absorption Rate as a Dosimetric Quantity for Electromagnetic Fields Bioeffects,” *PLoS ONE,* vol. 8, no. 6, p. e62663, 2013.

[42] J. Hand et al., “Prediction of specific absorption rate in mother and fetus associated with MRI examinations during pregnancy,” *Magnetic Resonance in Medicine,* vol. 55, no. 4, pp. 883-893, 2006.

[43] J. V. Hajnal, Y. Li and J. Hand et al., “Numerical study of RF exposure an the resulting temperature rise in the fetus during a magnetic resonance procedure,” *Physics in Medicine and Biology,* vol. 55, no. 4, pp. 913-930, 2010.

[44] P. Gowland and J. De Wilde, “Temperature increase in the fetus due to radio frequency exposure during magnetic resonance scanning,” *Physics in Medicine and Biology,* vol. 53, no. 21, pp. L15-8, 2008.

[45] S. Kikuchi et al., “Temperature elevation in the fetus from electromagnetic exposure during magnetic resonance imaging,” *Physics in Medicine and Biology,* vol. 55, no. 8, pp. 2411-2416, 2010.

[46] International Electrotechnical Commission, “Particular requirements for the safety of magnetic resonance equipment for medical diagnosis,” in *Medical electrical equipment*, 2.2 ed., Geneva, IEC, 2008.

[47] F. X. Hebrank and M. Gebhardt, “SAFE-Model- A New Method for Predicting Peripheral Nerve Stimulations in MRI,” in *Proc to 8th Annual ISMRM meeting*, Berlin, 2000.

[48] P. Gover, J. Hykin, P. Gowland, J. Wright, I. Johnson and P. Mansfield, “An assessment of the intrauterine sound intensity level during obstetric echo-planar magnetic resonance imaging,” *Journal of Radiology,* vol. 68, pp. 1090-1094, 1995.

[49] P. Baker, I. Johnson and R. Harvey et al., “A three-year follow-up of children imaged in utero with echo-planar magnetic resonance,” *American Journal of Obstetric Gynecology,* vol. 170, pp. 32-33, 1994.

[50] C. Myers, K. Duncan and P. A. Gowland et al., “Failure to detect intrauterine growth restriction following in uetro exposure to MRI,” *Journal of Radiology,* vol. 71, pp. 549-551, 1998.

[51] M. J. Reeves et al., “Neonatal cochlear function: measurement after exposure to acoustic noise during in utero MR imaging.,” *Journal of Radiology,* vol. 257, no. 3, pp. 802-809, 2010.

[52] American College of Radiology (ACR) and Society for Pediatric Radiology (SPR), “National Guideline Clearinghouse,” 15 September 2011. [Online]. Available: http://www.guideline.gov/content.aspx?id=32509. [Accessed 5 August 2015].

[53] S. T. Wong and M. S. Roos, “A Strategy for Sampling on a Sphere Applied to 3D Selectrive RF Pulse Design,” *Magentic Resonance in Medicine,* vol. 32, pp. 778-784, 1994.

[54] D. C. Peters, M. A. Guttman and A. J. Dick et al., “Undersampled projection reconstruction for active catheter imaging with adaptable temporal resolution and catheter-only views,” *Magnetic Resonance in Medicine,* vol. 49, pp. 216-222, 2003.

[55] G. H. Glover and J. M. Pauly, “Projection reconstruction techniques for reduction of motion effects in MRI,” *Magnetic Resonance in Medicine,* vol. 28, pp. 275-289, 1992.

[56] M. I. Altbach, E. K. Outwater and T. P. Trouard et al., “Radial fast spin-echo method for T2-weighted imaging and T2 mapping of the liver,” *Journal of Magnetic Resonance Imagin,* vol. 16, pp. 179-189, 2002.

[57] T. Shaffter, V. Rasche and I. C. Carlsen, “Motion compensated projection reconstruction,” *Magnetic Resonance in Medicine,* vol. 41, pp. 954-963, 1999.

[58] S. Nielles-Vallespin, “Development and Optimisation of Radial Techniques for Sodium Magnetic Resonance Imaging,” Ph.D. dissertation, Ruperto-Carola University of Heidelberg, Heidelberg, 2004.

[59] F. E. Boada, J. D. Christensen, J. S. Gillen and K. R. Thulborn, “Three-Dimensional Projection Imaging with Half the Number of Projections,” *Magnetic Resonance in Medicine,* vol. 37, pp. 470-477, 1997.

[60] K. Block, M. Uecker and J. Frahm, “Undersampled Radial MRI with Multiple Coils: Iterative Image Reconstruction Using Total Variation Constraint,” *Magnetic Resonance in Medicine,* vol. 57, pp. 1086-1098, 2007.

[61] H. A. Feldman, J. Brown, G. Chaing and V. Dialani et al., “Brain volumetry in fetuses referred for ventriculomegaly,” *AJR Am J Roentgenol,* vol. 189, no. 1, pp. 145-151, 2007.

[62] E. B. Welch, A. Manduca and R. C. e. a. Grimm, “Spherical navigator echoes for full 3D rigid body motion measurement in MRI,” *Magnetic Resonance in Medicine,* vol. 47, pp. 32-41, 2002.

[63] H. Bonel, K. A. Frei and L. Raio et al., “Prospective navigator-echo-based-real-time triggering of fetal head movement for the reduction of artifacts,” *European Radiology,* vol. 18, pp. 822-829, 2008.

[64] J. I. Jackson et. al, “Selection of a Convolution Function for Fourier Inversion Using Gridding,” *IEEE Transactions of Medical Imaging,* vol. 30, no. 3, pp. 473-478, 1991.

[65] O. Bieri, M. Markl and K. Scheffler, “Analysis and Compensation of Eddy Currents in balanced SSFP,” *Magnetic Resonance in Medicine,* vol. 54, pp. 129-137, 2005.

[66] E. B. Saff and A. B. Kuijlaars, “Distributing Many Points on a Sphere,” *The Mathematical Intelligencer,* vol. 19, no. 1, pp. 1-11, 1997.

[67] B. Gagoski, L. Wald and P. E. Grant, “Magnetic resonance fingerprinting for fetal imaging at 3T - initial results,” Harvard-MIT Health Sciences and Technology, Massachusetts Institute of Technology and the Fetal-Neonatal Neuroimaging & Developmental Science Center, Boston Children's Hospital, Boston, MA, United States, 2014.

[68] C. Chlor, E. Han and J. Stainsby et al., “Quantitative Measurements of T1 and T2 for the Abdomen in a 3 Tesla Whole-Body Imager,” *Proc. Intl. Soc. Mag. Reson. Med,* vol. 11, p. 1327, 2003.

[69] M. Jenkinson, P. Bannister, J. Brady and S. Smith, “Improved optimisation for the robust and accurate linear registration and motion correction of brain images,” *NeuroImage,* vol. 17, no. 2, pp. 825-841, 2002.

[70] A. J. W. van der Kouwe and H. Bhat, “Motion Correction for 3D Radial Encoded Spoiled Gradient Echo Imaging of the Head,” *Proc. International Society for Magnetic Resonance in Medicine,* vol. 20, p. 3413, 2012.

[71] C. Beckmann, M. Jenkinson, T. Behrens, M. Woolrich and S. Smith, “FSL,” *NeuroImage,* vol. 62, pp. 782-790, 2012.

[72] H. Bhat, Interviewee, *Applications for the Siemens Cardiovascular Sequence.* [Interview]. A.A. Martinos Center for Biomedical Imaging, Charelston Navy Yard, Boston., 20 February 2015.

[73] S. K. Patch, "k-Space Data Preprocessing for Artifact Reduction in MR Imaging," *Multidimensional Image Processing, Analysis, and Display: RSNA Categorical Course in Diagnostic Radiology Pysics,* pp. 73-87, 2005.

[74] V. Rasche, R. Sinkus and R. Proska, "Resampling of data between arbitrary grids using convolution interpolation," *IEEE Transactions on Medical Imaging,* vol. 18, no. 5, pp. 385-392, 1999.

[75] O. A. Glenn and A. J. Barkovich, "Magnetic Resonance Imaging of the Fetal Brain and Spine: An Increasingly Important Tool in Prenatal Diagnosis," *Americal Journal of Neuroradiology,* vol. 27, pp. 1604-1611, 2006.

[76] P. C. Brugger, F. Stuhr, C. Lindner and D. Prayer, "Methods of fetal MR: beyond T2-weighted imaging," *European Journal of Radiology,* vol. 57, pp. 172-181, 2006.

[77] C. Malamateniou, A. K. McGuinness and J. M. Allsop et al., "Snapshot inversion recovery: an optimized single-shot T1-weighted inversion-recovery seqeunce for improved fetal brain anatomic delineation," *Radiology,* vol. 258, pp. 229-235, 2011.